ISSN: 2708-7956

الأكاديمية
للهندسة والعلوم

Academic
For Engineering and Science

مجلة علمية محكمة فصلية
تصدر عن نقابة الأكاديميين العراقيين
المجلد (4) العدد (4)
كانون الاول - السنة 2022

رقم الإيداع في الدار الوطنية
2422 لسنة 2020

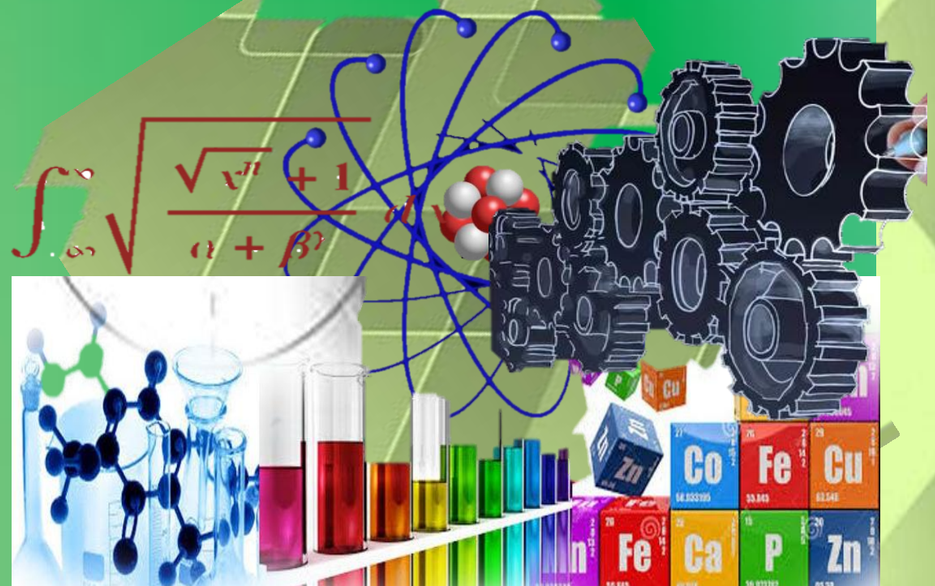

الأكاديمية للهندسة والعلوم
http://aphjournal.iraqiacademic.com
ISSN: 2708-7956 DOI prefix: 10.47719

الأكاديمية

للهندسة والعلوم

Academic

For Engineering and Science

مجلة علمية محكمة فصلية

تصدر عن نقابة الأكاديميين العراقيين

المجلد (4) العدد (4)

2022 /12/ 15

كـــلمة العدد (4) لسنة (2022)

يسعدنا ان نقدم لكم **العدد الرابع/ السنة 2022** لمجلة **الأكـاديمـية للهندسة والعلوم**. أود أن اسجل شكري الجزيل للجهود الكبيرة لكل من ساهم في إظهار هذا العدد. كما أتقدم بالشكر لجميع الباحثين الذين دعموا المجلة من خلال نشر أبحاثهم فيها، خاصاً بعد حصول المجلة على الرقم المعّرف **DOI** في عام 2020.

ضم هذا العدد، بحوث في مختلف المجالات العلمية، هي: الهندسة، والفيزياء، والاستشعار عن بعد، التحليل الإحصائي والرياضيات.

نأمل أن تحقق مجلة الأكاديمية للهندسة والعلوم، من خلال هذه الطبعة، تطلعات الباحثين والمهتمين، وأن نسعى، بعون الله تعالى، إلى تطوير مجلتنا نحو الأفضل، وأن يكون لها حضورا علميا متميزا إقليمياً وعالمياً، ونتطلع ان تكون المجلة في التصنيفات العلمية الدولية.

مع خالص التقدير

أ. د. أحمد كمال أحمد
رئيس هيئة التحرير
كانون الأول - 2022

نبـــــذة عن
نقابة الاكاديميين العراقيين

أسست نقابة الأكاديميين العراقيين بموجب القانون رقم (61) لسنة (2017)، بغية الاهتمام بالملاك التدريسي والأكاديمي (الأكاديمي: التدريسي الحاصل على شهادة الماجستير أو الدكتوراه ويمارس مهنة التدريس أو يعمل بمراكز البحث العلمي في الجامعات).

والارتقاء بمستوى العاملين في هذا القطاع الحيوي وإعداد الخطط والسياسات التي ترتقي بالعملية التدريسية ومن أجل إنشاء مجالس ونقابات تهتم بشؤون الأكاديميين والدفاع عنهم وحفظ كرامتهم وضمان حرياتهم الأكاديمية، ومن أجل رفع سمعة الجامعات والمعاهد العراقية ومساواتها مع مثيلاتها في الدول المتحضرة. ووفقاً للمادة –2– من البند الثاني من قانونها فأنها:

أولاً: تتمتع نقابة الأكاديميين العراقيين بالشخصية المعنوية والاستقلال المالي والإداري يمثلها (نقيب الأكاديميين العراقيين) أو من يخوله.

ثانياً: يكون مركز النقابة في بغداد ولها فتح فروع في المحافظات وحيثما تقتضي مصلحة النقابة إيجاد تمثيل.

ثالثاً: لأعضاء الهيئات التدريسية في الجامعات والمعاهد العراقية المعترف بها من وزارة التعليم العالي والبحث العلمي الانتماء إلى النقابة.

ووفقاً للمادة –3– فأن أهداف تأسيس النقابة هي:

أولاً: الارتقاء بمهنة التعليم العالي والبحث العلمي لتحقيق رسالتها في خدمة الوطن وأجيال الأمة.

ثانياً: التنسيق والتعاون مع وزارة التعليم العالي والبحث العلمي والجهات ذات الصلة بما يحقق مهام النقابة.

ثالثاً: تعزيز أخلاقيات مهنة التعليم العالي والمحافظة على آداب وتقاليد وشرف المهنة.

رابعاً: تشجيع الدراسات والبحوث والنشاطات والمؤتمرات التعليمية وعقد الدورات والندوات لرفع المستوى العلمي والمهني لتدريسي الجامعات والمعاهد العراقية.

خامساً: تعزيز مكانة الأكاديميين في المجتمع والدفاع عن حقوقهم ومصالحهم وكرامتهم.

سادساً: النهوض والارتقاء بالأعضاء مهنياً واقتصاديا وثقافياً واجتماعياً.

سابعاً: تأسيس صندوق للتكافل الاجتماعي لمساعدة أعضاء النقابة، يؤمن لهم ولأسرهم العيش الكريم في حالات العجز الكامل أو الوفاة وتوفير الرعاية الصحية للأعضاء وأسرهم.

ثامناً: التعاون وتوطيد العلاقات مع الاتحادات العربية والدولية المماثلة.

أ. م. د. مهـند الهـلال
نقيب الاكاديميين العراقيين

المحتوى (العدد 4 لسنة 2022)

أهداف ورؤية المجلة Aims and Scope

- تنشر المجلة الدراسات العلمية ذات الأفكار الأصيلة والحديثة والمتجددة، ويحوت الرسائل والأطروحات، التي لم يسبق نشرها أو المساهمة بها في أحد الملتقيات العلمية، وان تكون هذه البحوث مندرجة ضمن أحد المحاور تخصصات الهندسية والعلوم الصرفة.
- كما تنشر المجلة الكتب المؤلفة والمترجمة ضمن التخصصات أعلاه.

الوصول المفتوح للبحوث Open Access Policy

مجلة **الأكاديمية للهندسة والعلوم** هي مجلة مفتوحة الوصول، بالتالي لا توجد رسوم مطلوبة لتنزيل أي منشور من موقع المجلة من قبل المؤلفين والقراء والمؤسسات، وعلى الموقع:
http://aphjournal.iraqiacademic.com/Journal/GetAllVersions

قواعد النشر:

- البحوث المرسلة إلى المجلة يجب أن تكون سليمة من الأخطاء اللغوية والمنهجية والمعرفية، وملتزمة بالأعراف العلمية المتبعة، ولم يسبق نشرها.
- لا ينبغي أن يتحاوز عدد صفحات البحث عن خمسة عشر ورقة من حجم B5.
- في حالة وجود هوامش في اسفل الصفحة ينبغي اعتماد ترقيم آلي يتجدد في كل صفحة.
- يتضمن البحث ملخصين: الأول بلغة البحث، والثاني باللغة العربية أو الإنجليزية.
- تخضع جميع البحوث للتحكيم العلمي على نحو سري، ويخبر الباحث إما بقبول بحثه، أو بالقبول المشروط ببعض التعديلات التي يبلغ بها، أو بالرفض. وفي هذه الحالة الأخيرة؛ فإن المجلة ليست ملزمة ببيان الأسباب.

توصيات تقنية في كتابة البحوث:

- مقاس الورقة والهوامش: الورقة حجم B5، ويترك هامش بمسافة 2 سم من حواشي الورقة. مع مسافة 1 سم بين الأسطر في المتن والهوامش.
- يُعتمد الخط **Simplified Arabic** (البحوث باللغة العربية)/ و**Times New Roman** (البحوث باللغة الإنكليزية)، مقاس 16 غامق عنوان البحث، مقاس 14 غامق العناوين الأساسية، مقاس 12 غامق العناوين الفرعية، وبمقاس 12 في المتن، مقاس 11 غامق لعناوين الأشكال والجداول، 10 في الحواشي.

معلومات الاتصال:

- **موقع المجلة:** http://aphjournal.iraqiacademic.com/

ISSN: 2708-7956, DOI prefix: 10.47719

- **البريد الإلكتروني للمجلة:** info@iraqiacademics.iq
dr.ziadmabood@gmail.com

- **أرقام الهواتف: 9647709298631 -9647902746409**

- **رقم الإيداع في الدار الوطنية 2422 لسنة 2020**

Contra - $(1\ 2)^*$ - (πgb, c) - Open Functions Kinds

Dunya Mohamed Hameed
Mustansiriyah University - College of Education - Department of Mathematics
dunya_mahamed@uomustansiriyah.edu.iq

Abstract:

Labor purpose is to present new kinds of contra–(1,2)*–open functions which is contra–(1,2)*–(πgb,c)–open, and study some of it is characteristics. Other contra–(1,2)*–(πgb,c)–open types are also introduce namely [contra–(1,2)*–(πgb, bc)–open and contra –(1,2)*– (b πgbc)–open] functions, As well, will also debate the connection among these types of functions by presenting some propositions and examples that explain and investigate the connection between these kinds. In addition, we will present the necessary stipulations that make the reverse relation between those contra -$(1, 2)^*$-(πgb, c)-open functions kinds come true.

Keywords: (1, 2) *– πgb–open functions, M– (1,2) * –πgb–open function, Contra–(1 2) *–open function and Contra–(1,2) * (πgb c) –open.

المفتوحة -*(1 2)-(πgb,c) أنواع الدوال الضد -

م. دنيا محمد حميد
الجامعة المستنصرية - كلية التربية - قسم الرياضيات

الخلاصة:

الغرض من هذا البحث هو دراسة أنواع أخرى من الدوال الضد المفتوحة من النمط –(πgb,c)–(1,2)* ودراسة بعض من خصائصها. وأنواع أخرى من الدوال الضد المفتوحة من النمط –(πgb,c)–(1,2)* أيضا سوف تقدم تدعى (الدوال الضد المفتوحة من النمط –(πgb, bc)–(1,2)* والدوال الضد المفتوحة من النمط –(b, πgbc)–(1,2)*). كذلك, سوف نناقش أيضا العلاقة بين هذه الأنواع من خلال تقديم بعض الخصائص والامثلة التي تشرح وتحقق العلاقة بين تلك الأنواع. فضلا عن ذلك، سنقدم الشروط الضرورية التي تجعل العلاقة العكسية بين أنواع الدوال الضد المفتوحة من النمط –(πgb,c)–(1,2)* صحيحة.

الكلمات المفتاحية: الدوال المفتوحة من النمط πgb –(1,2)*، الدوال المفتوحة من النمط πgb –(1,2)* – M، الدوال ضد المفتوحة –(1,2)* والدوال ضد المفتوحة –(πgb,c)–(1,2)*

Introduction:

In 1963. Kelly J [3] was the first researcher who submit and studied the idea of the topic of bitopological spaces, defining them as a triple arrangement $(X, \tau_1\ \tau_2)$ which contains X, set is not empty and τ_1 τ_2 are two arbitrary topologies define on X. Ravi. O and Lellis Thivagar. M [5] they have proffered the conception of (1,2) *– (regular open (closed) sets. Sreeja. D and Janaki. C [6,7] They defined and proffered the notion of [(1,2)*–b–closed, (1,2)*–b–open (1,2)*–πgb –closed, (1,2)*– πgb –open] sets and they also introduced the (1,2)*– πgb –closed (open) functions , while the notion of contra– open(closed) functions in bitopological spaces, presented and debated by (Noiri. T and Popa. V, 2006 [4]) in 2021, Dunya. M. H. Sanna. H. J and Intidhar. Z. M [2] they submitted and debated a new several types of contras– (1,2) *– (open functions). The goal of this study is to submit a novel kind of contra– open functions. As well, we will involve the presentation of different definitions and outcomes in order to treatise the connection between these sorts of functions.

2-preliminaries:

This section proffers some definitions and outcomes that necessity in this research.

Definition (2،1), [3]: Let $Q \subseteq (\mathcal{M}\ \Im_1\ \Im_2)$, then

1- if $Q = P \cup K$ Where $P \in \Im_1$ and $K \in \Im_2$ is said $\Im_{1,2}$–open or [(1 2) *–open], and $(\Im_{1,2}$–open$)^c$ namely $\Im_{1,2}$–closed or [(1 2) *–closed].

2- $\cup\{Z: Z \subseteq Q$ and Z is $\Im_{1,2}$–open$\}$is called $\Im_{1,2}$–Interior of Q and symbolized by $\Im_{1,2}$–Int(Q).

3- $\cap$ $\{W: Q \subseteq W: W$ is $\Im_{1,2}$ – closed $\}$ namely $\Im_{1,2}$–closure of Q. and symbolized by $\Im_{1,2}$–Cl(Q).

Definition (2،2): If $Q \subseteq (\mathcal{M}\ ,\ \Im_1\ ,\ \Im_2)$, then Q namely

1- (1,2) *-regular open [5] , if $Q = \Im_{1,2}$– Int $(\Im_{1,2}$–Cl$(Q))$.

2- (1,2) * –b – open [6] if $Q \subset \Im_{1,2}$– Cl $((\Im_{1,2}$– Int $(Q)) \cup \Im_{1,2}$– Int $(\Im_{1,2}$ – C$(Q))$.

Remark (2،3) , [3] , [6]:

1. $\Im_{1\ 2}$– open set of $(\mathcal{M}\ \Im_1\ \Im_2)$, it is not indispensable to be topology.

2. If $Q \subseteq (\mathcal{M}\ \Im_1\ \Im_2)$, then $\cap\{W: Q \subseteq W: \forall W$ is $(1,2)^*$–b–closed of $\mathcal{M}\}$ namely $(1,2)^*$ – b–closure of Q. and symbolized by (1,2) * – bcl(Q).

Definition (2،4) [6]: If $Q \subseteq (\mathcal{M}, \Im_1, \Im_2)$, hence a set Q namely (1,2) *– πgb–closed if $\Im_{1,2}$ – bcl$(Q) \subseteq E$ such that $Q \subseteq E$ and E is (1,2) *–π–open , where $((1,2)^*$–πgb–closed$)^c$ is said $(1,2)^*$- πgb – open.

Remark (2،5), [6]: In $(\mathcal{M}, \Im_1, \Im_2)$,hence $\forall$

(i) $\Im_{1\ 2}$–closed$\langle\Im_{1,2}$ closed $\rangle$set is $\Im_{1,2}$– πgb – closed in $\mathcal{M}$.

(ii)$\Im_{1,2}$–open $(\Im_{1,2}$ –b– open$)$ set in $\mathcal{M}$ is $\Im_{1,2}$– πgb – open.

Definition (2، 6): A function $f: (\mathcal{M}, \Im_1, \Im_2) \rightarrow (T, \varepsilon_1, \varepsilon_2)$ namely:

1- Contra – (1 2)* – open (resp. contra – (1 2)*– closed), [4] if $\forall\ \partial_{1,2}$ – open $\langle$ resp, $\Im_{1,2}$ – closed $\rangle$ set E in $\mathcal{M}$, $f(E)$ is $\varepsilon_{1,2}$ –closed $[\![$resp. $\varepsilon_{1,2}$ –open $]\!]$ set in T.

2- (1 2)*– πgb – open $\langle$ (1,2)*–πgb –closed$\rangle$, [7] if $\forall\ \Im_{1,2}$– open $\langle\Im_{1\ 2}$ – closed$\rangle$ set E in $\mathcal{M}$ $f(E)$ is $\varepsilon_{1,2}$ – πgb–open $[\![\varepsilon_{1,2}$ – πgb–closed $]\!]$ in T.

3-M – (1,2)* –πgb–closed $\langle$ resp , M – (1 2)*–πgb–open $\rangle$, [7] if $\forall\ \Im_{1\ 2}$ —πgb–closed $\langle\forall\ \Im_{1,2}$ —πgb–open$\rangle$ E in $\mathcal{M}$, $f(E)$ is $\varepsilon_{1,2}$ –πgb–closed $[\![\ \varepsilon_{1,2}$ –πgb–open $]\!]$in T.

4- (1,2) * –M*–πgb–closed [1] if $\forall\ \Im_{1\ 2}$ –πgb–closed E in $\mathcal{M}$ $f(E)$ is $\varepsilon_{1,2}$ –closed in T.

Definition (2،7),[7]: $(\mathcal{M}, \Im_1, \Im_2)$ is known as (1 2)* – πgb–space if each $\Im_{1,2}$ – πgb –closed $(\Im_{1,2}$ πgb–open$)$ set is $\Im_{1,2}$_closed $(\Im_{1,2}$–open$)$in $\mathcal{M}$.

Contra- (1,2) *- (πgb c) - Open Functions Kinds:

Following, we will begin define contra-$(1,2)^*$-(πgb, c)- open.

Definition (3،1): A function $f: (X, \tau_1, \tau_2) \rightarrow (\Upsilon, \Omega_1, \Omega_2)$ namely contra -$(1,2)^*$-(πgb, c)-

open if $f(Q)$ is $\Omega_{1,2}$-closed in $(\Upsilon, \Omega_1, \Omega_2)$, for $\forall$ (1,2) *- πgb – open set Q in X.

Example (3،2): Assume X=Υ={$\mathcal{J}$ σ ℓ}, with τ_1 = {X,ϕ,{$\mathcal{J}$}}, τ_2 ={X, ϕ,{σ}}, Ω_1 = {Υ,{$\mathcal{J}$},{$\mathcal{J}$,ℓ},{$\mathcal{J}$, σ}, ϕ} and Ω_2={Υ, {σ}, {ℓ},{σ ℓ}, ϕ}. πGBO(X)={X,{$\mathcal{J}$},{ℓ},{σ},{$\mathcal{J}$, ℓ },{σ ℓ},{$\mathcal{J}$ σ}, ϕ}. Suppose $f: (X, \tau_1, \tau_2) \rightarrow (\Upsilon, \Omega_1, \Omega_2)$ s.t $f(\mathcal{J}) = \mathcal{J}$, $f(\sigma) = \ell$ and $f(\ell) = \sigma$, it is elucidative that f is contra -(1 2)*- (πgb, c)-open.

Proposition (3،3): If $f: (X, \tau_1, \tau_2) \rightarrow (\Upsilon, \Omega_1, \Omega_2)$ is contra -(1 2)*-(πgb, c)- function, then f is contra -(1 2)*-open.

Proof: Postulate a set Q is $\tau_{1,2}$ -open in X. implies that Q is $(1\ 2)^*$-πgb-open in X (by Remark (2.5)-point (i)), and hence $f(Q)$ is $\Omega_{1,2}$ -closed set Y, so we conclude f is contra -$(1\ 2)^*$-open.

Below example explain it the opposite (3.3) is incorrect in general:

Example (3.4): Let $X=Y=\{\mathcal{J}, \sigma\ \ell, \mathcal{b}\}$, with $\tau_1 = \{X, \phi, \{\mathcal{J}\}, \{\mathcal{b}\}, \{\mathcal{J}, \mathcal{b}\}\}$, $\tau_2 =\{X, \phi, \{\ell, \mathcal{b}\}, \{\mathcal{J}\}, \{\mathcal{J}, \ell, \mathcal{b}\}\}$, $\Omega_1 =\{Y, \{\mathcal{J}\}, \{\sigma\}, \{\mathcal{J}, \sigma\}, \phi\}$ and $\Omega_2=\{Y, \{\sigma\}, \{\mathcal{J}, \sigma\}, \{\sigma, \ell\}, \{\mathcal{J}, \sigma, \ell\}, \{\mathcal{J}, \sigma, \mathcal{b}\}, \phi\}$. Suppose $f: (X, \tau_1, \tau_2) \to (Y, \Omega_1, \Omega_2)$ such that $f(\mathcal{J})=\ell$, $f(\sigma)= \sigma$ $f(\ell) = \mathcal{J}$ and $f(\mathcal{b}) = \mathcal{b}$. Manifestly that f is contra -$(1\ 2)^*$-open, but is not contra -$(1\ 2)^*$-$(\pi gb, c)$-open. Since $\exists$ $(1\ 2)^*$-πgb-open Q $=\{\sigma\}$in X, such that $f(Q)= f(\{\sigma\})=\{\sigma\}$ is not closed in (Y, Ω_1, Ω_2).

Next. the stipulation which make (3.3) correct:

Proposition (3.5): If $f: (X, \tau_1, \tau_2) \dashrightarrow (Y, \Omega_1, \Omega_2)$ is contra$-(1\ 2)^* -$ open hence f is contra $-(1,2)^* - (\pi gb, c) -$ open, if X is $(1,2)^*$-πgb-space.

Proof:- If presume Q is $(1,2)^*$-πgb- open in X, from the postulate X is $(1,2)^*$-πgb- space, this implies Q is $\tau_{1,2}$ -open in X. Thus, $f(Q)$ is $\Omega_{1,2}$ - closed in Y and hence f is contra -$(1,2)^*$-$(\pi gb, c)$- open.

Several outcomes concerning the composition of contra -$(1, 2)^*$-$(\pi gb, c)$- open will be given in the next propositions.

Proposition (3.6): If $f: (X, \tau_1, \tau_2) \dashrightarrow (Y, \Omega_1, \Omega_2)$ is contra-$(\pi gb, c)$-open and $\ell: (Y, \Omega_1, \Omega_2) \dashrightarrow (H, e_1\ \ e_2)$ is any function. then $\ell \circ f: (X, \tau_1, \tau_2) \dashrightarrow (H, e_1\ \ e_2)$ is contra-$(\pi gb, c)$-open. If

(a) ℓ is $(1, 2)^*$- closed

(b) ℓ is $(1, 2)^*$-M*-πgb-closed

Proof(a):- Assume a set Q be $(1, 2)^*$-πgb-open in X, f is contra -$(1,2)^*$- $(\pi gb, c)$-open, this lead $f(Q)$ is $\Omega_{1,2}$ closed in Y. As well ℓ is $(1, 2)^*$-closed, this implies $\ell(f(Q))$ is $e_{1,2}$ -closed in H But, $\ell(f(Q)) = \ell \circ f(Q)$. Therefore, $\ell \circ f: (X, \tau_1, \tau_2) \dashrightarrow (H, e_1\ \ e_2)$ is contra-$(\pi gb, c)$-open.

Likewise, point (b) proves.

Proposition (3.7): If $f: (X, \tau_1, \tau_2) \dashrightarrow (Y, \Omega_1, \Omega_2)$ is contra-$(1, 2)^*$-open $\ell: (Y, \Omega_1, \Omega_2) \dashrightarrow (H, e_1\ \ e_2)$ be any function and H is (1,2) *-πgb-space. Hence $\ell \circ f: (X, \tau_1, \tau_2) \dashrightarrow (H, e_1\ \ e_2)$ is contra -$(1, 2)^*$- $(\pi gb, c)$-open if ℓ is

(a) $(1\ 2)^*$-πgb-closed

(b) M $(1, 2)^*$ πgb–closed

Proof(a): Suppose Q be $(1, 2)^*$-πgb-open in X, as per the assumption f is contra -$(1, 2)^*$-$(\pi gb, c)$-open we conclude $f(Q)$ is $\Omega_{1,2}$-closed in Y, this implies $\ell(f(Q)) = \ell \circ f(Q)$ is $(1, 2)^*$-πgb -closed in H, but H is $(1, 2)^*$-πgb-space this lead $\ell(f(Q))=\ell \circ f(Q)$ is $e_{1,2}$-closed in H. Hence, $\ell \circ f$ is contra -$(1, 2)^*$- $(\pi gb, c)$-open. By the same ditto, point (b) proves.

Other forms of contra -$(1, 2)^*$-$(\pi gb, c)$- open functions, we will give in the next definitions.

Definition (3.8): A function $f: (X, \tau_1, \tau_2) \dashrightarrow (Y, \Omega_1, \Omega_2)$ namely contra-$(1, 2)^*$-$(\pi gb, bc)$-open if $f(Q)$ is $\Omega_{1,2}$ -b-closed in (Y, Ω_1, Ω_2), $\forall Q$ is$(1, 2)^*$-πgb-open set in X.

Example(3.9): Let $X=\{\mathcal{J}\ \sigma\ \ell\ \mathcal{b}\}$, with $\tau_1=\{X,\phi\ \{\mathcal{J}\ \sigma\}\}$, $\tau_2=\{X,\phi,\{\ell\ \mathcal{b}\}\}$, hence $\tau_{1,2}=\{X,\phi\ \{\ell\ \mathcal{b}\},\{\mathcal{J}\ \sigma\}\}$. Assume $f:(X,\tau_1,\tau_2)\to(X,\tau_1\ \tau_2)$ s.t $f(\mathcal{J})=\mathcal{J}$, $f(\sigma)=\sigma$ $f(\ell)=\ell$ and $f(\mathcal{b})=\mathcal{b}$. It is intelligibly that f is contra-$(1,2)^*$-$(\pi gb,bc)$-open.

Proposition (3.10): Each contra-$(1,2)^*$-$(\pi gb,c)$- function is contra-$(1,2)^*$-$(\pi gb,bc)$ -open.

Proof: If presume $f:(X,\tau_1,\tau_2)\to(Y,\Omega_1,\Omega_2)$ is contra-$(1,2)^*$-$(\pi gb,c)$-function, and Q be $(1,2)^*$ - πgb - open in X. Thus, $f(Q)$ is $\Omega_{1,2}$-closed in Y, since $\forall$ $\Omega_{1,2}$-closed is $(1,2)^*$-b-closed. This implicate $f(Q)$ is$(1\ 2)^*$- b-closed in Y and hence f contra - $(1,2)^*$-$(\pi gb,bc)$ - open.

In general, the opposite of the prior proposition is incorrect. Example (3.11) elucidates it

Example (3.11): Let $X=\{\mathcal{J},\sigma,\ell,\mathcal{b}\}$, with $\tau_1=\{X,\phi,\{\sigma\},\{\mathcal{J}\},\{\mathcal{J},\sigma,\mathcal{b}\},\{\mathcal{J},\sigma\}\}$, $\tau_2=\{X,\ \{\mathcal{J},\sigma,\ \ell\},\{\mathcal{J},\sigma\},\phi,\{\mathcal{J},\sigma,\mathcal{b}\}\}$, $\Omega_1=\{Y,\{\mathcal{J},\sigma\}\ \phi\}$and $\Omega_2=\{Y,\{\sigma,\ell\},\phi\}$ Suppose $f:(X,\tau_1\ \tau_2)\to(Y,\Omega_1,\Omega_2)$ s.t $f(\mathcal{J})=\mathcal{J}$, $f(\sigma)=\ell$ $f(\ell)=\mathcal{b}$ and $f(\mathcal{b})=\sigma$,it is conspicuous that f is contra - $(1,2)^*$- $(\pi gb,bc)$-open, but not contra-$(1,2)^*$- $(\pi gb,c)$-open because $\exists$ $(1,2)^*$- πgb -open $Q=\{\ell\}$ in X,s.t $f(Q)=f(\{\ell\}=\{\mathcal{b}\}$ is not $\Omega_{1,2}$ _ closed in Y.

Proposition (3.12) offered the stipulation that make (3.11) correct

Proposition (3.12): $f:(X,\tau_1,\tau_2)\to(Y,\Omega_1,\Omega_2)$ is contra-$(1,2)^*$- $(\pi gb,c)$- open, if f is contra $(1,2)^*$- $(\pi gb,bc)$-open and Y is $(1,2)^*$- πgb-space.

Proof: - Assume Q be $(1,2)^*$- πgb-open in X, this lead $f(Q)$ is $(1,2)^*$- b-closed in Y by (2-5)-i- we conclude $f(Q)$ is $(1\ 2)^*$- πgb closed in Y. From the presumption Y is $(1,2)^*$- πgb-space. So, we conclude $f(Q)$ is $\Omega_{1,2}$- closed in Y subsequently f is contra -$(1\ 2)^*$- $(\pi gb,c)$-open.

Remark (3.13): ((Contra $(1,2)^*$ $(\pi gb,bc)$-open and contra$-(1,2)^*$ open)) functions notions are independents. Next examples demonstrate this.

Example (3.14): Let $X=\{\mathcal{J}\ \sigma\ \ell\}$ $\tau_1=\{X,\phi\}$, $\tau_2=\{X,\{\mathcal{J}\ \sigma\},\phi\}$, $\Omega_1=\{Y,\{\mathcal{J}\},\phi\}$and $\Omega_2=\{Y,\{\sigma\},\phi\}$, Define $f:(X,\tau_1,\tau_2)\to(Y,\Omega_1,\Omega_2)$ s.t $f(\mathcal{J})=\mathcal{J}$, $f(\sigma)=\ell$, $f(\ell)=\sigma$. it is conspicuous f is contra $(1\ 2)^*$ open. But f is not contra $-(1\ 2)^*$ $(\pi gb,bc)$-open. because $\exists$ $(1,2)^*$- πgb -open $Q=\{\mathcal{J},\ell\}$ in X, $f(Q)=f(\{\mathcal{J}\ \ell\}=\{\mathcal{J}\ \sigma\}$ in Y is not $\Omega_{1,2}$ b $-$ closed.

Example(3.15): Let $X=\{\mathcal{J},\sigma,\ell,\mathcal{b}\}$with $\tau_1=\{X,\{\mathcal{J},\sigma,\ell\},\phi\}$ $\tau_2=\{X,\phi\ \{\mathcal{J}\}\}$, $\Omega_1=\{Y,\{\mathcal{J},\ell\},\phi\}$ and $\Omega_2=\{Y,\{\ell,\mathcal{b}\},\phi\}$, let $f:(X,\tau_1,\tau_2)\to(Y,\Omega_1,\Omega_2)$ s.t $f(\mathcal{J})=\sigma$, $f(\sigma)=\ell$ $f(\ell)=\mathcal{J}$ and $f(\mathcal{b})=\mathcal{b}$. it is intelligibly that f is contra-$(1,2)^*$- $\pi gb,bc)$-open., but not contra -$(1,2)^*$- open, because $\exists$ $\tau_{1,2}$–open $Q=\{\mathcal{J}\}$ in X, $f(Q)=f(\{\mathcal{J}\}=\{\sigma\}$ in Y is not $\Omega_{1,2}$-closed.

Proposition(3.16) submit the stipulation which makes the Remark(3.13) correct:

Proposition (3.16): Assume $f:(X,\tau_1,\tau_2)\to(Y,\Omega_1,\Omega_2)$ be any function, hence f is

(i) contra- $(1\ 2)^*$ $(\pi gb,bc)$-open, if f is contra $-(1,2)^*$ open and X is $(1\ 2)^*$ πgb-space.

(ii) contra $(1,2)^*$ open if is contra-$(1\ \ 2)^*(\pi gb\ bc)$- open ,and Y is $(1,2)^*$- πgb space.

Proof:-

(i) Postulate that Q is $(1\ 2)^*\pi gb$-open in X, thus Q is $\tau_{1,2}$-open in X, (because X is $\tau_{1\,2}-\pi gb$-space) this lead $f(Q)$ is $\Omega_{1,2}$- closed in Y. Since ($\forall\Omega_{1,2}$-closed set is $(1,2)^*$- b-closed), this implies $f(Q)$ is $b-$closed in Y, hence f is contra$-(1\ 2)^*-(\pi gb,bc)-$ open. Likewise, we prove point -ii-.

Proposition (3.17): If $f:(X,\tau_1,\tau_2)\to(Y,\Omega_1,\Omega_2)$ is contra-$(1\ 2)^*$-$(\pi gb,bc)-$open and $\ell:(Y,\Omega_1,\Omega_2)\to(H,e_1\ \ e_2)$ is $(1,2)^*$- M^*- πgb-closed function, hence $\ell\circ f:(X,\tau_1\ \tau_2)\to(H,e_1\ \ e_2)$ is contra -$(\pi gb,c)$-open.

Proof: - Assume Q be $\tau_{1,2}$ - πgb - open in X, f is contra-$(1,2)^*$-$(\pi gb, bc)$- open then $f(Q)$ is $(1,2)^*$- b- closed in Υ. By (2-5)-i- we deduced $f(Q)$ is $(1\ 2)^*$- πgb-closed in Υ from the postulate ℓ is $(1,2)^*$- M*- πgb-closed, so we conclude $\ell(f(Q)) = \ell \circ f(Q)$ is $e_{1,2}$ - closed in H. Hence. $\ell \circ f$ is contra -$(1,2)^*$-$(\pi gb, c)$-open.

Proposition (3·18): If $f: (X, \tau_1, \tau_2) \to (\Upsilon, \Omega_1, \Omega_2)$ is contra-$(1,2)^*$-$(\pi gb, bc)$-open, $\ell:(\Upsilon, \Omega_1, \Omega_2) \to (H, e_1\ e_2)$ is any function and Υ, H are $(1,2)^*$- πgb- spaces, hence $\ell \circ f: (X, \tau_1, \tau_2) \to (H, e_1\ e_2)$ is contra -$(1,2)^*$- (πgb, bc)-open if ℓ is

(a) $(1,2)^* - \pi gb - closed$

(b) M-$(1\ 2)^* - \pi$gb–closed

Proof (a): Suppose Q be $(1,2)^*$- πgb- open in X from the postulate f is contra-$(1,2)^*$- $(\pi gb, bc)$-open this lead $f(Q)$ is $(1,2)^*$- b-closed in Υ. As well, by(2·5)-i- we conclude $f(Q)$ in Υ is $(1,2)^*$ πgb closed, Since Υ is $(1,2)^*$- πgb-space, then $f(Q)$ is $\Omega_{1,2}$ - closed from the supposition ℓ is $(1,2)^*$- πgb-closed this obtain $\ell(f(Q)) = \ell \circ f(Q)$ is $(1,2)^*$- πgb-closed in H, sinceH is $(1,2)^*$- πgb-space, this lead $\ell(f(Q))$ is $e_{1,2}$- closed and By (2·5)-i- we conclude, $\ell(f(Q))$ is $(1,2)^*$- b- closed in H. Hence, $\ell \circ f$ is contra-$(1,2)^*$-$(\pi gb, bc)$-open.

Point (ii) will be prove in the like method

Proposition(3·19): If $f: (X\ \tau_1\ \tau_2) \dashrightarrow (\Upsilon, \Omega_1, \Omega_2)$ is M $(1\ 2)^*$ πgb-open and $\ell:(\Upsilon, \Omega_1, \Omega_2) \dashrightarrow (H, e_1, e_2)$ is contra $(1,2)^*$-$(\pi gb, bc)$-open function, hence $\ell \circ f: (X, \tau_1, \tau_2) \to (H, e_1\ e_2)$ is contra -$(\pi gb, bc)$-open.

Proof: Assume a set $Q \subseteq X$ be$(1,2)^*$-πgb- open, then $f(Q)$ is $(1,2)^*$ πgb-open in Υ, ℓ is contra-$(1,2)^*$-$(\pi gb, bc)$-open and hence $\ell(f(Q)) = \ell \circ f(Q)$ is $(1,2)^*$-b-closed in H. Hence, $\ell \circ f$ is contra -$(1,2)^*$-$(\pi gb, bc)$-open.

Proposition(3·20): If $f: (X, \tau_1, \tau_2) \dashrightarrow (\Upsilon, \Omega_1, \Omega_2)$ is $\tau_{1,2}$ –open function, $\ell:(\Upsilon, \Omega_1, \Omega_2) \dashrightarrow (H, e_1\ e_2)$ is contra -$(1,2)^*$-$(\pi gb, bc)$-open, and X is $(1,2)^*$-πgb-space, hence $\ell \circ f: (X, \tau_1, \tau_2) \dashrightarrow (H, e_1\ e_2)$ is contra -$(1,2)^*$- (πgb, bc)-open.

Proof: Presume a set Q be $(1,2)^*$-πgb-open in X, from the supposition X is $(1,2)^*$ πgb space, hence Q is $\tau_{1,2}$- open in X, thus $f(Q)$ is $\Omega_{1,2}$ - open in Υ. By (2·5)-ii- we obtain $f(Q)$ is$(1,2)^*$-πgb- open in Υ, By imposition ℓ contra -$(1,2)^*$- $(\pi gb, bc)$-open So, $\ell(f(Q)) = \ell \circ f(Q)$ is $(1, 2)^*$– b– closed in H, therefore $\ell \circ f$ is contra-$(1,2)^*$-$(\pi gb, bc)$-open.

Definition (3·21): A function $f:(X, \tau_1, \tau_2) \to (\Upsilon, \Omega_1, \Omega_2)$ namely contra-$(1,2)^*$-$(b, \pi gbc)$-open, if $f(Q)$ is $\Omega_{1,2}$ πgb closed in $(\Upsilon, \Omega_1, \Omega_2)$, $\forall (1,2)^*$-b- open set in X.

Example(3·22): Let X $=\{\mathcal{J}\ \sigma, \ell, \mathcal{b}\}$,with $\tau_1 = \{X, \phi, \{\mathcal{J}\ \sigma\}, \{\sigma, \ell\}, \{\mathcal{J}\}, \{\sigma\}\{\mathcal{J}\ \sigma, \ell\}\}, \tau_2 = \{X, \phi, \{\mathcal{J}, \sigma, \mathcal{b}\}\{\mathcal{J}\}\}$, Suppose $f: (X, \tau_1, \tau_2) \to (X, \tau_1\ \tau_2)$ s.t $f(\mathcal{J}) = \ell$, $f(\sigma) = \mathcal{b}$ $f(\ell) = \mathcal{J}$ and $f(\mathcal{b}) = \sigma$.It is intelligibly that f is contra $(1,2)^*(b, \pi gbc)$-open.

Proposition (3·23): $f: (X, \tau_1\ \tau_2) \to (\Upsilon, \Omega_1, \Omega_2)$ is contra -$(1,2)^*$-$(b, \pi gbc)$ -open if f is

(a)contra-$(1,2)^*$-$(\pi gb, bc)$- open.

(b)contra$-(1,2)^* - (\pi gb, c)$-open.

Proof(a): Postulate $Q \subseteq X$ be $(1,2)^*$-b -open by (2.5)-ii this lead $Q \subseteq X$ is $(1,2)^*$- πgb -open Thus, $f(Q)$ in Υ is $(1\ 2)^*$-b -closed, also by(2·5)–(i) so we deduced $f(Q)$ is $(1,2)^*$-πgb-closed in Υ and hence f contra$-(1,2)^* - (b, \pi gbc)$ -open.

Proof(b): Clearly from Pro (3·10) and Pro (3·23) –point(a).

Remark (3·24): In general, the opposite of the (3·23) does not correct. Example (3-22) demonstrate this, because $\exists$ $(1,2)^*$-πgb-open set $Q = \{\sigma, \ell\}$ in X, $f(Q) = f(\{\sigma, \ell\}) = \{\sigma, \ell\}\}$ is not $\Omega_{1,2}$- closed [reps. $(1,2)^*$-b -closed] in X.

Remark (3.25): Contra-$(1,2)^*$-$(b,\pi gbc)$-open and contra $(1,2)^* -$ open functions are independent concepts. Example (3.15) and Example (3.22) demonstrate this.
The next proposition presents the stipulation that make the proposition (3.23) and Remark (3.25) correct.

Proposition (3.26): If $f:(X,\tau_1\ \tau_2)\rightarrow(Y,\Omega_1,\Omega_2)$ is contra$-(1,2)^*(b,\pi gbc)-$open, and X Y are $(1,2)^* - \pi gb -$spaces, hence f is

(a) contra $-(1,2)^* - (\pi gb, c) -$ open.

(b) contra $-(1\ 2)^* - (\pi gb, bc) -$ open

Proof(a): Postulate a set Q be $(1,2)^*$-πgb-open in X, since X is $(1,2)^*$-πgb-space, hence Q is $(1,2)^*$-open in X, by (2.5)-ii-we conclude Q is $(1,2)^*$-b-open in X, f is contra-$(1,2)^*$-$(b,\pi gbc)$- open, this lead f(Q) is$(1,2)^*$-πgb- closed in Y, From the presumption Y is $(1,2)^*$-πgb-space, this implies f(Q) is $\Omega_{1,2}$- closed in Y hence f is $-(1,2)^* - (\pi gb, c) -$ open Points (b) prove the same method.

References:

1- Dunya M. H and Messa. Z. S. Some types of (1, 2)*-M-πgb-closed mappings. Journal of the college of basic education. 2016, vol. 22. No. 95.
2- Dunya M. Hameed, Sanna. H. Jasem and Intidhar Z. Mushtt, "Types of Contra –(1,2)*-open Functions ", Journal of the College of Education, No.(2), 2021.
3- Kelly. J. C, "bitopological spaces ". Proc. London Math. Soc.1963, pp.13, 71-89.
4- Noiri.T and V. Popa. V;" Some properties of Weakly open functions in bitopologicall spaces ", Novi Sad J. Math. Vol.36, No.1, pp.47-56, (2006).
5- Ravi, O. and Lellis Thivagar, M.; "On Stronger Forms of (1,2)*-Quotient Mappings in bitopological Spaces", Int. Journal of Math. Game Theory and Algebra, Vol.14, No.6, pp. 481-492, 2004
6- Sreeja, D. and Janaki, C.; "On (1,2)*-πgb-Closed set s", Int. Journal of Computer Applications, Vol. 42, No.5, 2012.
7- Sreeja, D. and Janaki, C.; "A New Type of Homeomorphism in bitopological Spaces", Int. Journal of Scientific and Research Publications, Vol. 2, Issue 7, ISSN, 22SO-3153, July, 2012.

Influence of Laser Energy on CdTe Nano Partials Prepared by Laser Induced Plasma

Hayim Ch. Magid*, Hanaa Kadham Essa, Wasmaa Jabbar
***halhelfy@uomustansiriyah.edu.iq**

Abstract:

Cadmium telluride (CdTe) deposited on glass substrates is Using Nd-YAG laser wavelength (1064 nm) laser-induced plasma deposition technique (PLD). The structural, optical properties and morphology of these films have been described as a change the effect of laser pulse energy as in the range ($E = 400, 500, 600$ and 700 mJ). All samples showed polycrystalline hexagonal structure and with increasing laser energy, the transmittance of all deposited thin films decreases. As a result of the microscopic examination of the surface, it was found that the surface is uniform and the granular size increases with the increase of the laser power

Keywords: Cadmium telluride, Pulsed Laser Deposition, XRD, Effect the laser pulse energy.

الخلاصة

تم استخدام ابخرة البلازما المتولدة بتقنية الليزر وترسيبها على ركائز من الزجاج وتم دراسة الخصائص التركيبة والمورفولوجيا للهده الاغشية بتغير طاقة نبضة المصدر لليزر من 400 ملي جول الى 700ملي جول. اظهرت جميع العينات بنية سداسية متعددة الكريستال مع زيادة طاقة الليزر وانخفضت نفاذية جميع الاغشية الرقيقة المترسبة ونتيجة الفحص المجهري للسطح تبين انه متجانس ويزداد حجم الحبيبات بزيادة الطاقة

Introduction

Cadmium telluride (CdTe) It is in the form of a black crystalline powder. Cadmium telluride is insoluble in water, but its crystals can undergo etching with various acids, such as hydrochloric acid or hydrobromic acid, which release toxic hydrogen telluride gas [1]. Cadmium telluride crystals have a cubic structure, with the space group F43m. Cadmium telluride is transparent in the infrared range, from a band gap energy of 1.44 MeV at 300 K, which corresponds to a wavelength of 860 nm, to wavelengths greater than 20 µm, and has a characteristic fluorescence at 790 nm. When preparing cadmium telluride crystals within nanoscale dimensions, the compound becomes a quantum dot, and the fluorescence peak shifts through the visible to the ultraviolet range. It is of great importance in many applications, including detectors and solar cells. A doped cadmium telluride of the ductile type, which has a gap of (45.1) eV [2]. CdTe is also characterized by having the highest constant lattice (among other compounds). The same group is (48.6 nm), and this compound also has a direct energy gap (Gap Band Direct). Its value is (56.1) eV, and the coefficient of absorption (Coefficient Absorption) is high in the spectrum range. $\alpha > 10P$) visible is 4 $PcmP^{-1}$. [3, 4] (P) CdTe is the only compound of group VI-II that has two types

Membranes can be obtained Electrical conductivity (the acceptor and the donor) Thinner of both types according to the type and concentration of the impurity added Therefore, CdTe thin films are used in the homojunction and heterogeneous industries [5,6].

2. Experimental Procedure

Using pulsed laser ablation, high purity (99.99 per cent) cadmium oxide powder factory in FLUKA chemicals limited was used as a source for deposition of CdTe films on soda lime glass substrates (2.5x5) cm^2. The glass substratum was first treated with detergent and washed respectively in running water and alcohol concentration (96 per cent). Then,

the substrates dried with a fine tissue paper and washed in an ultrasonic cleaner with isopropyl alcohol (IPA). The powder mixture was pressed cold at 10 $^{-6}$Pa films using a hydraulic press, The CdTe thin film were prepared by sublimated plasma vapors by generating them with a Pld laser device pulsed, the 1064 nm Nd: YAG laser wavelength was used. The rate of repetition was 10 Hz and the target fluency was set at 60 J/cm^2 for all samples. At 2.5 cm, the distance from the target to the quartz substratum was preserved. For all experiments the number of shoot 100 has been preserved. The films were deposited at same substrate room temperatures. X-ray diffraction (XRD) investigated the crystal structure of 40 kV and 250 mA films with a reference Cu and a mono-chronometer. Films thickness was change with laser energy at (400mj, t=173nm), (500mj, t=162nm). (600mj, t=185nm), (700mj, t=205nm) and (800mj, t=224nm) Weighing method was used to measure film thickness with the full

$$m=2\pi\rho_m r^2 \ldots (1)$$

Where m is the mass of the substance that has been evaporated, r is the distance between the boat and the substratum, the density of the material being miss. The UV-VIS spectrophotometer was used to test optical properties of the optical transmission spectra of the deposited thin films were calculated as a function of the photon energy in the 300-800 nm wavelength range.

3. Results and Discussion

A. Structural Properties and Morphological Properties.

The (XRD) CdTe thin film X-ray diffraction patterns prepared with different laser energies show in Figure (1). All samples showed polycrystalline hexagonal structure matched with the standard card (No. 96-900-8863). Figure (4-15) shows the X-ray diffraction patterns for CdTe thin films prepared at different laser energies. All samples showed polycrystalline cubic structure corresponding to the standard card (No. 96-900-8841). Three broad peaks appeared coordinated with the lattice planes (111), (220), and (311). This result agrees with Jimenez et al [7]. The crystallinity was enhanced by increasing the laser energy. Also, the width of the peaks decreased indicates increasing the crystalline size. Table (4-5) shows the diffractioameters for the CdTe thin films prepared at different laser energies. Increasing the crystalline size with laser energy due to more laser energy enables it to remove larger masses of the target material, as well as the higher energy leads to the merging of the small particles between them [8].

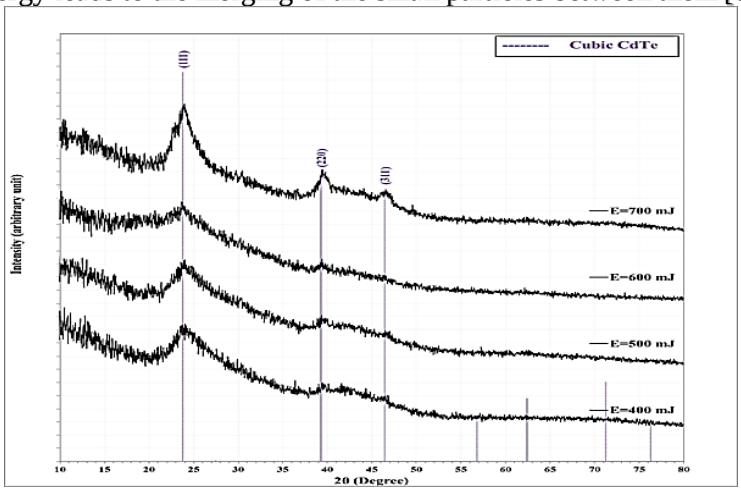

Figure (1): XRD patterns for CdTe thin films prepared using different laser energies.

Table (1): The variation of XRD parameters for CdTe using different laser energies.

E (mJ)	2θ (Deg.)	FWHM (Deg.)	d_{hkl} Exp.(Å)	C.S (nm)	d_{hkl} Std.(Å)	Phase	hkl
400	23.8252	3.4960	3.7317	2.3	3.7412	Cub.CdTe	(111)
	39.5573	1.9863	2.2764	4.3	2.2910	Cub.CdTe	(220)
500	23.9047	3.4960	3.7195	2.3	3.7412	Cub.CdTe	(111)
	39.3190	1.4302	2.2896	5.9	2.2910	Cub.CdTe	(220)
600	23.7457	2.4631	3.7440	3.3	3.7412	Cub.CdTe	(111)
	39.3984	1.4302	2.2852	5.9	2.2910	Cub.CdTe	(220)
700	23.9047	2.3042	3.7195	3.5	3.7412	Cub.CdTe	(111)
	39.4779	0.8741	2.2808	9.7	2.2910	Cub.CdTe	(220)
	46.5494	1.3507	1.9494	6.4	1.9538	Cub.CdTe	(311)

Three dimensional surface morphology prepared at different laser energies AFM images and the cumulating distribution for particle diameters of CdTe thin films surface prepared at different laser energies illustrate in Figure (2). The sample prepared with the lowest energy has uniformly distributed as shown by the 3D image and the cumulating histogram. Increasing laser energy cause to increase in the average particle size and roughness, in addition, the particle distribution became irregular.

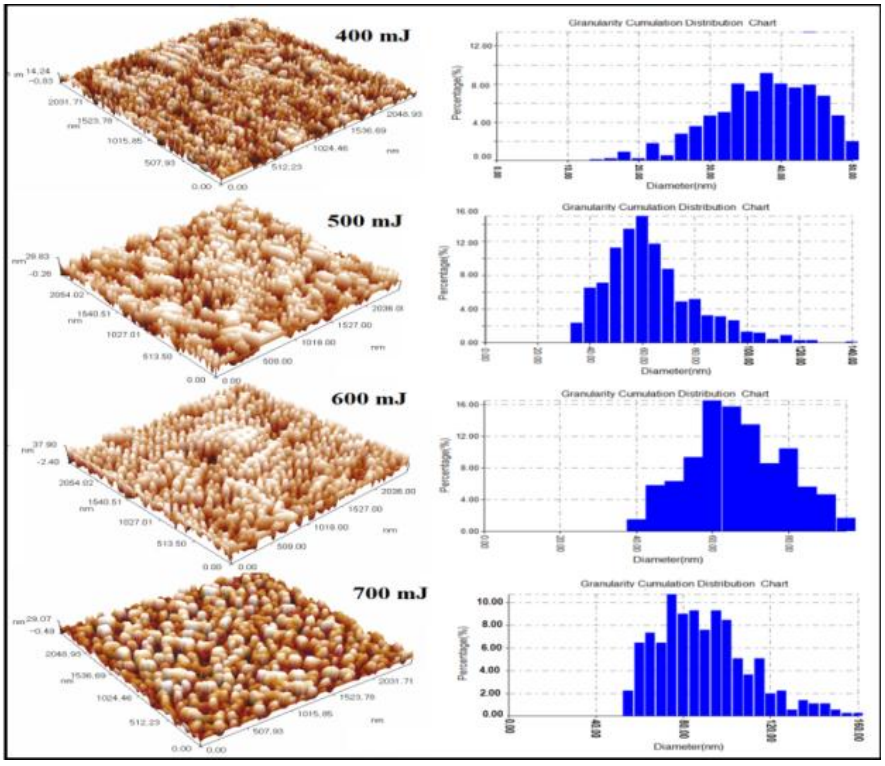

Figure (2): AFM images for CdTe thin films surface prepared using different laser energy.

The table (2) consist the parameters of AFM for CdTe thin film prepared at different laser energies Average Diameter, Average roughness and RMS roughness.

Table (2): AFM parameters; Average Diameter, Average roughness and RMS roughness for CdTe thin film prepared at different laser energies.

Laser energy (mJ)	Average diameter (nm)	Average roughness (nm)	RMS roughness (nm)
400	38.26	3.77	4.35
500	60.95	7.27	8.4
600	64.21	7.39	8.53
700	86.85	10.1	11.6

Figure (3) shows the cross-section images of the field emission scanning electron microscope (FESEM) for the CdTe thin films prepared at different laser energies on glass substrates at two magnification powers (60 kx and 15 kx). The film prepared at low energy appeared with small particles. Increasing laser energy cause to increase in the sample density and the samples seem like a solid behavior.

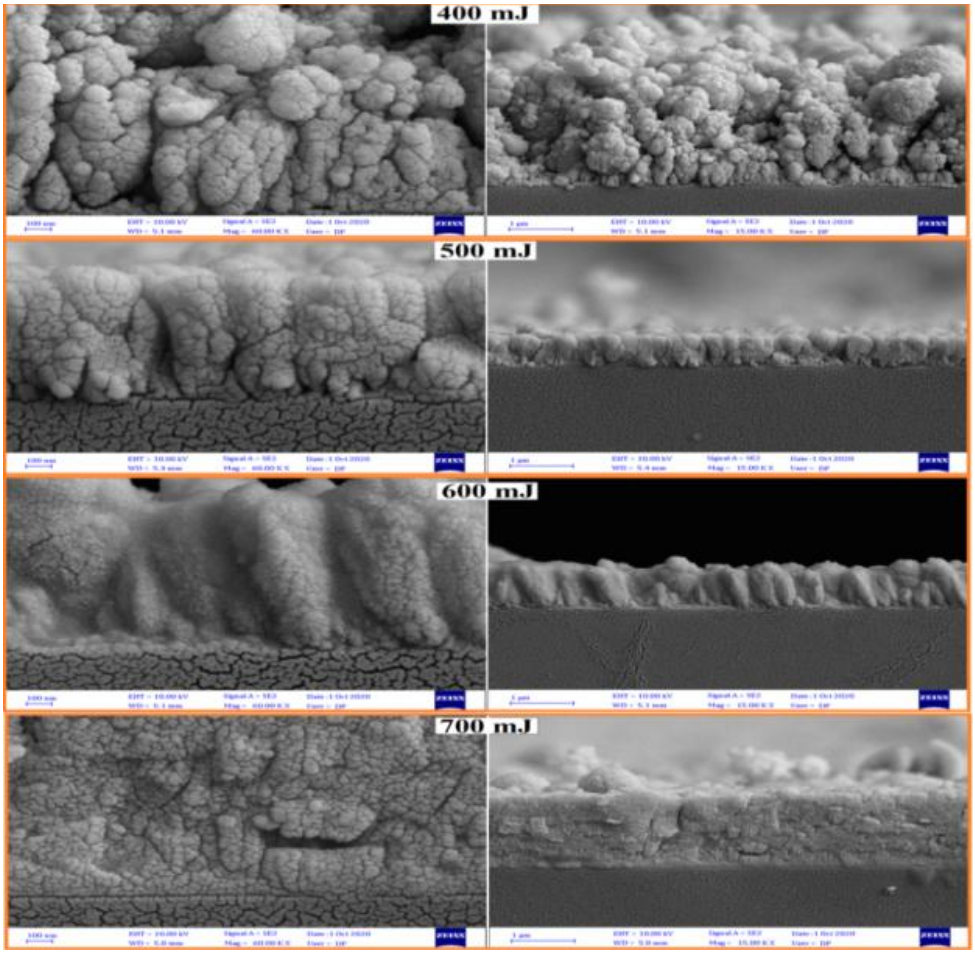

Figure (3): Cross-section view of SEM images for CdTe thin films on glass substrates at two magnifications using different laser energy.

B. Optical Properties

1-transmission: Optical properties of CdTe thin films are deducing from transmission (T) spectra of the thin films deposited on glass substrate using the UV-visible spectrophotometer. The optical characteristics involve; the coefficient of absorption (α), the optical energy gap (E_g), studied within the range (300-800) nm.

The transmission spectra of CdTe thin film prepared at different laser energies (x= 0.2, 0.4 and 0.6) shown in Figure (4). the transmittance increases with decreasing laser energy for CdTe thin film. As seen from figures the typical transmittance is found within the range (45%-85%) which is good for Opto-electronic applications, especially for photovoltaic cell window layers. The upper transmittance is often attributed to less scattering effects, structural homogeneity and better crystallinity [14]. Furthermore, sharp fall at band edge is a sign of excellent crystallinity of CdTe within the thin films.

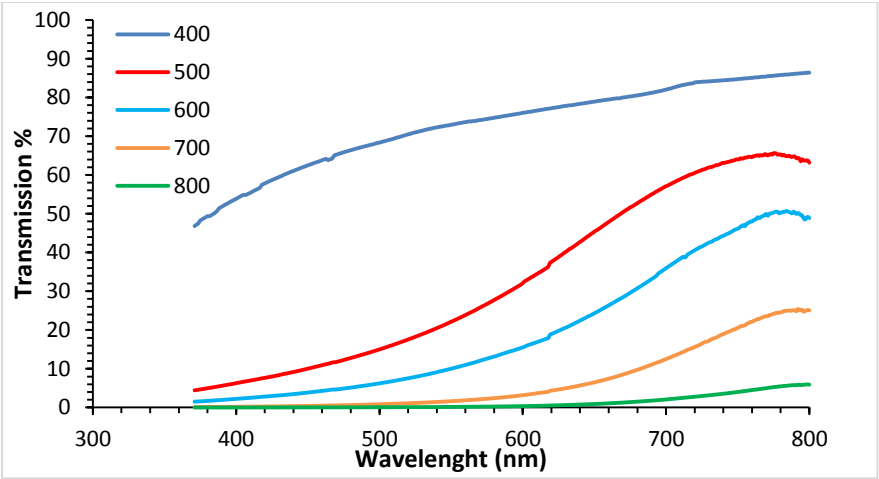

Figure (4). Transmittance spectra as a function of wavelength for CdTe films deposited at different laser energies

2. The Optical Energy Gap

As the energy divide has widened, a fundamental and very important role in determining the applications of the membrane used, for example in detectors and solar cells, must be greater than the energy gap of the base.

The allowed direct energy gap is determined by plotting $(\alpha h\upsilon)^2$ as a function of photon energy has been determined by using Tauc equation. The optical energy gap (E_g^{opt}) is then determined by the extrapolation of the portion at $(\alpha h\upsilon)^2 = 0$ and selecting the optimum linear part.

Figures (5) show the energy gap values of thin films (CdTe) at different energies of the laser device, which shows the decrease in the energy gap with the increase in the energy of the source for all samples and this occurs due to the increase in the crystal size or due to the change of the lattice constant, also is due to the grain growth and the decrease in defect states near the bands and in turn decreasing the value of E_g [12], as there is an inverse relation between grain and E_g in nano size.

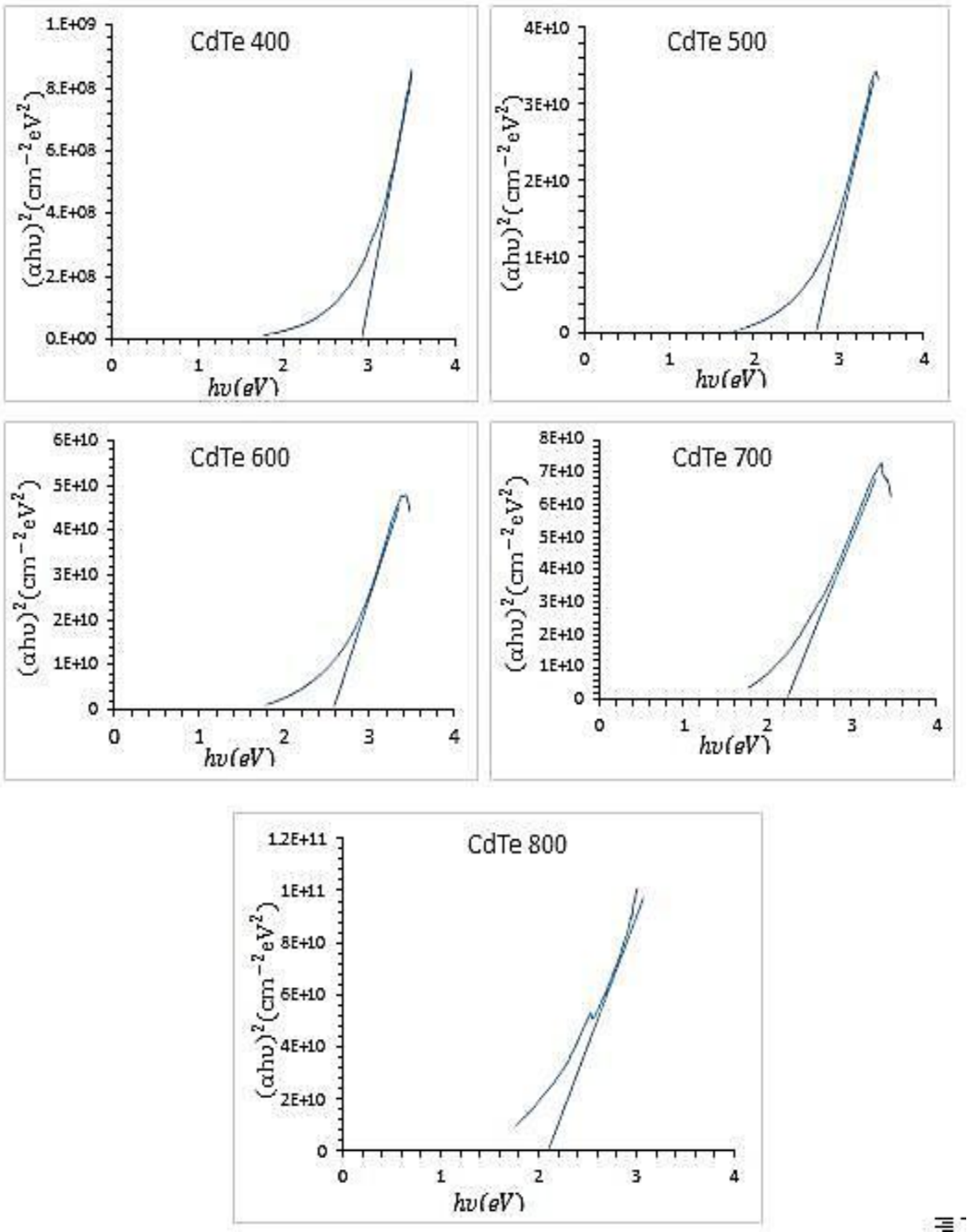

Figure (5): Tauc relation for CdTe thin film prepared at different laser energies.

Conclusions

CdTe films with a thickness of (200nm) were fabricated on glass substrates by laser induced plasma method. Films were prepared in vacuum at room temperature. Films were investigated by XRD, AFM, SEM optical transmittance spectra and energy gap. Based on the above results, the following conclusions can be drawn:

1- The CdTe films have a many peaks appeared to conform the lattice planes (100), (002), (101), (102), (110), (103). It is also evident that the peak's intensity increases while the peaks width is decreases with rising laser energy indicates on increasing the crystallinity and growing crystalline size.

2- Increasing the laser pulses energy cause to increase in the average size and the surface roughness as shown.

3- Generally, with increasing laser energy, the transmittance of all deposited thin films decreases and also the energy gap decrease for all samples and this occurs due to the increase in the crystal size or due to the change of the lattice constant.

References

1. Sinha, Parikhit; Kriegner, Christopher J.; Schew, William A.; Kaczmar, Swiatoslav W.; Traister, Matthew; Wilson, David J. "Regulatory policy governing cadmium-telluride photovoltaics: A case study contrasting life cycle management with the precautionary principle". Energy Policy 36:381 (2008).

2. G. H. Tariq and M. Anis-ur-Rehman. "Effects on structural Electronic Transport & Optical properties of doped & undoped ZnTe thin films for CdTe/CdS Solar Celles" Key Engineering Materials Vol.510, pp. 89-97,(2012).

3. J. Heo, H. Thn, R. Lee, Y. Han and D. Kim, "Solar Energy Materials and Solar Cells", vol. 75, pp. 193-203, (2003).

4. S. Franssila,"Introduction to Micro fabrication", John Wiley and Sons, England, (2004).

5. M. Bayhan, "Structural and Optical Characterization of Vacuum Deposited CdTe Thin Films" Tr. J. of Physics, No. 22, vol. 929, (1998).

6. Juan Hou, Hai Bin Cao, Xu chu Huang, Chun Yan Song "EDS, XRD and Raman Scattering study of Dy ion implanted CdTe polycrystalline thin films", Advanced Material Research, Vol. 213, pp157-160, (2011).

7. J. Fred O'Shay. "Time-Resolved Visible and Extreme Ultraviolet Spectroscopy of Laser- Produced Tin Plasma", Ph.D. Dissertation, University of California, San Diego USA, (2007).

8. V. K. Unnikrishnan, K. Alti, V. B. Kartha, C. Santhosh, G. P. Gupta, and B. M. Suri. "Measurements of plasma temperature and electron density in laser-induced copper plasma by time-resolved spectroscopy of neutral atom and ion emissions", Pramana J. Phys., vol. 74, no. 6, pp. 983-993, (2010).

Formation Layers Like Artichoke Tree in Triangular Pores by using Red Laser Illumination

Hasan A. Hadi[1], Sarab T. Kasim[2]
[1]Department of Physics, Education College, Mustansiriyah University
[2]Educational Rusafa Directorate II, Baghdad, Iraq

Abstract:

In this study, porous silicon layer were formed using photo electrochemical etching (PECE) with a red laser assist. The structural properties of porous silicon were one of the study's main topics as well. The triangular model pores are confirmed by SEM, elucidating the orientation dependence of the (111) n-Si wafer. This orientation dependence may be caused by anisotropy of Si disintegration, leading to porous silicon growth like a tree or an artichoke.Energy-dispersive X-ray spectroscopy (EDS) showing that the spectrum of the porous silicon layer, containing O (8.2%) and Si (91.8%) ratio. X-Ray diffraction (XRD) pattern showed the one peak was detected at of $2\theta \approx 28.47°$. Fourier transform infrared (FTIR) spectrum showed the most of bands mode in the range of 400 to 4000 cm^{-1} were vibration stretching mode. Atomic force microscopy (AFM) characterization showed that the value of Ten Point Height Sz., Root mean square Sq., and Roughness Average Sa. of the artichoke layer surface were 26.6, 6.26, and 5.28 nm respectively.

Keyword: Porous silicon, Photoelectrochemical etching PECE, EDS, FTIR, XRD.

الخلاصة

في هذه الدراسة، تم الحصول على طبقة السيليكون المسامي بواسطة عملية التنميش الكهروكيميائي الضوئي وباستخدام الليزر الاحمر. هدف الدراسة الرئيسي تبيان خصائص السيليكون المسامي التركيبية. اذ تم تاكيد نموذج المسام المثلثي بواسطة مجهر الماسح الالكتروني والذي يوكد اعتمادية شكل المسام على الاتجاهية لقاعدة السيليكون (111).ان تباين الخصائص للسيليكون ادت الى نمو سلييكون مسامي يشبه الشجرة او الخرشوف. اظهر التحليل الطيفي للطاقة ان نسبة الاوكسجين هي 8.2% والسيليكون 91.8% نمط حيود الاشعة السينية اظهر قمة واحدة عند زاوية 28.47 درجة. طيف تحويلات فوريه للاشعة تحت الحمراء بين ان اغلب انماط الاهتزاز الحزم في مدى الاعداد الموجية من 400 الى 4000 cm^{-1} هو تمدد (امتطاط) الاهتزاز. مجهر القوة الذرية بين ان قيم Sq, Sz وSa لطبقة الخرشوف هي 26.6, 6.26 و5.28 نم على التوالي

الكلمات الرئيسية: السيليكون المسامي، التنميش الكهروكيميائي الضوئي PECE، EDS، FTIR، XRD.

Introduction:

It is one of the more advanced stages of silicon, consisting of a collection of nanoscale gaps that can form when the crystal silicon is etched using a variety of electrical techniques, including electrochemical etching and photo-electrochemical etching, in an electrolyte solution with a base of hydrofluoric acid that has been diluted with (distilled water, ethanol, and methanol) for the anode [1, 2]. It caught the attention of experts when it was revealed that porous silicon has a high brightness at room temperature, and it is notably thought of as a basic material in the construction of electronic devices [3]. Following the discovery of the quantification mechanism and the impact of PSi surface on the properties of porous silicon, focus has shifted to the surface chemistry of porous silicon and applications of chemical sensors, where knowledge of the size, direction, and distribution of the pores as well as the conditions under which porous silicon was prepared is crucial [4]. In the nano scale, porous silicon is a semiconductor crystal that enhances various silicon characteristics. Porous silicon has a wide surface area, especially in earlier

years, which contributes to its high level of interest [5]. A top-down manufacturing procedure is used to produce porous silicon by etching pores into crystalline silicon. The structure of porous silicon can be modified to provide a wide variety of purposes due to the versatility of the preparation conditions. The current work aims to prepare porous silicon layers on n-type silicon wafers using electrochemical etching, formation layers with triangular pores like those of an artichoke tree under red laser illumination, and then characterize the structural and optical features.

Experimental part:

1. Photo Electrochemical Etching

Photo-electrochemically etching (PECE) an n-Si wafer in an electrolyte of HF 48%: 99% ethanol, was used to create a PS layer. The electrical resistivity of the single-crystal Si was in the range of (1~10) Ω.cm and it was (111) oriented. Methanol and distilled water were utilized to clean the silicon wafer, followed by an ultrasonic bath and drying in a hot air stream. The wafer was anodized for 12 minutes at a constant etching current density while being illuminated by a laser diode with a 650 nm wavelength and 53 mW of power. As shown in figure 1 in this case by illuminating n-type substrates surface of the wafer. Illuminating n-type substrates surface by the diode laser (red-650nm) to etch an area $\cong 0.2826 cm^2$, using a concave lens to spread the light evenly on the sample, were the distance between the lens and the laser source was 2 cm and the distance between the lens and the sample was 55 cm. Diagram of the etch cell used to prepare Psi (PECE).

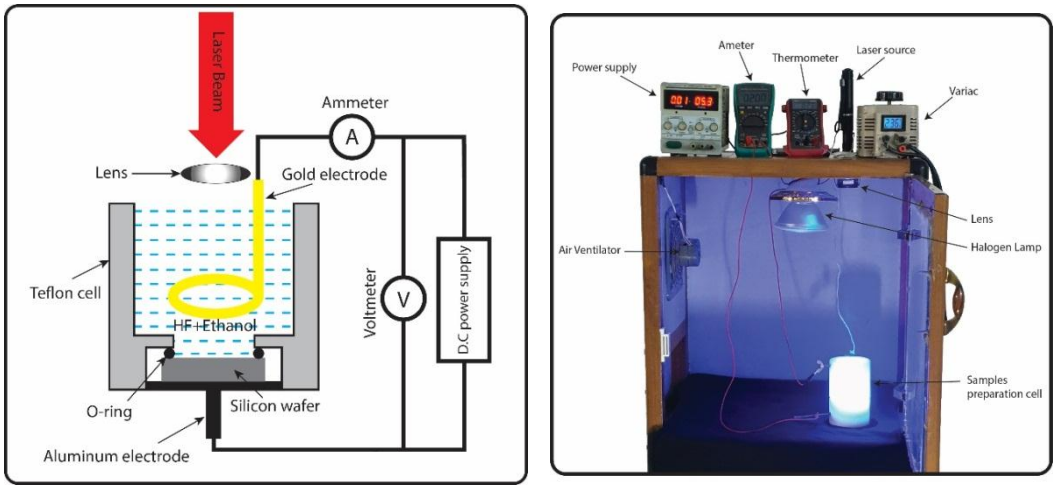

Figure 1: Photograph of the porous silicon fabrication system(PECE).

2. Result and dissection

The thickness and porosity of the PS layer, as determined by gravimetric measurements and the following equation:

$$t = m_1 - m_2 / A \times \rho \quad \ldots (1)$$

Where A is the Sample effective area is etched and ρ is the density of Si [6].

The porosity is defined as the fraction of void within the PS layer and can be determined easily by weight measurements from following equation [7].

$$P\% = \frac{m_1 - m_3}{m_1 - m_2} \quad \ldots (2)$$

The virgin wafer is first weighed before anodization (m_1), then just after anodisation (m_2) and finally after dissolution of the whole porous layer in a molar KOH aqueous solution

(m_3). Uniform and rapid stripping in the KOH solution is obtained when the PS layer is covered with a small amount of ethanol which improves the infiltration of the aqueous KOH in the pores. The PS 1ayers' thickness and porosity were found to be (5.2 - 9.1)% m and (54 -77)% m, respectively. The XRD pattern of the substrate silicon wafer (n-Si) is shown in Figure2 and one peak is detected at 28.46° with full width at half maximum of 0.19. Formation of nanostructure of porous silicon layers was confirmed by a decrease in the intensity peak values and widening in full width half maximum FWHM. As expected the structure of the porous silicon layer which most often behave like an almost single crystal. One XRD peak was detected at of 28.47 with full width at half maximum of 0.2256 corresponded (111) for red laser and that agree with similar results were reported [8,9].

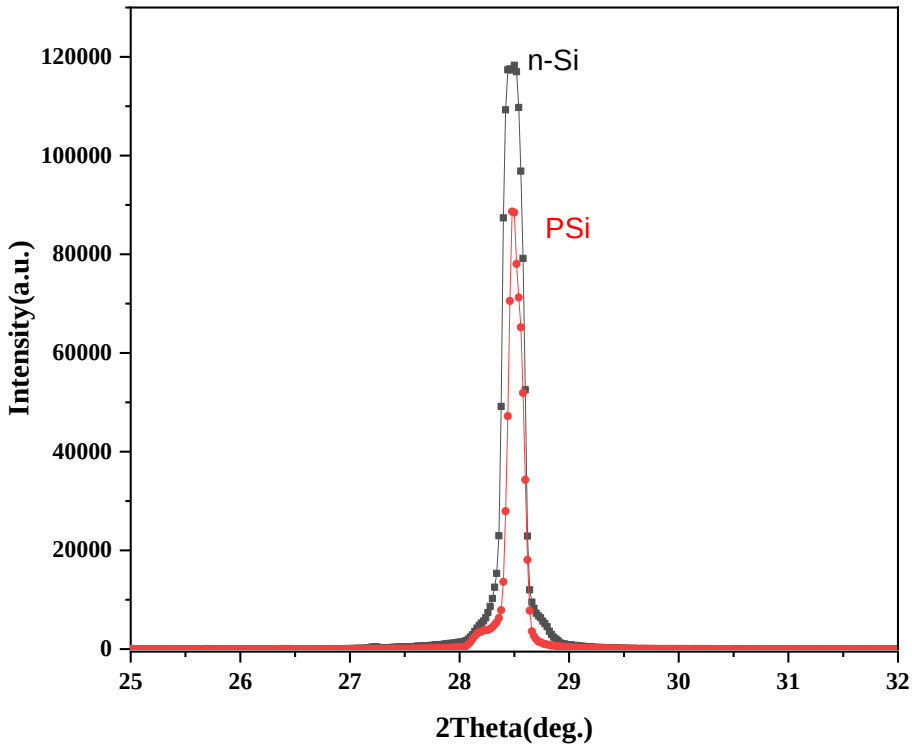

Figure 2: X-ray diffraction of bulk silicon n-Si (black line) and porous silicon layer PSi (red line).

Figure 3 show that FTIR transmission spectrum of the porous silicon layers prepared at red laser light in the range of 400 to 4000 cm^{-1} wavenumber. The band between 2140-2158 cm-1for the Si-H Vibration Stretching in Si-O_2- SiH molecule and the band at about 2240-2262 cm^{-1} for Vibration Stretching of Si-H in the O_3-SiH molecule. As for the band at around 2933-2923 cm^{-1} is caused by the Stretching Vibration of the CH in group CH_2, while the band at about 3374-3419 cm^{-1} is attributable to the Stretching Vibration-H in the SiOH groups and these results close to our results have been identified [10].

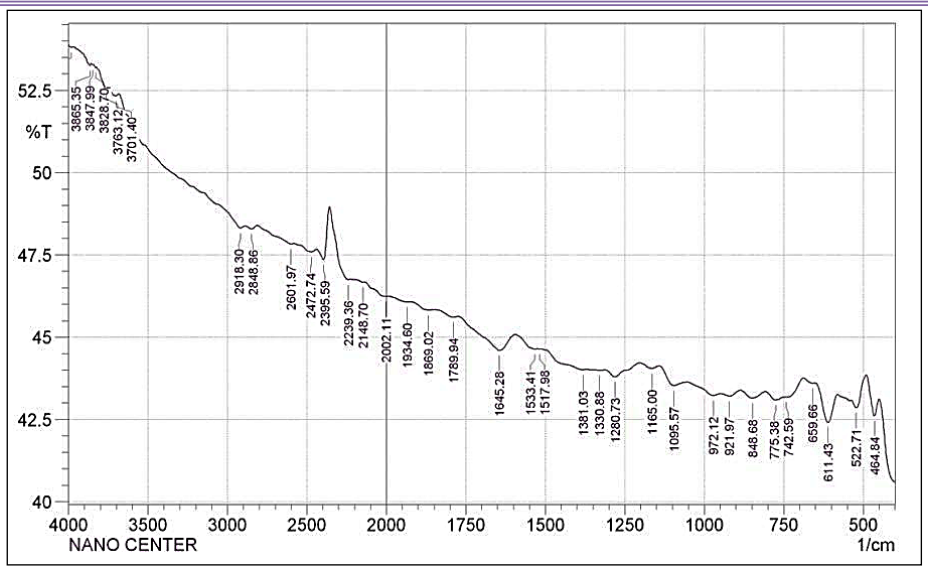

Figure 3: Transmission Fourier transformation infrared spectra of porous silicon.

Figure4 shows 2D and 3D atomic force microscope images of porous silicon layer sample was formed with red laser source illumination. Amplitude parameters from Figure(4.a) showed that the value of Ten Point Height Sz., Root mean square Sq., and Roughness Average Sa. of the porous silicon layer surface were 26.6, 6.26, and 5.28 nm respectively. From The histograms of Height and granularity distribution charts, the average height and diameter of porous silicon layers were 21.14 and 41.12 nm respectively as shown in Figure (4,b and c).

In this section of structural and morphology study and shown in the figure 5, the scanning electron microscope (SEM) measurements have been used to describe the illumination condition effect on the morphology of porous silicon layers. Material synthesis and concentration ratio of the porous silicon layer sample were specified using Energy-dispersive X-ray spectroscopy (EDS). It is well known that the Energy-dispersive X-ray spectroscopy (EDS) can be identified elemental composition by peak-height ratio and also suppose that the deepness of pores in the porous silicon layers according to the oxygen percentage in the crystal structure.

Figures 5-a and 5-b showed that SEM micrograph of the porous silicon layer is preparing by using a red laser with 353 mw/cm^2 power density with 100×100 and 200×200 nm magnification. Triangular model pores clarifying orientation reliance of the (111) n-Si wafer, perhaps consequent to the anisotropy of Si disintegration so porous silicon growth like a tree or artichoke. The grain size ranges from 39 to 400 nm with an average grain size of 220nm, EDS spectrum of the porous silicon layer, containing O (8.2%) and Si (91.8%) ratio.

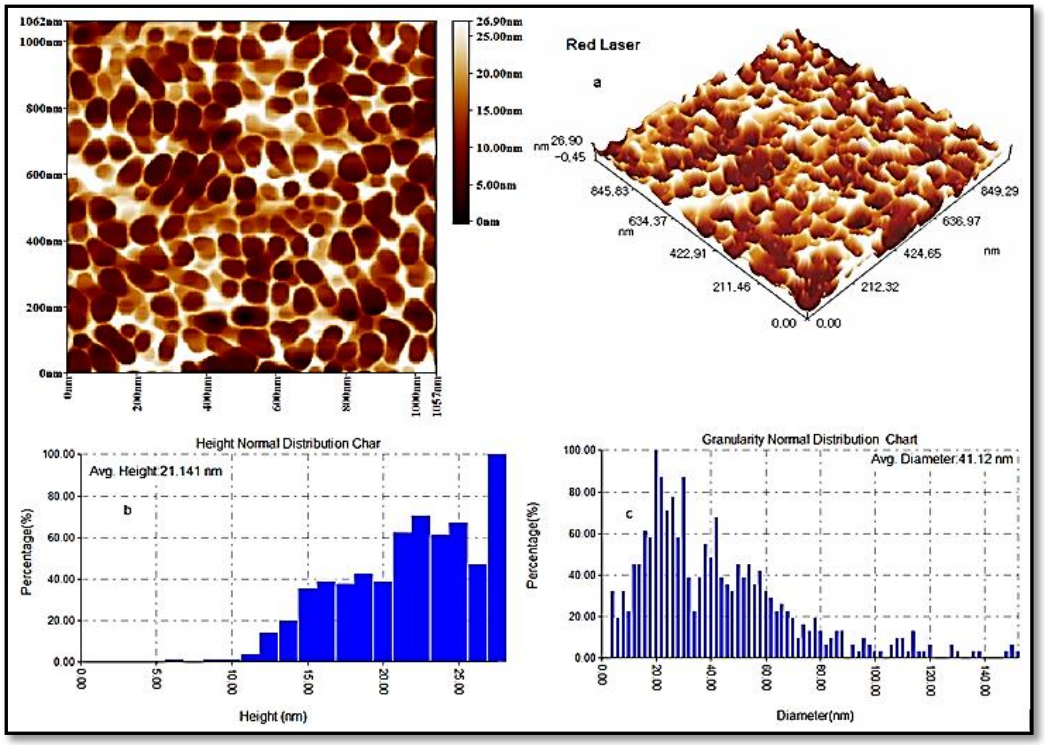

Figure 4: Two and three-dimensional view of AFM of a fresh porous silicon sample (red laser illuminated) (a), the histogram of heights normal distribution (b), and the histogram of granularity normal distribution (c).

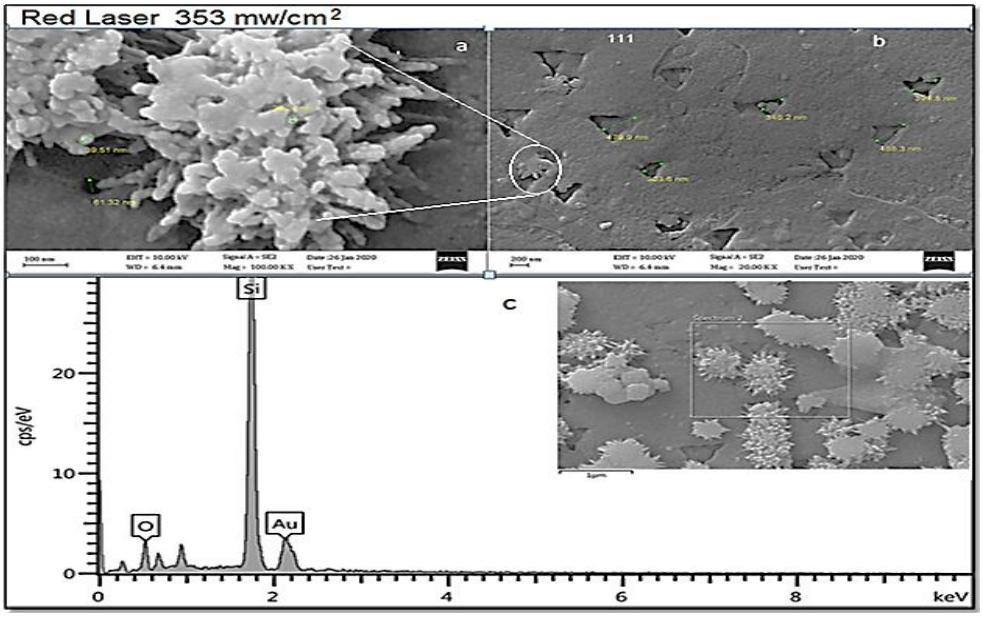

Figure 5: (a), (b) shows SEM micrograph of the porous silicon layer is preparing by using a red with 353 mw/cm^2 power density with 100×100 and 200×200 nm magnification, while (c) EDS spectrum of the porous silicon layer, containing O (8.2%) and Si (91.8%) ratio.

From SEM, the varying shapes and sizes of the grains agglomerate from porous silicon formation showed the effect of the wavelength and illumination intensity of the light source was used during the electrochemical etching.

The photoluminescence PL spectra were recorded to porous silicon layer, the peaks were observed at λ=580nm corresponded to energy of 2.34eV and the full width at half maximum FWHM 12.37nm when used a red laser in electrochemical etching process respectively as shown in Figure 6. Due to the nanostructure of porous silicon layers and according to the quantum confinement effect, we can interpret why photo luminance spectra PL peak shifted toward to blue shift in the visible region for samples prepared under illuminated at a red laser wavelength.

It was found, in general, that it had a small thickness and a high porosity which led to a significant increase in the intensity of PL with blue shift.

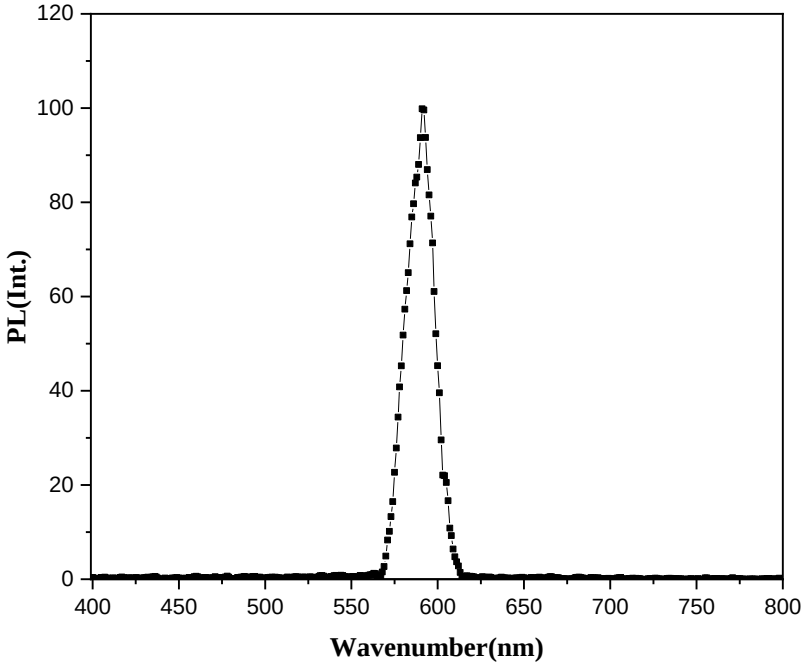

Figure 6: PL spectra of nanostructures PSi on illuminations 353mw/cm^2 red laser power density.

Conclusion:

Porous silicon was created by photo electrochemical etching. Illumination conditions were employed to control the regrowth method PECE and decrease defect. The SEM examination revealed triangular pores with porous silicon PS growth like a tree or artichoke. The average grain size of the porous silicon layer's was 220 nm and that the range of grain sizes from 39 to 400 nm. The wide PL spectrum of the PS makes them appropriate provenance for optoelectronic applications.

References:

1. Sarab T. , Hasan A. Hadi, **Illumination condition effect on properties of nano porous silicon for optoelectronic application**, MSc. thesis, Mustansiriyah university 2020,Iraq.

2. Layla Alag Wali, **"SERS of Silver Plated-Porous Silicon for Chemical Sensing Applications"**, A Doctor thesis, Al-Mustansiriya University, (2017).

3. S. Basu, **"Crystalline Silicon: Properties and Uses"**, In Tech, (2011).

4. M. Beale, N. Chew, M. Uren, A. Cullis, and J. Benjamin, **"Microstructure and formation mechanism of porous silicon",** Applied Physics Letters, vol.46, pp. 86 (1985).

5. Duaa Jabbar Hussein, Muneer H. Jaduaa Alzubaidy, Ahmed N. Abd, **"Fabrication and Characterization of Porous Silicon",** World Scientific News An International Journal, Vol. 94, No. 2, pp. 321-328, (2018).

6. Hasan A. Hadi, Raid A. Ismail, Nahida J. Almashhadani, **"Preparation and Characteristics Study of Polystyrene/Porous Silicon Photodetector Prepared by Electrochemical Etching"** Journal of Inorganic and Organometallic Polymers and Materials, Vol. 29, pp. 1100–1110, (2019).

7. Olga Volovlikova , Sergey Gavrilov and Petr Lazarenko, **"Influence of Illumination on Porous Silicon Formedby Photo-Assisted Etching of p-Type Si with a Di_erent Doping Level'',** Micromachines **2020**, 11, 199; doi:10.3390/mi11020199.

8. Hasan A. Hadi, Faten Sh. Zain Al-Abedeen, **"Comparative Study in Optoelectronic Properties between Nano Gold/ Porous Silicon Heterojunction Based on P and N-Type Crystalline Silicon"**, International Journal of Emerging Research in Management & Technology ISSN: 2278-9359 (Vol. 3, Issue 11), 2014.

9. Abdulkahlig A. Sulaiman, "**Effect of γ- Irradiation on the n-Porous Silicon Structures Prepared by Electrochemical Etching",** Raf. J. Sci., Vol. 27, No.3, pp.173-180, 2018.

10. Majid S. Jabir, Uday M. Nayef , Kareem H. Jawad , Zainab J. Taqi , Buthenhia A. H and Nada R. Ahmed, **"Porous silicon nanoparticles prepared via an improved method: a developing strategy for a successful antimicrobial agent against Escherichia coli and Staphylococcus aureus**", IOP Conf. Series: Materials Science and Engineering 454 (2018) 012077 doi:10.1088/1757-899X/454/1/012077.

Copper and Nickel Oxide Nanostructures' in Vitro Antibacterial and Anticancer Activities in Human Breast Cancer 7 Cells of the Michigan Cancer Foundation

Zainab Ali Hrbe[*1], Muneer H. Jaduaa Alzubaidy[2], Ahmed N. Abd[3]
[1,2]**Department of Physics, College of Science, Wasit University, Iraq.**
[3]**Department of Physics, College of Science, Mustansuria University, Iraq.**
[1*]**E-mail: zainabali@uowasit.edu.iq**

Abstract:

Using Nd-YAG pulse ablation, copper oxide and nickel oxide nanoparticles were produced and subsequently examined as colloidal solutions. Transmission electron microscopy (TEM) and Fourier transform infrared spectroscopy (FTIR) were used to examine the nano-particles for UV-VIS absorption. The FTIR analysis demonstrates the formation of copper oxide and nickel oxide nanoparticles. The UV-VIS absorption tests are below. According to TEM, the sizes of the nano-particles ranged from (75) nm for a copper-nickel. According to FE-SEM analysis, copper-nickel nanoparticles with a size of (53.91) nm indicated antibacterial activity. In addition, the human breast cancer MCF-7 cell line has significant anticancer activity.

Keywords: pulsed laser ablation in liquid, metallic oxide nano-particles, SEM anticancer, antibacterial activity.

خلاصة:

باستخدام الاستئصال النبضي Nd-YAG، تم إنتاج جزيئات أكسيد النحاس وأكسيد النيكل النانوية وفحصها لاحقًا كمحلول غرواني. تم استخدام المجهر الإلكتروني للإرسال (TEM) والتحليل الطيفي للأشعة تحت الحمراء (FTIR) لفحص الجسيمات النانوية لامتصاص الأشعة فوق البنفسجية. يوضح تحليل FTIR تكوين أكسيد النحاس وجسيمات أكسيد النيكل النانوية. فيما يلي اختبارات امتصاص UV-VIS. وفقًا لـ TEM، تراوحت أحجام جزيئات النانو من (75) نانومتر للنيكل والنحاس. وفقًا لتحليل FE-SEM، أشارت جزيئات النحاس والنيكل النانوية بحجم (53.91) نانومتر إلى نشاط مضاد للجراثيم. فضلا عن ذلك، فإن خط خلايا سرطان الثدي البشري MCF-7 له نشاط كبير مضاد للسرطان.

الكلمات المفتاحية: الاجتثاث بالليزر النبضي في السائل، جزيئات أكسيد المعادن النانوية، SEM مضاد للسرطان، نشاط مضاد للجراثيم.

1. Introduction

Copper oxide (CuO), a P-type semiconductor with a band gap of 1.21-1.51 eV is regarded as one of the preferable oxides. Metal oxides are the most versatile class of materials, having properties that cover every facet of chemistry and physics [1]. Copper oxide semiconductors exhibit great optical absorption, is non-toxic, and affordable to manufacture. Furthermore, breakthroughs in nanoscience and nanotechnology have created new opportunities to investigate the bactericidal effects of innovative nanomaterials containing metals known for their apparent bioactivities, such as Cu and Ni. [2-6]. The biological effectiveness of metal-based nano-antimicrobials has been demonstrated to be significantly longer or higher than the (standard) bio-activity of the actual bulk metal, which was thought to be the result of several factors, including non-traditional properties related to the presence of surface stabilizers, size-dependent properties of nano-metals, and the high surface-to-volume ratio. Capping chemicals have consistently been found to modify nanoparticle ionic release and, as a result, anti-biofilm properties. The need for clean living conditions has created new obstacles in producing efficient and cost-effective antimicrobial materials that must be completely safe for people

and ecologically friendly. This presently boosts the influence of "smart" nano-antimicrobial [7]. Nickel oxide has a semitransparent and stable structure, a high direct band gap, and p-type semiconducting activity with weak absorption bands [8-9]. NiO thin films are appealing materials that have the potential to be employed as functional sensor layers for chemical sensors, antiferromagnetic layers, and active electrodes in electrochromic devices, and electrochromic devices [10-12]. Sputtering, pulsed laser deposition, thermal evaporation, spray pyrolysis, electron beam evaporation, dip coating, spin coating, and electro-deposition are all physical and chemical deposition methods that may be utilized to make NiO thin films [12-15]. The project's purpose is to use laser ablation to create CuO and NiO nanoparticles for medical applications such as (cancer).

2. Experimental Works

Nickel oxide and copper oxide were generated by laser ablation of 99.99% pure nickel powder pellets in distilled water (provided by Poch Company) at room temperature. Grinding the target materials (Ni and Cu) and then crushing and pulverizing them in a piston to form a circular disk produces the target materials (Ni and Cu). The water used in the experiment is distilled water (DW), which has the chemical formula H_2O and a density of 1 g/cm^3, and it has the benefit of being a good solvent for most organic colors as well as a neutral solvent. Where were prepared glass bases with dimensions (2.5x2.5) cm and were cleaned with distilled water and then dried with a special blotting paper, and then cleaned with high purity ethyl alcohol (99,99) for (15) minutes, washed with a special blotting paper, and cleaned with distilled water after it cleans the floors to be ready, as shown in figure 1. The colloidal solution made by the (PLAL) technique is then deposited on the glass bases by distilling the colloidal solution over those glass bases using an electric heater set to (60)^{o}C, so the liquid evaporates after NPS is coated on the glass bases, as illustrated in figure 2. Figure 1 depicts a schematic representation of laser ablation in a liquid environment. Fourier transformation infrared spectroscopy, JEOL (JSM-5600) scanning electron microscopy, Philips CM10 PW 6020 transmission electron microscopy, Angstrom AA 3000 atomic force microscopy, and Cary 100 Conc plus UV-Vis's spectrophotometer were used to investigate the structural, morphological, and optical properties of NiO, CuO, and NPs. Colloidal NiO and CuO nanoparticles were deposited on a glass substrate by drop casting. Cu: Ni material was produced and dried for 30 minutes at 400 degrees Celsius before being milled into a powder.

3. Results and Discussion

Figure 3 depicts an (FE-SEM) image of a Cu: Ni nanoparticle created by distillation and placed on a glass substrate, revealing a Cu: Ni particle morphology with a spherical form. It also boasts a large number of corporations. Indicates the size of the nano-particles is between (53.91) nm.

FTIR spectroscopy is a particularly useful tool for investigating the vibrational properties of synthetic materials. Thin films' band positions and absorption peaks are influenced not only by their chemical composition and structure but also by their form. The FTIR spectrum of a Cu:Ni thin sheet is shown in Figure 4. The Cu:Ni stretching vibrations are responsible for the 578 (1/cm) absorption band. Weak peaks at 1631 cm^{-1} are attributed to symmetric and asymmetric C=C bond beats, respectively, as well as O-H at 3317 (1/cm).

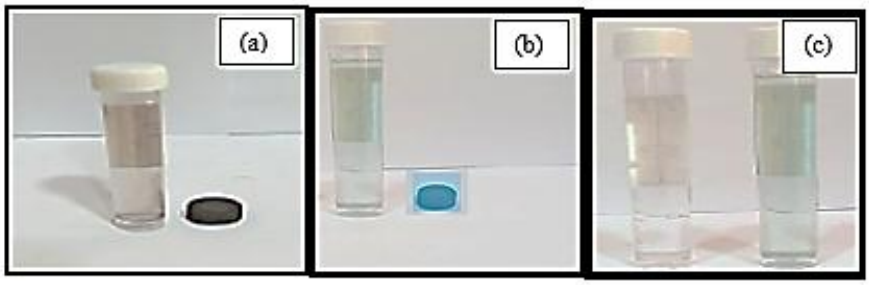

Figure (1): (a)fresh colloidal NiO NPs induce by Laser ablation in liquid and the ballet .(b) fresh colloidal CuO NPs induce by Laser ablation in liquid and the ballet . (c) fresh colloidal CuNi NPs induce by Laser ablation in liquid and the ballet.

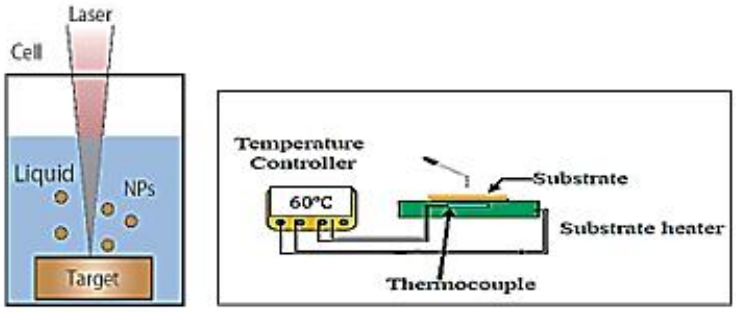

Figure (2): shows the precipitation of the solution on a glass substrate.

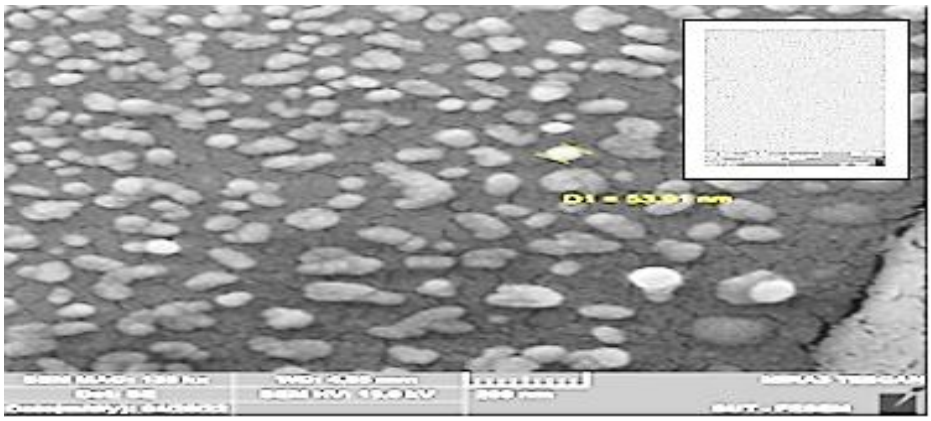

Figure 3: FE-SEM image of Cu: Ni nanostructure.

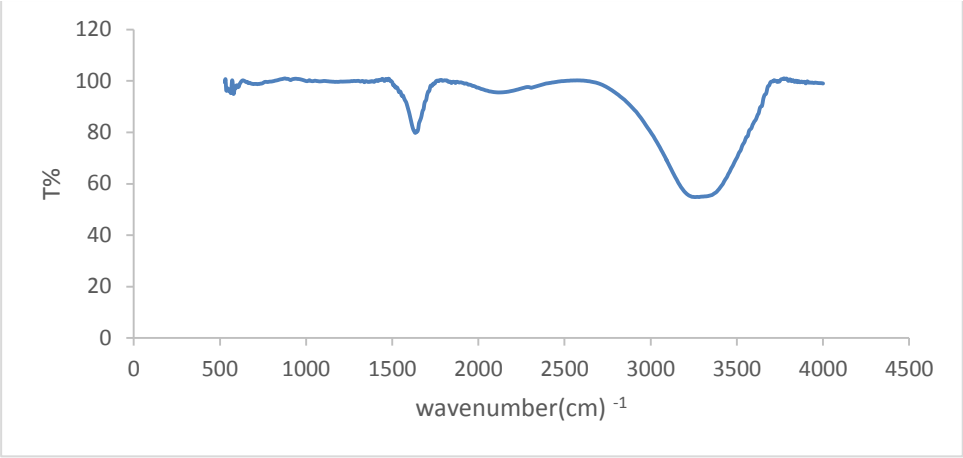

FTIR spectrum of nano-scale Cu:Ni particles: Figure4

A transmission electron microscope (TEM) picture of a (Cu:Ni) nanoparticle solution generated by laser ablation is shown in Figure 5. The TEM picture shows that the development of NPs (Cu:Ni) with a diameter of 75 nm reveals the quantitative size of nano-particles, which portray the form of rod particles. The size of the nano-particles formed during the laser ablation process is determined by the solvent and the quantity of laser energy employed.

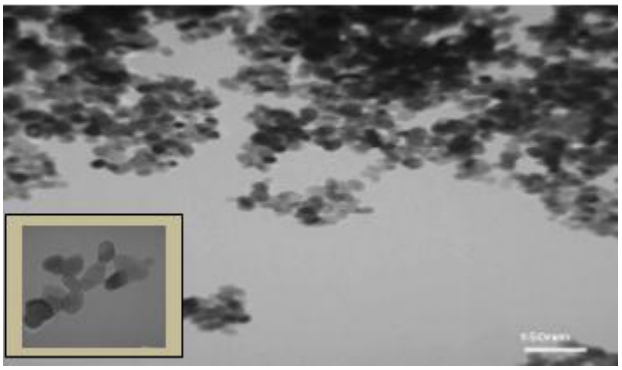

Figure 5: TEM image of the Cu:Ni nanostructure.

It is possible to study the absorption spectra of copper-nickel nano-particles (Cu:Ni) produced by laser ablation. It was discovered that at a wavelength of 200 nm, absorption reduces. Figure 6 shows how its absorption diminishes with increasing wavelengths in the visible and infrared regions, where it is around (3.5%).

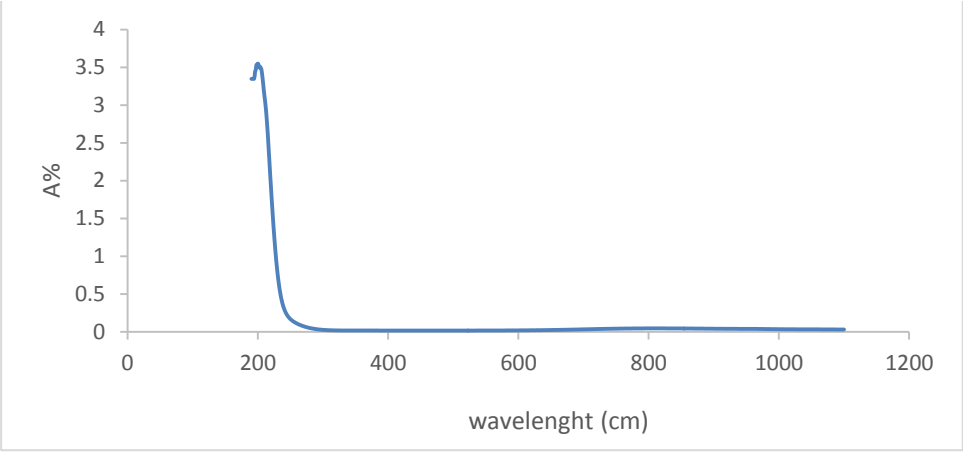

Figure 6: shows the optical absorbance spectrum of (Cu:Ni) nanoparticles.

Figure 7 displays the biological activity of four distinct types of positive and negative bacteria in distilled water when exposed to laser-produced copper nickel nano-particles. (Klebsiella spp., Staphylococcus aureus, Staphylococcus epidermidis, E. coli) Table 1 contains information on the biological impact, also known as inhibition with strong effects. [17].

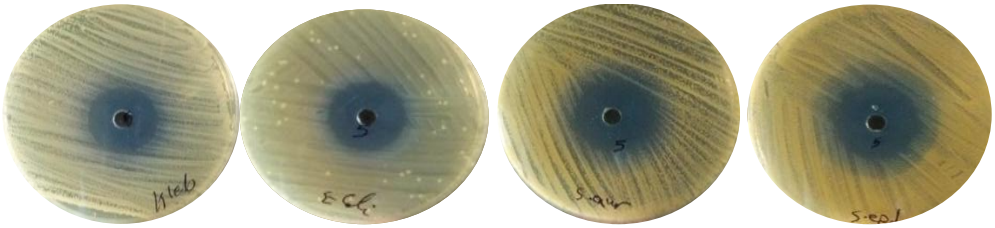

Figure 7: the adsorption of Cu:Ni nano-particles by bacteria

According to Table 1, the amount of sorption was the same for these four species of bacteria.

Table 1: The inhibition zone of Copper nickel Nano-particles by bacteria

Bacterial	Inhibition zone (mm)
S.aureus	26
S.epidermidis	25
E. coli	23
Klebsiella spp	24

Particles penetrate the bacterial cell wall and occupy specific locations in the DNA helical structure, thereby stopping metabolic processes and scattering enzymes, or the attraction of nanomaterial ions at high concentrations to the bacterial cell wall, thereby limiting oxidation and reduction and stopping respiratory processes, may initiate the inhibition process. To assess the quantity of absorbance and its interaction with this specific type of fungus, a nano-nickel oxide substance created by laser ablation of liquid was introduced to the fungi. It can absorb up to 22 mm of water.

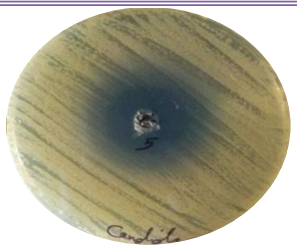

Figure 8: shows the amount of Cu:Ni nano-particles absorbed by fungi.

The topography of the surface was examined using an atomic force microscope. In Figure 10, a three-dimensional image of Cu:Ni nano-particles revealed a population of homogeneous particles with a stable surface. Cu:Ni nanoparticles with an average diameter of (426) nm are used in the liquid laser ablation procedure. The topography of the surface, such as the mean value of roughness and the root mean square.

Table (2) The average roughness, average diameter, and root mean square of the Cu:Ni Nanoparticle films

Sample	Average. diameter (nm)	Surface Roughness(nm)	Root Mean Square(nm)
Cu:Ni	426	34-35	50.42

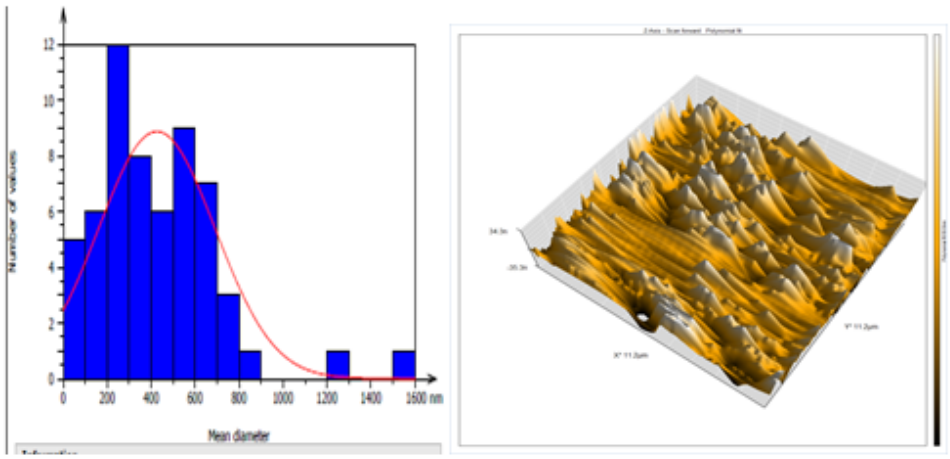

Figure9: AFM 3D surface topography and average grain size range distribution of Cu:Ni Np films.

Anticancer Activity

The antitumor activity of the manufactured nanoparticle is investigated using an MTT assay against breast cancer MCF7 cell lines throughout a dilation range of 0.5 to 2.5. Figure 11 demonstrates the relationship between the MTT assay and the relative cell viability of the cancer MCF-7 cell line.

According to the results of the chart, the colloidal nanoparticle has better anticancer activity at bigger dilations, i.e., at 0.5 dosages, and the anticancer activity declines as the dilations fall from 0.5 to 2.5. The breast cancer (MCF 7) cell viability%, i.e., the number

of live cancer cells, increases from 20% to 50%, indicating an inverse association between nanoparticle dilations and the number of living breast cancer cells. Furthermore, earlier research has demonstrated the dose-dependent anticancer efficacy of many kinds of nano-particles.

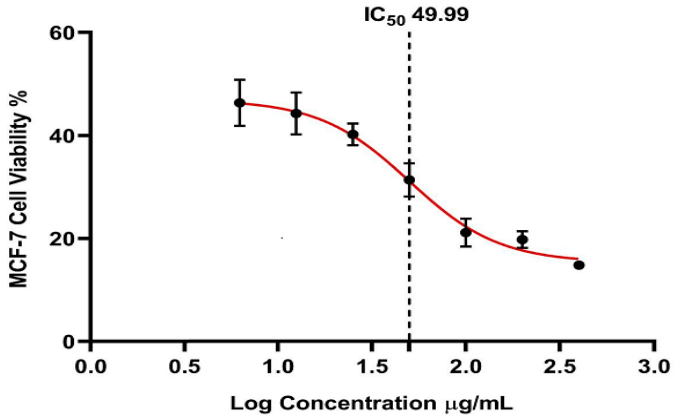

Figure (10): MTT assay chart gives the relative cell viability of breast cancer vs log concentration.

Conclusions

In this study, copper oxide and nickel oxide nanoparticles were investigated using the laser ablation technique. NiO and CuO nanoparticles in water were created by laser ablation and then examined using SEM, TEM, UV-vis absorption, AFM, and FTIR. SEM, TEM, UV-vis absorption, and AFM, FTIR was used to analyze NiO and CuO nanoparticles generated in water using the laser ablation approach. For most metal oxides, it is possible to create nano-particles in large quantities and of high economic quality. Furthermore, a new study indicates that laser ablation of nickel and copper metal in water can generate nickel oxide and copper oxide nano-particles extremely quickly.

The relationship between nickel and oxygen, copper and oxygen, is proven by FTIR spectra at (600-700) cm-1. may be observed in the UV-Vis absorption spectrum. The findings show that NiO and CuO nano-particles have a synergistic impact on bacteria's cell membranes and that Ni and Cu nano-particles may efficiently boost bacterial penetration and absorption, making them a good platform for biological applications. The findings revealed that copper-nickel nano-particles had a greater impact on (Bacterial and fungi).

References

[1] Akimoto K, Ishizuka S, Yanagita M, Nawa Y, Paul GK, Sakurai (2008) T. Sol. Energy 0:715.

[2] C. C. Trapalis, M. KokkOris, G. Perdikakis, G. Kordas, Study of antibacterial composite Cu/ SiO_2 thin coatings, J. Sol-Gel Sci Techn. 26 (2003) 1213–1218, https://doi.org/10.1023/A:1020720504942.

[3] S. Pal, Y. K. Tak, J. M. Song, Does the antibacterial activity of silver nanoparticles depend on the shape of the nanoparticle? A study of the gram-negative bacterium Escherichia coli, Appl. Environ. Microb. 73 (6) (2007) 1712–1720, https://doi.org/10.1128/AEM.02218-06.

[4] V. Sambhy, M.M. MacBride, B. Peterson, A. Sen, Silver bromide nanoparticle/ polymer composites: dual action tunable antimicrobial materials, J. Am. Chem. Soc. 128 (2006) 9798–9808, https://doi.org/10.1021/ja061442z.
[5] K. B. Holt, A. J. Bard, Interaction of silver (I) ions with the respiratory chain of Escherichia coli: an electrochemical and scanning electrochemical microscopy study of the antimicrobial mechanism of micromolar Ag+, Biochemistry 44 (13214–13223) (2005), https://doi.org/10.1021/bi0508542.
[6] M. Kawashita, S. Tsuneyama, F. Miyaji, T. Kokubo, H. Kozuka, K. Yamamoto, Antibacterial silver-containing silica glass prepared by sol-gel method, Biomaterials 21 (4) (2000) 393–398, https://doi.org/10.1016/S0142-9612(99) 00201-X.
[7] G. Faundez, M. Troncoso, P. Navarrete, G. Figueroa, Antimicrobial activity of copper surfaces against suspensions of salmonella enterica and campylobacter, BMC Microbial. 4 (2004) 19–25, https://doi.org/10.1186/ 1471-2180-4-19.
[8] Rosarin FS and Mirunalini S (2011) Nobel Metallic Nanoparticles with Novel Biomedical Properties *J. Bioanal. Biomed.* Vol. 3(4) 85-91.
[9] A. Garduno, J. C. Alonso, M Bizarro, R. Ortega, L. Rodrıguez-Fernandez, A. Ortiz (2010), "Optical and electrical properties of lithium doped nickel oxide films deposited by spray pyrolysis onto alumina substrates" Jour. of Crystal Growth, 312: 3276-3281.
[10] Hammad AH, Abdel-wahab MS, Vattamkandathil S, Ansari AR. Growth and Correlation of the Physical and Structural Properties of Hexagonal Nanocrystalline Nickel Oxide Thin Films with Film Thickness. Coatings (2019). 9(10), 615.
[11] Habubi NF, Ismail RA, Abd AN, Hamoudi WK. Improved photoresponse of porous silicon photodetectors by embedding CdSe nanoparticles. Indian J. Pure Appl. Phys, (2015); 53: 718.
[12] Jesuraj SA, Haris M, Immanuel P. Structural and Optical Properties of Pure Nio and Li-Doped Nickel Oxide Thin Films by Sol-Gel Spin Coating Method. Strain (2013). 10, 10-3.
[13] Sahar A. Aziz, Reem S. Ali, Ahmed. N. Abd, "Characterization Studies of Nickel Oxide Nanostructure films Prepared by Electrolysis Method for Photo Detectors Applications", Neuro Quantology.18, (2020). pp. 45-49.
[14] Abd AN, Habubi NF, Ismail RA. Preparation of colloidal cadmium selenide nanoparticles by pulsed laser ablation in methanol and toluene. Journal of Materials Science: Materials in Electronics (2014); 25(7): 3190-3194.
[15] M. A. Gondal, Tawfik A. Saleh, Q. A. Drmosh. "Synthesis of nickel Oxide nanoparticles using pulsed laser ablation in liquids and their optical characterization". Journal Applied surface science 258. (2012) p.p.6982-6986
[16] R. K. Swarnkar, S. C. Singh, R. Gopal, Paper presented at the 1st International Conference on Nanostructured Materials and Nanocomposites, Kottayam, India, 6–8 April 2009.
[17] Ali. A. fayyadh, Muneer. H. Jaduaa. "Green-synthesis of Ag_2O nanoparticles for antimicrobial assays". Journal of the Mechanical Behaviors of Materials 30(2021) p.p228-236.

Studies Comparison of People Gait Distinguish Using Biometric and Algorithms

Balkees Ahmed Mohammed, Ziad M. Abood*, Muhssen Salbookh Erhayief
Collage of Education, Mustansiyiah University, Iraq
dr.ziadmabood@uomustansiriyah.edu.iq

Abstract

Ear recognition is employed to protect the privacy and prevent unauthorized persons from entering the system. To distinguish people, many of the distinctive biometric features that characterize each person are relied on, so the biometric features are searched through which people can be distinguished with a high degree of accuracy. The aim of the study distinguishes people based on distinctive features in the ear using different computer algorithms. This paper presents a review of a number of the literature and a comparison of some different algorithms related to ear recognition.

Keywords: Personal identification, Biometric, Pattern recognition, Ear recognition.

المستخلص:

يستخدم التعرف على الأذن لحماية الخصوصية ومنع الأشخاص غير المصرح لهم من دخول النظام. ولتمييز الأشخاص، يتم الاعتماد على العديد من الصفات الحيوية المميزة التي يميز كل شخص، لذلك يتم البحث عن الصفات الحيوية التي يمكن من خلالها تمييز الأشخاص بدرجة عالية من الدقة. تهدف الدراسة إلى تمييز الأشخاص بناءً على السمات المميزة في الأذن باستخدام خوارزميات الحاسوب المختلفة. يقدم البحث الحالي مراجعة لعدد من الأدبيات ومقارنة بعض الخوارزميات المختلفة حول تمييز الأشخاص اعتمادا شكل الأذن.

الكلمات المفتاحية: التعريف الشخصي، المقاييس الحيوية، تمييز الأنماط، تمييز الأذن.

1. Introduction

Personal identification systems based on biometrics have witnessed a surge in popularity, owing to growing concerns about privacy and security in diverse applications. The human ear has been discovered to have enough discriminating qualities to allow it to be used as a robust biometric measure, even though the application of any biometric trait is problem dependent. Although locating an ear in a facial image is a difficult task, several existing techniques have shown promising results. The human ear has sparked a lot of attention in the biometric field in recent years because it has several advantages that are comparable to other biometrics like face, fingerprint, or gait. [1]

1.1 Biometric

Biometrics is a method that deals with identifying and verifying people built on physiological and behavioral characteristics. These characteristics or identifiers are singular and can be used for distinguishing one person from another [2].

As shown in Figure (2), biometric techniques can be categorized into two groups based on the attributes that are used: [3] Physiological Characteristics-Based Biometric Techniques: They cover all biometrics approaches that rely on simple computations on a specific portion of a person's body, such as the iris, face, or fingerprint. The most well-known and popular types are ear, hand, and DNA. These kinds are more trustworthy than those that are built on behavior.

Biometric Techniques Based on Behavioral Characteristics includes the following: This sort of approach extracts attributes based on a person's behavior or action; the most popular and successful types are voice, keystroke, and signature. [3]

1.2 Pattern recognition

Pattern recognition is the process of identifying patterns using machine learning techniques. It categorizes data using statistical data or knowledge derived from patterns and their representation. The computerized detection and analysis of patterns in signals are known as pattern recognition. It generally refers to the analysis, description, identification, and classification of objects or other relevant regularities in image processing [4, 5].

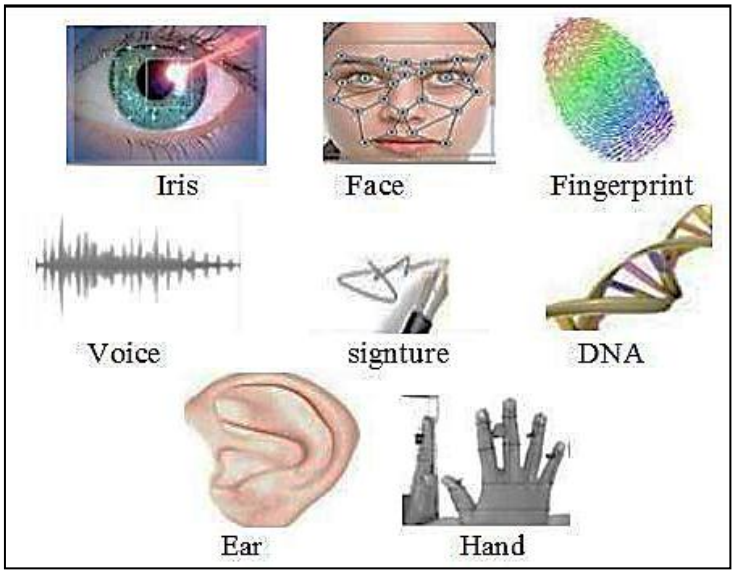

Figure 1: Biometric Technologies [3]

1.3 Ear recognition

Human ear identification is a relatively recent biometric technology that competes with other powerful biometric modalities such as fingerprint, face, and iris recognition. The ear is tiny, has uniform color dispersion, and does not require much user participation [6].

The biometric community is particularly interested in automatic identification detection of ear pictures. Automated personal identification using ear shape is becoming more accepted, mainly due to the ear pattern's ability to provide rich and consistent information that able is employed to distinguish and identify people. Ear images can be taken from a distance and invisibly, so it is catchy for security and surveillance applications, also in other related application areas. The human ear is unaffected by facial expressions and does not require near touching like fingerprints, unlike other biometric modalities. However, at the illumination, position, and partial occlusion are changed, the recognition performance drops dramatically, see figure (2) [7, 8].

Another prominent biometric is ear recognition, which is well alternative to other biometrics. Ear recognition algorithms use different sections of ear images to detect attributes and compare them to other ear images. Ear images able be caught passively, and the ear's stability allows for a more consistent biometric recognition method [9].

In general, registration and recognition are two base components in the permission identification system for people, where each step of them passes through three stages: firstly, is a pre-processing stage to improve the characteristics of the image for each person, followed by the second stage, which is to extract the region of interest ROI from each image, and finally, extraction the features that will be stored in the database. [10]

This paper reviews various methods to recognize the human ear with different algorithms. The remaining of the paper is set as follows section II provides a survey of literature on-ear recognition by using different algorithms. Section III compares different algorithms for ear recognition. Lastly, section IV gives the conclusion.

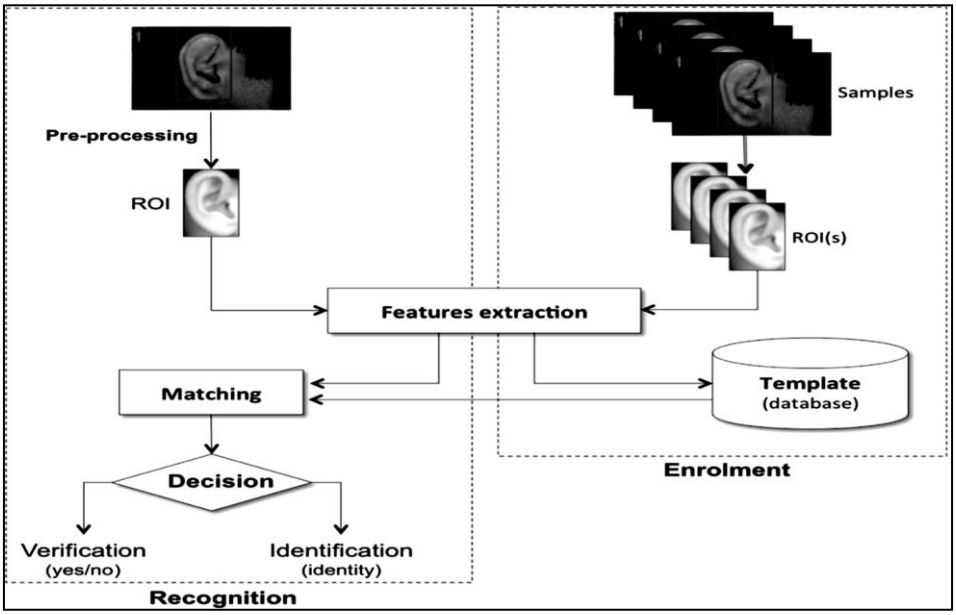

Figure 2: Human Ear recognition approach

2. Literatures Survey

Sinha et al. (2010), [1] the paper presented a system for person identification based on ear pictures. For ear image feature extraction, (PCA) was employed, and (MFFNN) for classification. The UND ear picture database, which has 85 images, was put to the test to see how reliable and accurate it was. When applied to the ear image field, which lacks many attributes that a facial image possesses, it obtained higher discrimination accuracy with the less computational effort (e.g. eyes, nose, mouth, etc.). However, he did not address the accuracy explicitly.

Wang et al. (2010), [2] employed the BP algorithm to classify identification. They chose three layers of the BP artificial neural network and 40 neurons in the middle. For ear, image distinguishes they utilized their own database 60, and they got a good trial result with a recognition rate of 91.8% when check six vectors were on a 4/5 scale. However, when seven vectors were input into the neural network, the results reached only a 66.7% recognition rate.

Tariq et al. (2011), [3] have proposed a new approach for an automated system for human ear identification. The method consists of three stages. In the first stage, preprocessing of the ear image is done for its contrast enhancement and size normalization. In the second stage, features are extracted through Haar wavelets followed by ear identification using fast normalized cross-correlation (Fast NCC) in the third stage. The proposed method is applied to the USTB ear image database and lIT Delhi ear image database. The proposed system achieves an average accuracy of 97.2% and 95.2% on these databases respectively. Results showed that the recognition rate on the USTB database is good. However, unrecognized one image from 60 images in USTB DB1, three Images

from 77 in USTB DB2, and not recognized six images from125 images in IIT Ear Database.

Asmaa et al. (2015), [4] developed a recognition technique based on the SIFT algorithm for identifying people until their ear images. The identification system is divided into 4 phases: pre-processing, detection of the ear image using edge detection, extraction of features from the ear picture, and classification using a minimum distance classifier. However, there are several obstacles to using the ear to identify persons, such as hair on the ear that obscures a great portion of them, Muslim women's headscarves that cover their hair and hence cover their ears, and the amount of illumination. They used three ear pictures for 125 persons from the IIT database. As a result, they achieved a rate of recognition is 95.2%. When they used the AMI database, which included Seven ear images for the 100 persons, they achieved an accuracy is 100%.

Khobragade et al. (2016), [5] the ear recognition system encountered problems due to improper image capture Blurred images do not give good results. Noise generated due to hair occlusion and improper lighting is also a problem. They proposed a simple and less time-consuming method for 20 ear feature extraction. As a result, they used MATLAB as a processing tool. They did image preprocessing to remove unwanted information of ear images, also performed steps like image segmentation and feature extraction to get the desired shape of the ear for ear recognition system purposes. They have applied the feature extraction process to 40 people. The method gives the best results for the ear images which are appropriate, properly captured, and has proper light. While The method gives poor results for the ear images which are not captured properly or have high light intensity. So, the method of feature extraction is failed to get output from pose variation, blurred and high light intensity images.

Rao et al. (2019), [6] proposed a methodology for ear localization and recognition which reduces the pipeline for a biometric recognition system. The proposed framework uses HOG with SVM for ear localization and CNN for ear recognition. HOG descriptors depend on image gradient orientations which describe the shape of an object. But it poses challenges such as illumination, contrast, rotation, scale, and pose variation. The problem of ear recognition is very similar to that of face recognition. It faces the problem of bad illumination, poses variation, and occlusion. Recognition models are generally unable to overcome problems such as local deformation, rotation, or translation. The (USTB) provides three databases for public use. The USTB III ear dataset contains side profile images of the face. The database contains images from 79 subjects, each image having a resolution of 768×576. Each subject has approximately 10 uncropped images (a total of 785 images). The work demonstrates 97.9% average recognition accuracy using CNN without any image preprocessing. The proposed method achieves the highest recognition rate of 97.9% on the USTB III dataset.

Alemran and Rahmatullah, (2019), [7] the study aimed to construct a passive identification system for hybrid ear biometric from a digital image database. The database was gathered from two classes of identifiers (right-left ear of the same individual). The difficulty of occlusion, variations in illumination, and real-time application in getting information from an integrated database system with improved accuracy are all challenges and concerns faced in the domain of personal identification employing ear detection and recognition. They used the USTB and IIT Delhi databases because they contain suitable images for testing. However, they did not mention accuracy as a percentage.

Sarangi et al. (2019), [8] suggested integrating two of the most used local feature descriptors to represent ear images, such as Gradient Directed Hierarchical Graph (PHOG) and Local Orientation Patterns (LDP). LDP effectively encodes local tissue information,

while PHOG reflects spatial shape information. They employed principal component analysis (PCA) to minimize dimensionality before normalization and fusion because feature sets had a lot of them. So, to create a single feature vector, two sets of heterogeneous conventional features are amalgamated. Lastly, they extracted nonlinear discriminant features using the Kernel Discriminant Analysis (KDA) approach for efficient identification using the nearest classifier (NN). Experiments with three standard datasets from IIT Delhi (I and II) and UND-E have achieved remarkable discrimination performance comparison with other methods. However, there isn't evident accuracy.

Priyadharshini et al. (2020), [9] devised a straightforward deep CNN architecture for detecting persons from ear pictures. Traditional computer vision systems rely on hand-crafted features, but CNNs immediately learn the features from the input image, resulting in improved performance. Hair, fabric, or jewelry can, nevertheless, obstruct vision. For ear recognition, they presented a six-layer deep CNN architecture. The simple DL architecture is built with the memory requirements of end applications in mind. They used a database IIT Delhi consisting of two groups, the first group IITD-I contain 125 different subjects, the second group IITD-II includes 100 various objects. All objects in the database are between 14 and 58 years old. They also used a database AMI that contains 700 images from 100 people between the ages of 19 and 65 years all images are 492×702 pixels in size. On the IITD-II ear dataset and the AMI ear dataset, the Deep CNN's potential performance is examined. They achieved a recognition rate of 97.36% for the IITD-II dataset under a controlled environment for the tanh activation function, but they observed that the sigmoid activation function suffers from overfitting, and 96.99% for the AMI dataset in uncontrolled environment.

Ganapathi et al. (2020), [10] proposed a new and effective system to describe and reveal the key points using geometric statistics to match and represent the same three-dimensional subjects. Identifying three-dimensional biometrics based on the ear can prove its effectiveness. However, the applications of biometrics, when they used to compare the same subjects such as the ear or face, fail. Experiments were carried out on the public database of the University of Notre Dame Collection-J2 (UND-J2). It contains 1,779 samples from 404 people. Experiments using the University of Notre Dame public database Collection J2 (UND-J2) yielded rank-1 and rank-2 recognition rates of 98.60 percent and 100 percent, respectively, with a 1.50 percent error rate. Because of the following factors, it is a reliable and general technique. 1) Conducted on a genuinely large model size from the UND-J2 database, which includes images of the ear with changes in position and scale, as well as images affected by occlusion. 2) They randomly selected the gallery image of the subject from the database, during the experiments, instead of selecting a good image of the subject.

Nikose et al. (2020), [11] applied a deep learning-based convolutional neural network (CNN) model to the USTB database. They used a Gaussian filter and Canny's edge detector to manipulate the image to increase the recognition rate. However, to obtain the information, they ran into hair, cloth, or earring clogged issues. USTB database is component of three groups: - USTB Database1 (60 subjects), USTB Database2 (77 subjects), and USTB Database3 (79 subjects). The results showed that the USTB database I and database II achieved an accuracy of 93.345% and 91.281%, respectively, because the accuracy was low in the second database due to the loss of important information such as the scar in the ear, the use of a sharp-edged detector. One of the reasons is the depletion of memory due to reducing the size of the image. At the ear images are taken in different directions, the algorithm used is unable to map the pictures from USTB Database2 to training and test images, which results in low accuracy. However, there was no distortion

in the orientation of the different images in database1 and database3. Which led to a relationship between training and testing images and thus have better accuracy.

The researcher (Chowdhury) et al. (2020), [12] devised a method based on a tunable filter bank. To determine the camera source for ear biometric images. To verify, they used the devised method in two sets of ear databases. The initial experiment used three databases: the IITD-I, AMI, and WPUT ear databases, each of which contained a distinct camera type. To identify the image source, they used a random forest classifier with an accuracy of 99.25 percent in this scenario. The accuracy of camera source identification was significantly decreased in the second experiment using four datasets IITD-I, AMI, WPUT, and AWE ear. The addition of the AWE ear database was the main reason for the decreased inaccuracy in the second experiment. Each database, except for AWE, utilizes the same camera model to get ear photographs. However, images in the AWE database are get from the web. AWE, for instance, employs a different camera model to obtain images. As a result, it's feasible that some AWE camera types are comparable to those in three other databases. As a result, photos from a different database were utilizing incorrectly same camera source.

3. Comparative Analysis of Algorithms

Table (1) show comparison between ear algorithms.

Table 1: Comparison between above algorithms

Ref	Year	Algorithm	Database	Accuracy %
1	2010	PCA and MFFNN	UND	-
2	2010	BP algorithm	their own database	91.8
3	2011	Fast NCC	USTB	97.2
			lIT Delhi	95.2
4	2015	SIFT algorithm	lIT Delhi	95.2
			AMI	100
5	2016	MATLAB	their own database	-
6	2019	CNN	USTB III	97.9
8	2020	deep CNN	IITD-II	97.36
			AMI	96.99
10	2020	geometric statistics	UND-J2	Rank-1, 98.60
				Rank-2, 100
11	2020	CNN	USTB I	93.345
			USTB II	91.281
12	2020	tunable filter bank	IITD-I, AMI, and WPUT	99.25

4. Conclusion

This document covers a variety of ear algorithm that use to recognize people within the period (2010-2020), this paper has presented different strategies in ear recognition some of them extracts features, and others focus on ear shapes and their own geometric by using different algorithms artificial intelligence. It has been demonstrated that ear biometrics can be used for identification and that they are a good biometric that is similar to face biometrics.

Acknowledgements
The authors would like to thank Mustansiriyah University (https://uomustansiriyah.edu.iq Baghdad- Iraq) for its support in this work.

References
[1] A. Kamboj, R. Rani, A. Nigam, and R. R. Jha, "CED-Net: context-aware ear detection network for unconstrained images", Pattern Anal. Appl., vol. 24, no. 2, pp. 779–800, 2021, doi: 10.1007/s10044-020-00914-4.
[2] S. Dargan and M. Kumar, "A Comprehensive Survey on the Biometric Recognition Systems based on Physiological and Behavioral Modalities", Expert Syst. Appl., p. 113114, 2019, doi: 10.1016/ j.eswa.2019.113114.
[3] R. A. Mustafa, H. S. Chyad, and D. N. George, "Human Ear Print Detection Algorithm", Int. J. Eng. Res. Adv. Technol., vol. 06, no. 08, pp. 90–104, 2020, doi: 10.31695/ijerat.2020.3644.
[4] Bishop, Christopher M. (2006). Pattern Recognition and Machine Learning. Springer.
[5] Milewski, Robert; Govindaraju, Venu (31 March 2008). "Binarization and cleanup of handwritten text from carbon copy medical form images". Pattern Recognition. 41 (4): 1308–1315. doi:10. 1016/ j.patcog.2007.08.018.
[6] L. Ghoualmi, A. Draa, and S. Chikhi, "An efficient feature selection scheme based on genetic algorithm for ear biometrics authentication," 12th Int. Symp. Program. Syst. ISPS 2015, pp. 234–238, 2015, doi: 10.1109/ISPS.2015.7244991.
[7] A. M. Alkababji and O. H. Mohammed, "Real time ear recognition using deep learning", Telkomnika (Telecommunication Comput. Electron. Control, vol. 19, no. 2, pp. 523–530, 2021, doi: 10.12928/ TELKOMNIKA.v19i2.18322.
[8] A. Benzaoui, A. Hadid, and A. Boukrouche, "Ear biometric recognition using local texture descriptors", J. Electron. Imaging, vol. 23, no. 5, p. 053008, 2014, doi: 10.1117/1. jei.23.5.053008.
[9] E. E. Hansley, "Identification of Individuals from Ears in Real World Conditions", ProQuest Diss. Theses, no. April, p. 56, 2018.
[10] Z. Youbi, L. Boubchir, and A. Boukrouche, "Human ear recognition based on local multi-scale LBP features with city-block distance", Multimed. Tools Appl., vol. 78, no. 11, pp. 14425–14441, 2019, doi: 10.1007/s11042-018-6768-9.
[1,] M. Alaraj, J. Hou, and T. Fukami, "A neural network based human identification framework using ear images", IEEE Reg. 10 Annu. Int. Conf. Proceedings/TENCON, pp. 1595–1600, 2010, doi: 10.1109/TENCON.2010.5686043.
[2] X. Q. Wang, H. Y. Xia, and Z. L. Wahg, "The research of ear identification based on improved algorithm of moment invariant", ICIC 2010 - 3rd Int. Conf. Inf. Comput., vol. 1, pp. 58–60, 2010, doi: 10.1109/ICIC.2010.21.
[3] A. Tariq, M. A. Anjum, and M. U. Akram, "Personal identification using computerized human ear recognition system", Proc. 2011 Int. Conf. Comput. Sci. Netw. Technol. ICCSNT 2011, vol. 1, pp. 50–54, 2011, doi: 10.1109/ICCSNT.2011.6181906.
[4] A. S. Anwar, K. K. A. Ghany, and H. Elmahdy, "Human ear recognition using SIFT features", Proc. 2015 IEEE World Conf. Complex Syst. WCCS 2015, 2016, doi: 10.1109/ICoCS.2015.7483254.
[5] S. Khobragade, D. D. Mor, and A. Chhabra, "A method of ear feature extraction for ear biometrics using MATLAB", 12th IEEE Int. Conf. Electron. Energy, Environ. Commun. Comput. Control (E3-C3), INDICON 2015, no.3, 2016, doi: 10.1109/INDICON. 2015.7443344.

[6] G. S. Rao, G. V. Kumari, and B. P. Rao, Network for Biomedical Applications, vol. 2, no. January. Springer Singapore, 2019.
[7] A. Alemran and B. Rahmatullah, "Novel Hybrid Ear Recognition Framework in Passive Human Identification", Int. J. Acad. Res. Bus. Soc. Sci., vol. 9, no. 14, pp. 63–70, 2019, doi: 10.6007/ijarbss/v9-i14/6505.
[8] P. P. Sarangi, B. S. P. Mishra, and S. Dehuri, "Fusion of PHOG and LDP local descriptors for kernel-based ear biometric recognition", Multimed. Tools Appl., vol. 78, no. 8, pp. 9595–9623, 2019, doi: 10.1007/s11042-018-6489-0.
[9] R. Ahila Priyadharshini, S. Arivazhagan, and M. Arun, "A deep learning approach for person identification using ear biometrics", Appl. Intell., vol. 51, no. 4, pp. 2161–2172, 2021, doi: 10.1007/s10489-020-01995-8.
[10] I. I. Ganapathi, S. S. Ali, and S. Prakash, "Geometric statistics-based descriptor for 3D ear recognition", Vis. Comput., vol. 36, no. 1, pp. 161–173, 2020, doi: 10.1007/s00371-018-1593-8.
[11] S. Nikose and H. K. Meena, "Ear-biometrics for human identification", Proc. - 2020 Adv. Comput. Commun. Technol. High Perform. Appl. ACCTHPA 2020, pp. 8–13, 2020, doi: 10.1109/ACCTHPA49271.2020.9213190.
[12] D. P. Chowdhury, S. Bakshi, P. K. Sa, and B. Majhi, "Wavelet energy feature based source camera identification for ear biometric images," Pattern Recognit. Lett., vol. 130, pp. 139-147, 2020, doi: 10.1016/j.patrec.2018.10.009.

Comparative study: To prepare nanoscale lithium oxide using different materials on the properties of the material and its effect on antifungals

Bahaa J. Alwan[1], Ahmed N. Abd[2], Neihaya H. Zaki[3]
[1,2]Physics Department/ Collage of Science/ Mustansiriyah University/ Iraq
[3]Biology Department/ Collage of Science/ Mustansiriyah University/ Iraq

Abstract:

The colloidal solutions of M1 and M2 nanoparticles were prepared through the biosynthesis method using a Hibiscus sabdariffa L plant extract. Through optical measurements in the range of UV and visible rays, we observe an increase in the energy gap of M1 (2.8 eV and 4 eV) and M2 (3 eV and 4 eV), which indicate the increase in the concentration of nanoparticles and the quantum size effect. X-ray diffraction (XRD) pattern presented that the structure of the Lithium oxide films is polycrystalline and formation with preferential orientation of M1 NPs in Li_2O (100) direction, M2 NPs in Li_2O (200) direction, with an average crystallite size of nanoparticles were 42.22 and 17.15, nm, respectively. Morphological properties were observed by Field Emission Scanning Electron Microscopy (FESEM) images for particle size and shape of Lithium oxide nanoparticles. These images obtained give us a piece of important information about the nanostructure for these thin films. The particle sizes of M1 NP are (39.27 nm) and M2 NPs is (262.28 nm with the shape of these nanoparticles had semispherical a cluster, and woven fibers and mud like particles, respectively shown by FESEM images. according to this study. As a result, biosynthesized LiO nanoparticles could be promising candidates for biomedical applications in the future.

Keywords: lithium oxide, XRD, SEM, TEM, antifungi.

الخلاصة:

تم تحضير المحاليل الغروية للجسيمات النانوية M1 وM2 من خلال طريقة التخليق الحيوي باستخدام مستخلص نبات Hibiscus sabdariffa L. من خلال القياسات الضوئية في نطاق الأشعة فوق البنفسجية والأشعة المرئية، نلاحظ زيادة في فجوة الطاقة من M1 (2.8 eV and 4 eV) وM2 (3 eV and 4 eV)، مما يشير إلى زيادة تركيز الجسيمات النانوية وتأثير حجم الكم. أظهر نمط حيود الأشعة السينية (XRD) أن بنية أغشية أكسيد الليثيوم متعددة البلورات وتتشكل بتوجيه تفضيلي لـ M1 NPs، Li_2O (100) في اتجاه M2 NPs في اتجاه 200 (Li_2O)، بمتوسط حجم بلوري للجسيمات النانوية كانت 42.22 و17.15 نانومتر على التوالي. تمت ملاحظة الخصائص المورفولوجية بواسطة صور المجهر الإلكتروني لمسح الانبعاث الميداني (FESEM) لحجم وشكل الجسيمات النانوية لأكسيد الليثيوم. تعطينا هذه الصور التي تم الحصول عليها معلومات مهمة حول البنية النانوية لهذه الأغشية الرقيقة. أحجام جزيئات M1 NP هي (39.27 نانومتر) و(262.28) M2 NPs نانومتر مع شكل هذه الجسيمات النانوية تحتوي على كتلة نصف كروية، والألياف المنسوجة وجزيئات تشبه الطين، على التوالي موضحة في صور FESEM. وفقًا لهذه الدراسة. نتيجة لذلك، يمكن أن تكون جسيمات LiO النانوية المُصنَّعة حيوياً مرشحة واعدة للتطبيقات الطبية الحيوية في المستقبل.

الكلمات المفتاحية: أكسيد الليثيوم، XRD، SEM، TEM، مضاد للفطريات.

1. Introduction

Nanotechnology field has become one of modern physics and chemistry. Depending on certain features including size, distribution, and shape, nanoparticles (NPs) exhibit new or improved properties. Nanotechnology has advanced significantly in recent years. Numerous methods have been established to synthesis nanoparticles with specific shape and size requirements. The number of new nanoparticle and nanomaterial applications is rapidly increasing [1]. Nanotechnology is the study of materials on the nanoscale (1-100 nm) for various fields of study [2, 3]. Materials having nano-scale structures that display considerably innovative and enhanced physical, chemical, and biological properties,

phenomena, and usefulness are the focus of this field. Nanoparticles, on the other hand, are so much smaller that their surface areas far exceed those of their macro counterparts. The size, shape, composition, crystallinity, and surface morphology of metal nanoparticles are the primary factors that are responsible for determining their intrinsic qualities. Nanoparticles, because of their small size, have different properties than the bulk of a similar material [4, 5]. These differences have made it possible for countless new biosensor and bio nanotechnology advances. In the field of medical, nanotechnology is utilized for the diagnosis of diseases and disorders, the delivery of therapeutic medications, and the development of innovative remedies. This is a particularly powerful technology with incredible potential for designing and developing a wide range of novel products, which may have medical applications in detection of disease, treatment, and prevention [6].

2. Materials and Instruments

2.1 Instruments

Several instruments have been used in this analysis, as shown in Table (1).

Table (1): The instrument used in the experiment.

Instrument	Manufacturer
Beaker 250ml	China
Test tubes 5-10 ml	China
Petri dish	China
Four filter paper (grad 1:11 µm)	China
Glass Slides	China
Syringe 5ml or Microliter	China
Hot plate and Stirrer	Gallen Kamp, England

2. 2 Materials Chemicals

The materials which used to prepare lithium oxide nanoparticles are shown in Table (2).

Table (2) The chemicals used in the experiment.

Chemicals	Origin
Distilled water	**Iraq**
96% Ethanol absolute	**Iraq**
Hibiscus sabdariffa L	**Africa**
Lithium	**BDH Chemicals Ltd Pool England**
Lithium nitrate	**BDH Chemicals Ltd Pool England**
Lithium chloride	**BDH Chemicals Ltd Pool England**

2.3 Preparation of Plant Extract

Hibiscus sabdariffa L plant was utilized in the synthesis; it was purchased in an Iraqi market and then identified at the Seed bank of the Iraqi Health Ministry. 2 grams of powder of the dried HS plant are put on (Hot Plate and Magnetic Stirrer) with 100ml of distilled water at 60°C for an hour and cooled at room temperature. Then, Filter paper was used to purify the solution by removing particles.

3. Biosynthesis of Lithium Oxide nanoparticles by different methods

3.1 Method 1 (M1 NPs): LiCl NPs synthesized by Lithium chloride

1M molar of Lithium chloride (LiCl with Molar mass= 84.78 g/mol) dissolved in 100 ml of distilled water and mixed in hot plate. The device (Hot Plate and Magnetic Stirrer) is set to 60^{o}C, and the mixture is left there for an hour. Then, heat the aqueous solution at 160°C for an hour while adding 100 ml of the plant extract solution. The solution becomes a

bright blood crimson after being left alone for a while. The steady shift in hue is evidence of the creation of M1 nanoparticles

3.2 Method 2 (M2 NPs): Li NPs synthesized by Lithium

1M molar of lithium (Li) with Molar mass= 6.941 g/ mol) dissolved in 100 ml of distilled water and mixed in hot plate. (Hot Plate and Magnetic Stirrer) is set to 60 ^{o}C and the mixture is left there for one hour. Then, heat the aqueous solution at 160°C for an hour while adding 100 ml of the plant extract solution. The solution gets red as time passes. The steady development of a new hue is indicative of the production of M2 nanoparticles.

4. Results and dissection

4.1 X-ray Diffraction (XRD) Analysis

The structural features of thin films can be investigated by the use of x-ray diffraction. Drop-casting the nanoparticle solution applied on a glass substrate heated to 70°C yields a thin layer with uniformly dispersed nanoparticles, which is used to construct the Lithium oxide nanostructure. Crystalline phase and crystal structure of biosynthesized films using Hibiscus sabdariffa L plant extract were analyzed using X-ray diffraction. The XRD spectra in Figure (1) show the polycrystalline structure, Hexagonal, and Cubic phases formed after the synthesis of M1 and M2 NS with LiCl and Li, respectively, in a solution containing Hibiscus sabdariffa L plant extract. The Bragg peak observed at 2θ=22.45° associated with (002) of cubic phase Li2O2 (JCPDS card n0-05-0640), and other peak at 2θ values of 30.85° associated with the (100) of cubic phase Li_2O, and other sharp peaks such as 2θ=34.277° and 35.6° associated with the (100) the cubic phase planes for Li_2O_2(JCPDS card-39-1221), and the sharp peak at {2θ = 41.2° Li_2O (101). peak at 2θ = 48.194° Li_2O_2 (004), other peak located at 2θ = 49.3° of Li2O (110), and peak at 2θ = 58.3° of Li_2O_2 (104), and peak at 2θ value of 60.65° of Li_2O (021), and the last peak at 2θ value of 69.85° of Li_2O_2(200)}, of hexagonal phase plans (JCPDS-005-0674), In the present analysis as seen in figure (1:a).

For M2, the Bragg peak at 2θ=22.2° is associated with the (001) plane of the cubic phase of the Li (JCPDS-05-0640), while another peaks at 2θ=32.55° are associated with the (220) the cubic phase plane of the Li (JCPDS-39-1221), and another peak at 2θ=40.6° is associated with the (200) plane of the cubic phase of the Li_2O (JCPDS-05-0640) (JCPDS-005-0674) as seen in figure (1:b).

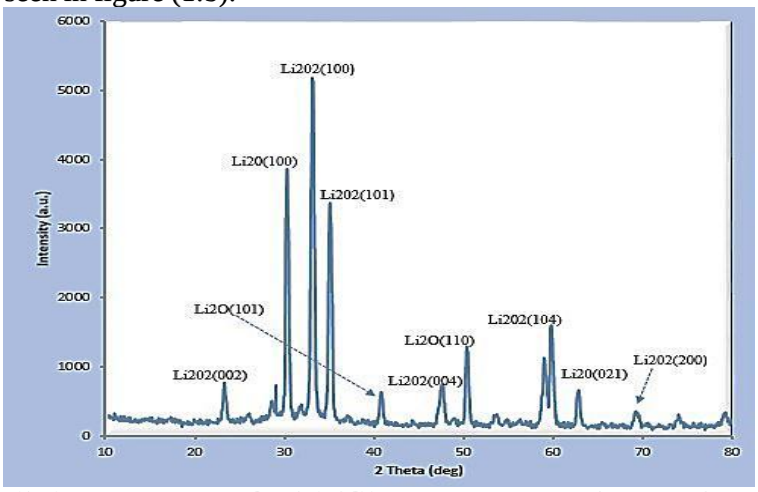

Figure (1:a) :XRD pattern of M1 (LiCl) nanostructure, which deposited on a glass.

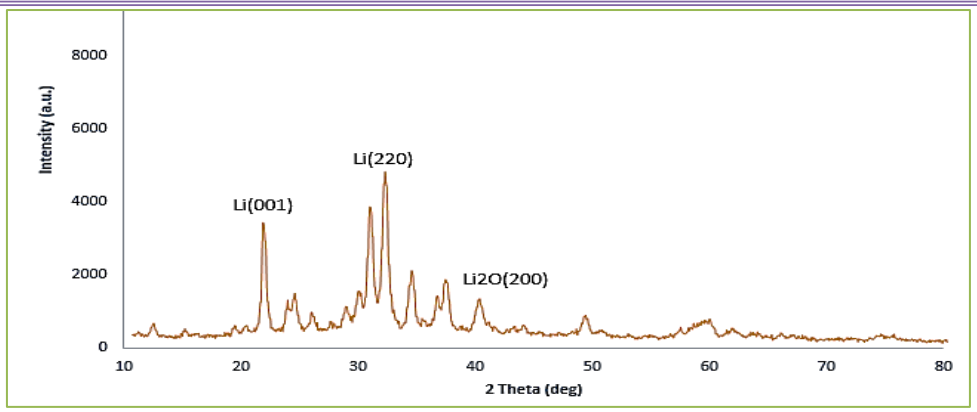

Figure (1:b) XRD pattern of M1 (Li) nanostructure, which deposited on a glass.

Miller indices (hkl) computed for each peak in LiCl and Li nanostructures using Bragg's equation (1.9) agree with the orientation of the JCPDS standard card of planes. Sharpening of XRD peaks in Table (4.2) demonstrates an increase in the crystalline quality of the particles in M1 and M2 NS. It demonstrates that experimental and reference data for inter-planar distance are in accord with one another. According to the X-ray spectrum and international standards, pure lithium particles and mono and dioxides in one compound are produced using the green synthesis method and the drop-casting method at temperatures not exceeding 70 ° C; in addition, the plant extract serves as oxygen reduction from the salts of the substance, and the absence of any organic compounds refers to the plant. According to the Figure, lithium nitrate is a better candidate for producing lithium oxides than either pure lithium or lithium chlorides, but it still has to be calcined at high temperatures to stabilize the material. By using Debye-formula Scherrer's (7, 8), we were able to determine that the typical crystalline size is around 49.69 nm. Dislocation density (δ) and microstrain (η) were also determined using reference (9-10).

Table (3) Structural parameters of M1 and M2 nanostructure.

Sample	2 Theta (deg)	FWHM (deg)	D (nm)	strain 10^{-4}	δ line/m^2 10^{14}
M1	23.20	0.246	32.79	10.56	9.290
	28.52	0.295	27.62	12.54	13.10
	30.15	0.196	41.58	8.331	5.78
	31.73	0.393	20.87	16.59	22.94
	33.12	0.442	18.62	18.60	28.83
	35.24	0.147	56.18	6.1666	3.167
	40.69	0.344	24.48	14.15	16.68
	47.62	0.344	25.09	13.80	15.87
	50.40	0.393	22.20	15.60	20.27
	53.59	0.492	18.01	19.23	30.82
	58.98	0.196	46.18	7.501	4.687
	59.73	0.295	30.90	11.21	10.46
M2	62.69	0.196	47.08	7.358	4.510
	69.21	0.688	13.96	24.81	51.27
	21.51	0.196	40.86	8.478	5.987
	32.07	0.393	20.89	16.58	22.90
	43.81	0.590	14.43	24.00	47.99

4.2 Field Emission-Scanning Electron Microscopy (FESEM)

FESEM, utilized in order for investigate a morphological characteristics of nanoparticles (at 1.00kx and 60.00kx magnifications). Figure (2a and b) displays (FESEM) images of bio-synthesized M1 and M2 thin films that were formed on a glass substrate by the use of a drop-casting process. The 39.27 nm M1 nanostructure and the 262.28 nm M2 nanostructure, Not only are M1 NPs semi-spherical, but M2 NPs are clustered, Because of the organic particles left behind from the plant extract, the size of the nanoparticles is significantly different from the particles generated with pure lithium.

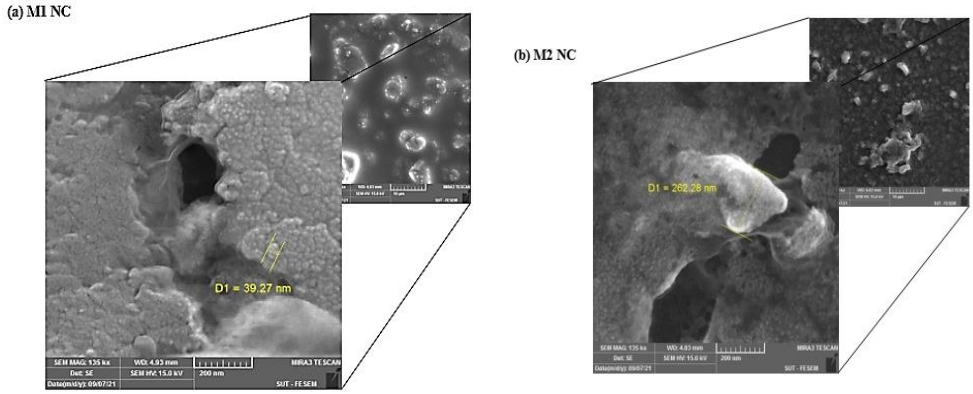

Figure (2): FESEM of (a) M1 and (b) M2 film deposited on a glass (scale bar = 10 µm, 200nm).

4.3 Transmission electron microscope (TEM)

The TEM images of lithium oxide nanocomposite caused by bio-synthesized techniques utilizing various salts of lithium solvents in distill water are exhibited in the figures (3). The micrographs demonstrate the development of well-defined spherical nanoparticles, and the TEM images demonstrate that the diameters of the nanoparticles vary depending on the preparation technique (M1 and M2), although all of them are less than 20 nm in size.

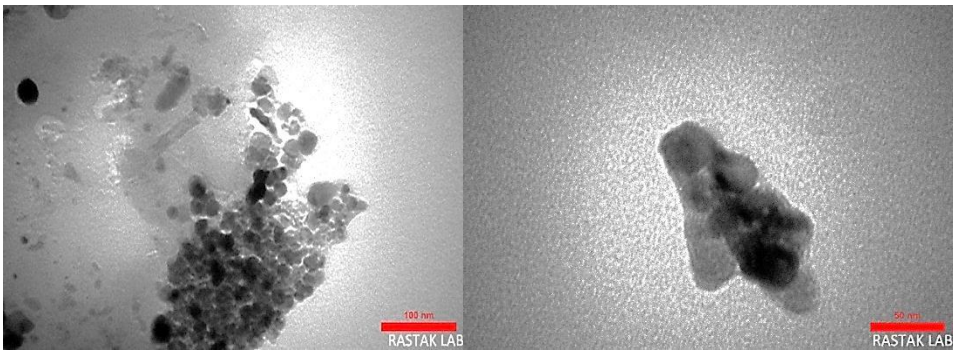

Figure (3) TEM images of (a) M1 and (b) M2

5. Antifungal activity of M1and M2 NPs

Through the use of the agar well diffusion technique, the antifungal properties of the biosynthesized M1, M2, and M3 nanoparticles were investigated. This technique was used to combat a variety of pathogenic fungus, such as Candida albicans and Aspergillus species, among others. Antifungal activity was determined by testing various molar concentrations of produced M1, M2, and M3 NPs, including 0%, 25%, 50%, and 75% M. The findings demonstrated that the materials exhibited antifungal activity that was

proportional to the concentration of the nanoparticles used, At a 50% and 75% concentration of the nanoparticles, the greatest zone of inhibition (ZOI) plate images were found in the progression of the fungus. It's possible that this is because of the differences in the chemical structure and ingredients that make up the antifungal cell wall. Antifungal action of M1and M2 nanoparticles may be attributed to the inhibition of enzymes and toxins employed by fungal pathogens for pathogenesis, as has been shown (Figure 4) and Table (4). This provides further evidence that the biosynthesized M1and M2 nanoparticles are capable of functioning as antifungal agents.

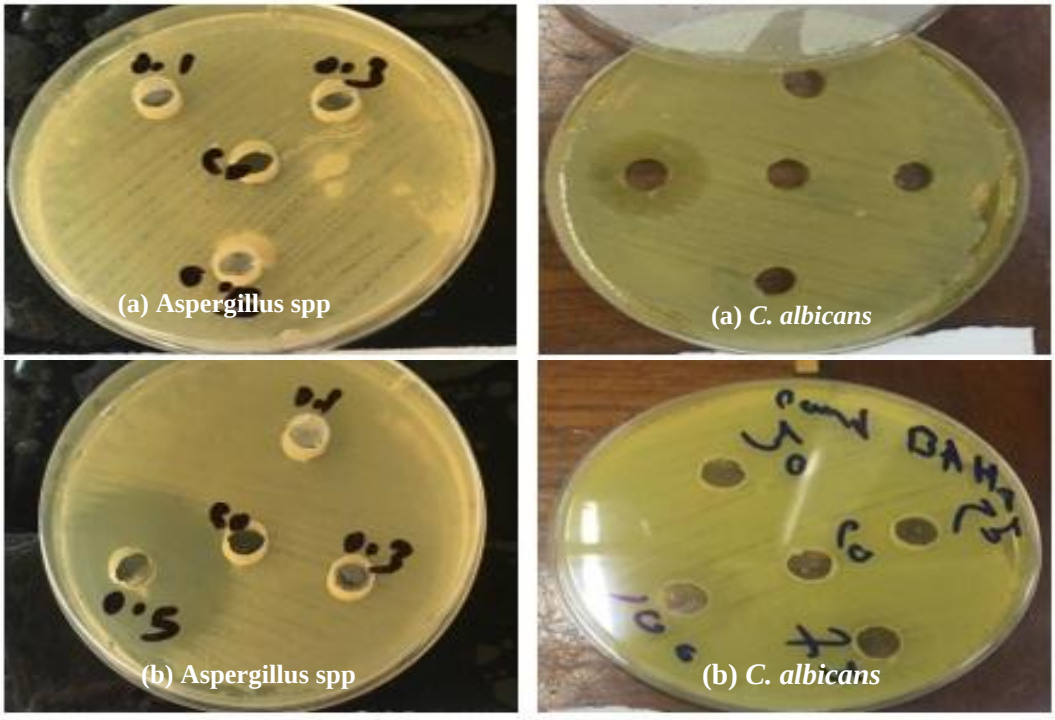

Figure (4) Antifungal activity of NPs synthesized from (a) M1 NPs and (b) M2 NPs NPs against C. Albicans and Aspergillus spp at (0%,25%, 50%, 75% M).

Table (4) Zone of inhibitions (mm) of biosynthesized M1 and, M3 NPs against C. Albicans and Aspergillus spp at (0%, 25%, 50%, 75% M).

Type of material	Aspergillus spp				C. albicans			
	Molar concentrations				Molar concentrations			
	0%	25%	50%	75%	0%	25%	50%	75%
(a) M1 NPs (Sample LiCl)	0	o. s	o. s	o. s	0	o. s	o. s	7mm
(b) M2 NPs (Sample Li)	0	o. s	o. s	40mm	0	o. s	o. s	o. s

5. Conclusions

The results indicated that lithium oxide can be prepared by the method of plant synthesis using lithium salts represented by lithium chloride or pure lithium, but the properties of the prepared lithium oxides, whether they are mono, binary or triple, depend on the materials that enter the preparation, so the effect on the fungi used was different other than the preparation method and the concentration of those materials.

Reference:

[1] Barnali Ashe, "A Detail investigation to observe the effect of zinc oxide and silver nanoparticles in biological system", M.SC. thesis, Department of Biotechnology & Medical Engineering National Institute of Technology, (2011).
[2] Kelsall, Robert, Ian W. Hamley, and Mark Geoghegan, eds. Nanoscale science and technology. John Wiley & Sons, (2005).
[3] J. Prikulis, F. Svedberg and M. Kall," Nano Letters", 4, 115-118 (2004).
[4] Szymańska-Chargot, M., A. Gruszecka, A. Smolira, J. Cytawa, and L. Michalak. "Mass-spectrometric investigations of the synthesis of silver nanoparticles via electrolysis". Vacuum 82, no. 10:1088-1093 (2008).
[5] H. Zhang, U. Siegert, R. Liu, and W.Cai, "Nanoscale Res. Lett"; 4, 705-708 (2009).
[6] Ashaq Hussain Shan, "Investigations of optical, structural, antibacterial and photo catalytic properties of doped ZnO nanostructures", PhD thesis, B. S. Abdur Rahman University, (2014).
[7] Sze, Simon M., and Kwok K. Ng. Physics of semiconductor devices. John Wiley & sons, 2nd Ed. (1981).
[8] Sze, Simon M., and Kwok K. Ng. Physics of semiconductor devices. John Wiley & sons, 3rd Ed. (2007).
[9] Justin T. Seil, Thomas J Webster "Antimicrobial applications of nanotechnology: methods and literature" School of Engineering, Brown University, publisher and licensee Dove Medical Press Ltd, International Journal of Nanomedicine ;7, 2767–2781 (2012).
[10] Thangavelu, Raja Muthuramalingam, Dharanivasan Gunasekaran, Michael Immanuel Jesse, Mohammed Riyaz SU, Deepan Sundarajan.

Synthesis of Nickel Oxide Nano-Particles for Biological Activities

Saba J. Hasan
Department of Physics, College of Education, Mustansiriyah University, Iraq
Email: sabajameel66@gmail.com

Abstract:
This work describes the manufacture of nickel oxide nano-particles (NiO NPs) utilizing nickel nitrate and extract from pomegranate peels. In an (XRD) examination, a face-centered cubic phase was observed. By using SEM, the surface morphology was verified. The existence of Ni-O bonds in NiO NPs was established by (FT-IR) spectra. A band gap of 3.8 eV was employed to analyze the optical characteristics using UV-Visb spectral data. The anti-bacterial efficacy of the produced NiO nanomaterial against several gram positive and gram negative bacterial pathogens and fungi was examined. The produced NiO nano-particles performed better at inhibiting gram positive pathogens than gram negative pathogens and at inhibiting fungal growth.
Keywords: NiO, Nano-particles, UV–Vis absorption. Pomegranate peels extract, Bioapplications.

الخلاصة:
يصف هذا العمل تصنيع جزيئات أكسيد النيكل النانوية (NiO NPs) باستخدام نترات النيكل والمستخلص من قشور الرمان. في فحص (XRD)، لوحظ وجود مرحلة مكعبة محورها الوجه. باستخدام SEM، تم التحقق من مورفولوجيا السطح. تم تأسيس وجود روابط Ni-O في NiO NPs بواسطة أطياف (FT-IR). تم استخدام فجوة نطاق مقدارها 3.8 فولت لتحليل الخصائص الضوئية باستخدام البيانات الطيفية للأشعة فوق البنفسجية - Visb. تم فحص الفعالية المضادة للبكتيريا لمادة NiO النانوية المنتجة ضد العديد من مسببات الأمراض الجرثومية والفطريات الموجبة والسالبة الجرام. كان أداء جزيئات النانو النانوية المنتجة أفضل في تثبيط مسببات الأمراض إيجابية الجرام مقارنة بمسببات الأمراض سالبة الجرام وفي تثبيط نمو الفطريات.
الكلمات المفتاحية: NiO، جزيئات النانو، امتصاص UV-Vis، خلاصة قشور الرمان، التطبيقات الحيوية.

1-Introduction

Researchers' interest in nano-materials sparked by their effect of quantum size, which display special magnetic, optical, electrical, and catalytic capabilities [1, 2]. Food, agriculture, cosmetics, medication transport, biomedicine, cancer theranostics, biological, and pharmaceutical applications have all profited from the usage of nano-particles (NPs) [3–8]. NPs have also played a significant role in the development of several economic sectors. A p-type semiconductor with a large band gap energy of between 3.6 and 4 eV is nickel oxide (NiO). The synthesis of NiO NPs has been carried out using a variety of techniques, including sol-gel chemistry, electro deposition, hydrothermal synthesis, solvothermal approach, and co-precipitation [9–13]. Physical synthesis demands a lot of energy, whereas chemical synthesis frequently results in toxic compounds that are bad for the environment and generate non-biodegradable goods [14, 15]. To address these issues, scientists have devised a more dependable strategy that is also greener and more environmentally friendly [16]. Green synthesis using plant extracts is becoming more popular because they have a high phytochemical profile (alkaloids, flavonoids, and phenolic) that are thought to be effective stabilizers [17-19]. Plant extract has the potential to affect the size and form of NPs as well as function as a potent capping and lowering agent [20, 21]. As a result, scientists have focused on the manufacture of metallic nano-particles by the use of plants. NiO NPs have been successfully generated employing pomegranate peel extract as an efficient reducing and stabilizing agent, which is important given the significance of green nanochemistry. Numerous medical conditions can be

treated with pomegranate peel, including leucorrhea, gonorrhea, rheumatism, arthritis, cardiovascular disease, and liver illness. Without the use of any surfactants or organic/ inorganic solvents, the present work is the first to describe biogenic NiO NPs from pomegranate peel. The XRD, SEM, UV, and FTIR were used to characterize the produced NiO NPs. Additionally, several biological functions including anti-bacterial and antifungal.

2. Experimental part

Pomegranate peels weighing around 25 g were carefully cleaned and cut into little pieces. The peels were then submerged in deionized water for a further 30 minutes while the solution was continuously stirred at 60°C. Whatmann No. 1 filter paper was then used to filter the extract as shown in Figure1. The resultant extract was utilized to make pomegranate peel extract, which serves as a reducing and capping agent in the production of nanomaterial.

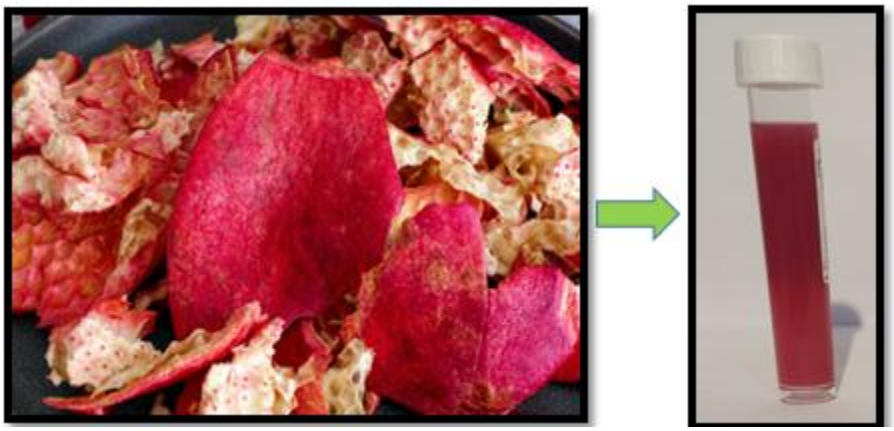

Figure1: pomegranate peel extract.

3. Preparation of NiO Nps

Nickel nitrate and the pomegranate peels extract of used as precursors to synthesize (NiO NPs) by green synthesis method. About 1.8g of Nickel nitrate in 100 ml under constant and continuous stirring for 1 h at 60 °C. 5 ml of the plant extract added to the aqueous solution of Nickel nitrate under constant and continuous stirring for 1 h in order to attain homogenous solution of NiO with concentration 0.1 M as in Figure2. Where the beaker on the left a nickel nitrate solution and in middle is the beginning of reaction of $(NO_3)_2$ solution with the extract of pomegranate peels, while the beaker on the right is the final homogenous solution of NiO nanoparticles**.**

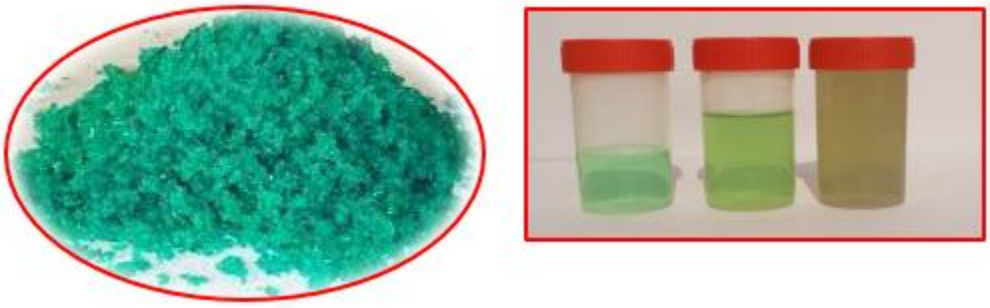

Figure 2: Ni $(NO_3)_2$ powder and NiO NPs colloidal

4. Application

The anti-bacterial activity of NiO NPs was assessed using the agar well diffusion technique on Muller-Hinton agar against two pathogenic bacterial strains (gram positive and gram negative) in line with the Clinical and Laboratory Standards Institute's. recommendations [22]. The medium plates were streaked with bacteria 2-3 times, rotating the plate at an angle of 60° for each streak, to ensure that the inoculums were distributed evenly. Then, 100 ml of each culture was swabbed onto the agar plates using a sterile L-shaped glass rod. Each petri plate has six millimeter (six mm) wells that were created with a sterile cork-borer. NiO NPs (1 g/ml for both G+ and G microbes) were added to petri plates with the bacteria, and they were then incubated for 1 day at 37 °C as in Figure 3.

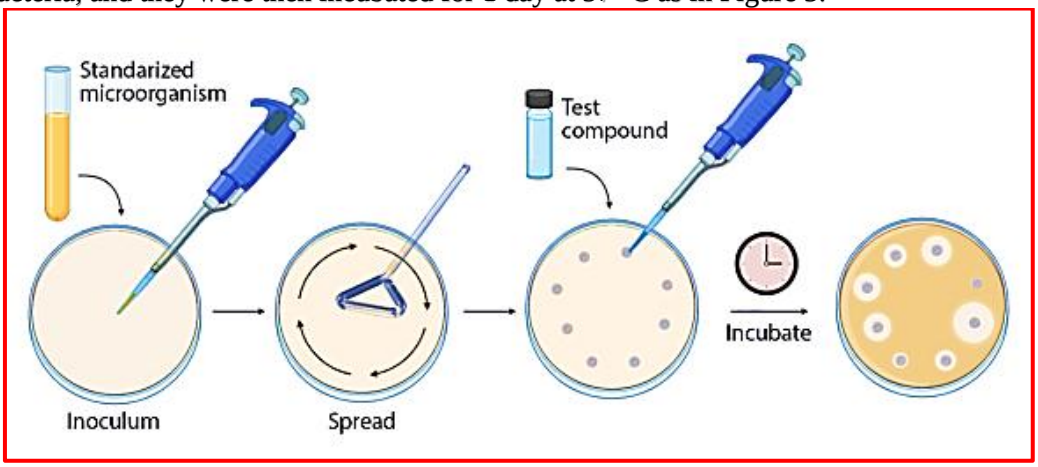

Figure 3: The agar disk diffusion method.

Figure 4 show XRD diffraction pattern of NiO that prepared by green synthises method and deposited on glass substrate by drop casting method (Three drops each equaling 100 ml). XRD pattern used to analyze the structural information and crystallinity. The NiO nanostructure's X-ray diffraction pattern is seen in Figure 4, there are four distinct Bragg peaks with maxima at 2θ = 37.14, 43.35, 62.89, and 75.49. According to card (JCP2 47-1049), the detected diffraction peaks that correspond to the (1 1 1), (2 0 0), (2 2 0), and (3 1 1) planes are well ascribed to the cubic structure of NiO. [23].

The morphology of NiO Nano-particles created using pomegranate peel extract and deposited on glass substrate using the drop casting process shown in Figure 5. SEM pictures show that the created nano-particles have various forms, aggregate as shells, and take on a relatively spherical appearance. Due to protein aggregation, NPs had average diameters between 50 and 150 nm, and some of the particles may be several micrometers in size. Phytochemicals that act as capping agents for the particles are responsible for the formation of the heterogeneous morphological characteristics [24].

The UV-Vis spectra of NiO-NPs shown in Figure 6. A good method for figuring out the energy structures and optical characteristics of nano-particles is absorption spectroscopy. It was believed that the creation of NiO-NPs was likely the source of the strong band at 380 nm. The movement of absorption bands towards short wavelength may be caused by a decrease in particle size in the blue shift, or UV area, when absorption rates rise [25].

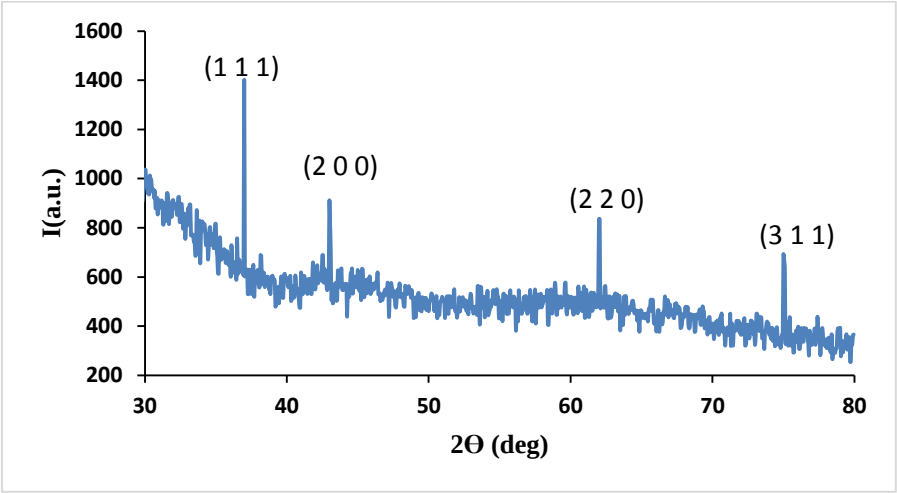

Figure 4: XRD pattern of NiO nanostructure

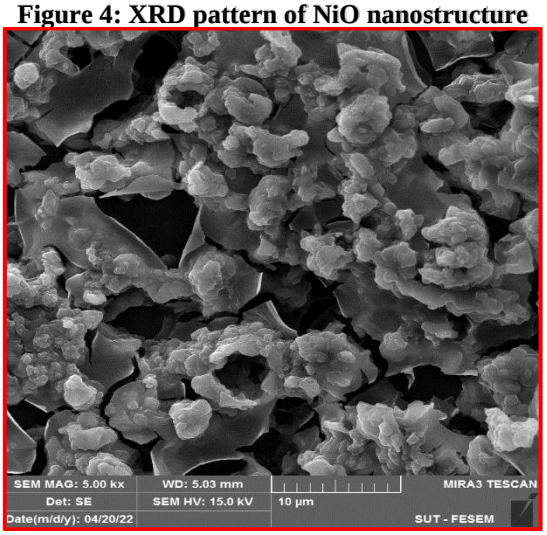

Figure 5: morphology of NiO nanostructure.

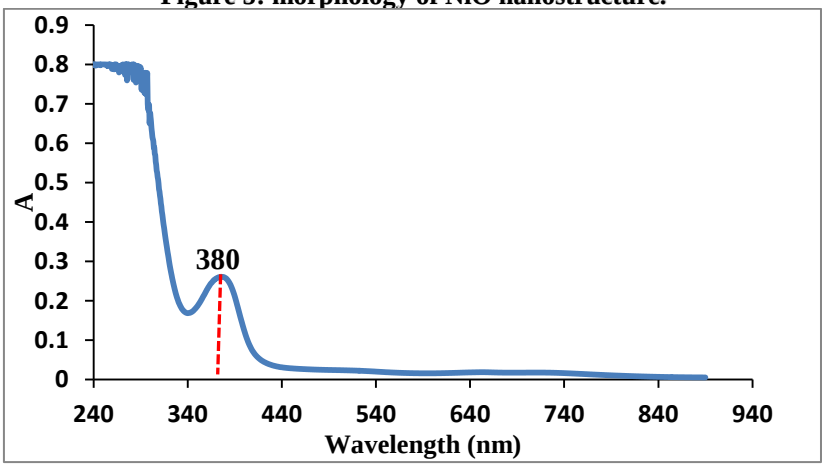

Figure 6. (a) Absorption spectra of NiO NPs.

Tauc equation's results were used to calculate the E_g of the NiO NPs [26–28]

Extrapolating the straight portion of the graph between $(\alpha hv)^2$ and hv yields (hv) = 0.

$$\alpha hv = \alpha_0 (hv - Eg)^n \ldots\ldots (1)$$

The results of the E_g calculation indicate that the band gap energy of NiO NPs is between 3.2 and 3.8 electron volts, as shown in Figure 6b. The spectra of nano-scale semi-conductors exhibit a blue shift as a result of the quantum confinement effects [26]. An rise in the band gap value and the blue shift phenomena point to a quantum confinement effect. This suggests that the band gap value increased as particle size decreased [26–28].

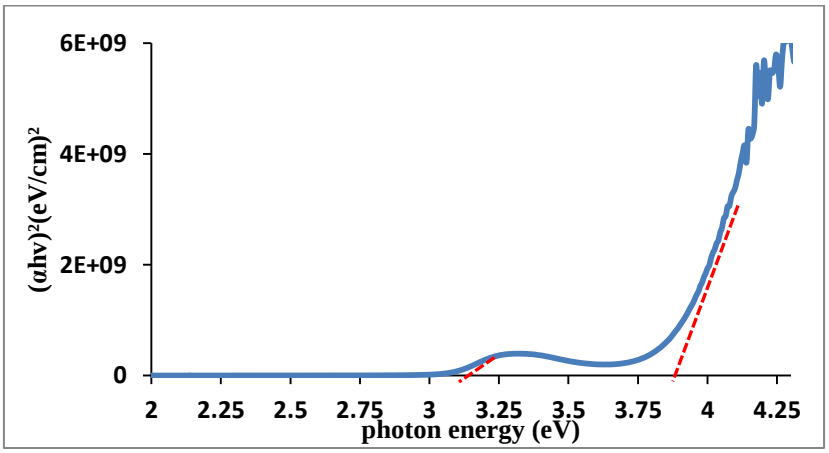

Fig.6b: displays a graph of $(\alpha hv)^2$ vs photon energy (hv).

The absorption peaks and their locations in FT-IR spectra are connected to a material's chemical composition, crystallinity, and morphology, and the absorption peaks below 1000 cm1 are regarded to be essential for evaluating whether Ni-O bonds are present in NiO NPs [29]. According to Figure 7, where the broadness of the absorption band reveals the nanocrystalline structure of the NiO, the vibration range (600-700) cm^{-1} assigned to Ni-O. The band at 1639 cm^{-1} seen because of water bending due to OH. This picture demonstrates that the broad absorption band at 3340 cm^{-1} is caused by band O-H stretching vibrations [30, 31].

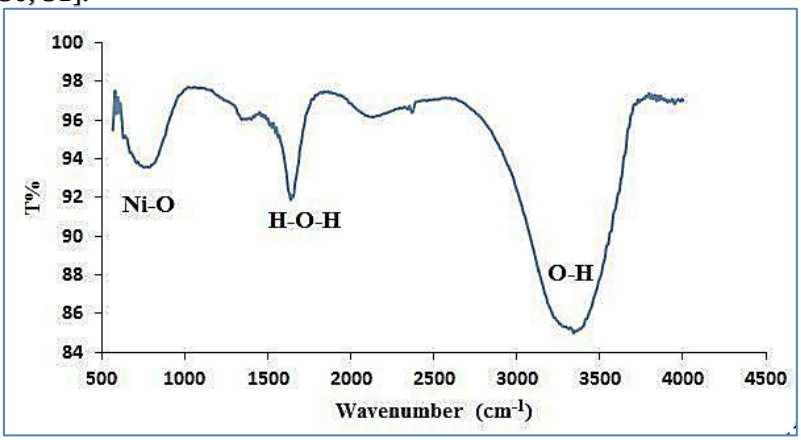

Figure 7: FTIR spectra of NiO NPs

Pomegranate peel extract was used to test the synthetic NiO NPs' anti-bacterial and antifungal efficacy against gram positive and gram negative bacterial pathogens as well as fungus growth. The several zones of inhibition are depicted in Figure 8.

Figure 8: Size of the zone of inhibition

The assessed bacterial strains were Staphylococcus aureus (19 mm), Escherichia coli (16 mm), Klebsiella (16 mm), and candida (15 mm). It is clear from the Figure 9 that the NiO NPs generated by the green method had outstanding anti-bacterial activity against these bacterial strains. However, compared to gram negative bacterial strains, Staphylococcus aureus bacteria had more activity. Staphylococcus aureus has just one cytoplasmic membrane and a thick wall made of several layers of peptidoglycan, which renders it more susceptible to harm [32]. This difference may be explained by these factors. Particle size has a substantial impact on anti-bacterial activity, and most studies have indicated that anti-bacterial activity rises as particle size decreases [33]. Due to their tiny size, green produced NiO nano-particles have a tendency to electrostatically cling to cell membranes [34] and trigger an oxidative stress response that damages bacterial cell membranes by releasing free radicals (ROS).

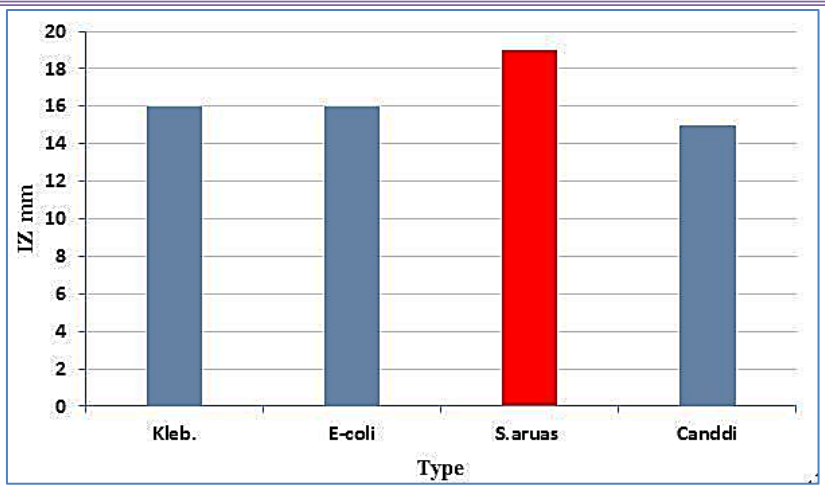

Figure 9: inhibition zone values of green synthesized NiO NPs

The amount of ROS produced is influenced by both the electrical makeup of metal - oxides and the redox potentials of the processes that produce it. The significant anti-bacterial activity of these nano-particles may be related to their unique chemical composition, particle size, tendency to release metal ions, and shape these elements result in the penetration and oxidation of cell components and the generation of secondary products (ROS), which harm cells. It is unclear exactly how metal oxide nano-particles are hazardous to bacteria. According to Basak et al., the anti-bacterial activity of the produced NiO nano-particle may be controlled by the electrostatic interaction between positively charged nickel ions and negatively charged bacterial cell membranes. NiO nano-particles that release nickel ions (Ni^{2+}) through the cell wall damage DNA, proteins, and mitochondria in addition to interfering with electron transport, which leads to cell death. NiO NPs diffuse and accumulate inside cell membranes, changing membrane permeability and causing protein leakage [35, 36].

Conclusion

Pomegranate peel extract has been produced as the fuel for a green-mediated synthesis of NiO NPs. The production of NiO NPs with a high purity phase and crystallinity was verified by XRD and FT IR. Our findings show that the green syntheses approach is effective for creating nano-particles and that it may be regarded as a safe, environmentally friendly method. Additionally, it offers a large quantity of nano-particles that may be applied in a variety of environmental and medicinal applications.

References

[1] J. Iqbal, B.A. Abbasi, R. Ahmad, T. Mahmood, B. Ali, A.T. Khalil, A. Munir, Nanomedicines for developing cancer nanotherapeutics: from benchtop to bedside and beyond, App. Microbiol. Biotechnol, Vol.102, pp. 9449-9470, 2018.
[2] Iqbal J, Abbasi BA, Mahmood T, Kanwal S, Ali B, Khalil AT, Shah SA "Plant-derived anticancer agents: a green anticancer approach. Asian Pac J Trop Biomed Vol.7, pp. 1129–1150, 2017.
[3] Tung-Yuan Yung, Li-Ying Huang, Tzu-Yi Chan, Kuan-Syun Wang, Ting-Yu Liu, Po-Tuan Chen, Chi-Yang Chao and Ling-Kang Liu."Synthesis and characterizations of Ni-NiO nanoparticles on PDDA-modified graphene for oxygen reduction reaction", Nanoscale Research Letters, Vol.9, pp. 444, 2014.

[4] Nurul Nadia Mohd Zorkiplia, Noor Haida Mohd Kausb, Ahmad Azmin Mohamad, "Synthesis of NiO Nanoparticles through Sol-gel Method", Procedia Chemistry, Vol.19, pp.626-631, 2016.
[5] Sone B T, Fuku X Gand Maaza M, "Physical&electrochemical properties of green synthesized bunsenite NiO nanoparticles viaCallistemon viminalis' extracts", Int. J. Electrochem. Sci. Vol.11, pp. 8204-8220,2016.
[6] Pandian CJ, Palanivel R. and Dhananasekaran S." Green synthesis of nickel nanoparticles using Ocimum sanctum and their application in dye and pollutant adsorption Chinese". J. Chem. Eng. Volume 23, pp. 1307-1315, 2015.
[7] S. Sudhasreea, A. Shakila Banua, P. Brindhab and Gino A. Kurian "Synthesis of nickel nanoparticles by chemical and green route and their comparison in respect to biological effect and toxicity". Toxicological & Environmental Chemistry, Vol. 96, pp.743-754,2014.
[8] B. Sasi, K. G. Gopchandran and P. K. Manoj, Studies on nanocrystalline nickel oxide thin films for potential applications, Mater. Today Proceedings, Vol. 4, pp.4123–4129, 2017.
[9] M. K. Lee and Y. T. Lai, "Characterization of transparent conducting p-type nickel oxide films grown by liquid phase deposition on glass", J. Phys. D: Appl. Phys., vol. 46, no. 5, 2013.
[10] D. Y. Jiang, J. M. Qin, X. Wang, S. Gao, Q. C. Liang, and J. X. Zhao, "Optical properties of NiO thin films fabricated by electron beam evaporation," Vacuum, vol. 86, no. 8, 1083-1086,2012.
[11] I. Fasaki, A. Koutoulaki, M. Kompitsas, and C. Charitidis, "Structural, electrical and mech-anical properties of NiO thin films grown by pulsed laser deposition," Appl. Surf. Sci., 257, 2, (2010) 429-433, 2012.
[10] KunduMand Liu L' Binder-free electrodes consisting of porous NiO nanofibers directly electrospun on nickel foam for high-rate supercapacitors Mater. Lett. Vol. 144, pp. 114-118,2015.
[11] Soomro R A, Ibupoto ZH, Abro MI and Willander M,"Electrochemical sensing of glucose based on novel hedgehog-like NiO nanostructures Sens. Actuators. B: Chem. Vol. 209, pp. 966-974, 2015.
[12] Tao K, Li P, Kang L, Li X, Zhou Q, Dong L and LiangW" Facile and lowcost combustion-synthesized amorphous mesoporous NiO/carbon as high mass-loading pseudocapacitor materials", J. Power Sources. Vol. 293, pp. 23-32 2015
[13] Thema F T, Manikandan E, Gurib-Fakim Aand MaazaM, 'Single phase Bunsenite NiO nanoparticles green synthesis by Agathosma betulina natural extract" J. Alloys. Comp. vol. 657, pp. 655-661, 2016.
[14] Gong N, Shao K, Feng W, Lin Z, LiangCand Sun Y 2011 "Biotoxicity of nickel oxide nanoparticles and bio-remediation by microalgae Chlorella vulgaris". Chemosphere, Vol. 83, pp. 510-516, 2011.
[15] M. Hafeez, R. Shaheen, B. Akram, M. Naeem Ahmed, Zain-ul-Abdin, Sirajul Haq, S. Ud Din, M. Zeb, M. A. Khan." Green Synthesis of Nickel Oxide Nanoparticles using Populus ciliata Leaves Extract and their Potential Antibacterial Applications" J. Chem., Vol. 75, pp. 168–173, 2021.
[16] O. V. Kharissova, H. V. R. Dias, B. I. Kharisov, B. O. Perez and V. M. J. Perez, The greener synthesis of nanoparticles, Trends Biotechnol., 2013, 31, 240–248. 16.
[17] D. Nath and P. Banerjee, Green nanotechnology a new hope for medical biology, Environ. Toxicol. & Pharmacol., 2013, 36, 997–1014.
[18] Iqbal J, Abbasi B A, Mahmood T, Kanwal S, Ali B, Shah S A and Khalil A T "Plant-derived anticancer agents: a green anticancerapproach Asian. Pac. J. Trop. Biomed. Vol. 7, pp. 1129-1150, 2017.
[19] H. Joy Prabu, I. Johnson, Plant-mediated biosynthesis and characterization of silver nanoparticles by leaf extracts of Tragia involucrata, Cymbopogon citronella, Solanum verbascifolium and Tylophora ovata, Karbala Int. J. Modern Sci. Vol.1, pp.237-246, 2015.

[20] Kar A and RayAK,"Synthesis of nano-spherical nickel by templating hibiscus flower petals J. Nanosci. Nanotechnol. Vol. 2, pp. 17-20, 2014
[21] Ezhilarasi A A, Vijaya J J, Kaviyarasu K, Maaza M, Ayeshamariam A and Kennedy L J, "Cytotoxicity effect of nanoparticles against HT-29 cancer cells J. Photochem. Photobiol. B: Bio. Vol. 164, pp. 352-360, 2016.
[22] Wright GD." Resisting resistance: new chemical strategies for battling superbugs. Cell Chem Biol.Vol. 7, pp.127–132, (2000)
[23] H.G. Gebretinsae, M.G. Tsegay, Z.Y. Nuru,"Biosynthesis of nickel oxide (NiO) nanoparticles from cactus plant Extract" Materials Today: Proceedings, Vol.36, pp.566–570, 2021
[24] H.C. Ananda Murthy, Tegene Desalegn Zeleke a, K.B. Tan b, Suresh Ghotekar c, Mir Waqas Alam d, R. Balachandran e, Kah-Yoong Chan f, P.F. Sanaulla g, M.R. Anil Kumar h, C "Enhanced multifunctionality of CuO nanoparticles synthesized using aqueous leaf extract of Vernonia amygdalina plant", Results in Chemistry Vol. 3, pp. 100-141, 2021.
[25] Saion, E.; Gharibshahi, E.; Naghavi, K. Size-controlled and optical properties of monodispersed silver nanoparticles synthesized by the radiolytic reduction method. Int. J. Mol. Sci. Vol.14,pp. 7880–7896. 2013.
[26] Anandan, K.; Rajendran, V. Morphological and size effects of NiO nanoparticles via solvothermal process and their optical properties. Mater. Sci. Semicond. Process. Vo.14, pp.43-47,2011.
[27] Suresh, S.; Podder, J. Investigations on structural, optical, morphological and electrical properties of nickel oxide nanoparticles. Int. J. Nanoparticles,Vol.8,pp289-301,2015.
[28] Hu, L.; Peng, J.; Wang, W.; Xia, Z.; Yuan, J.; Lu, J.; Huang, X.; Ma, W.; Song, H.; Chen, W.; et al. Sequential Deposition of CH3NH3PbI3 on Planar NiO Film for Efficient Planar Perovskite Solar Cells. ACS Photonics,Vol.1, pp.547-553, 2014.
[29] Zhai, Z.; Huang, X.; Xu, M.; Yuan, J.; Peng, J.; Ma, W. Greatly Reduced Processing Temperature for a Solution-Processed NiO x Buffer Layer in Polymer Solar Cells. Adv. Energy Mater.Vol.3, pp. 1614-1622, 2013.
[30] R. Guzatto, D. Defferrari, Q. B. Reiznautt, Í. Cadore, and D. Samios, "Transesteri ication double step process odi ication or ethyl ester biodiesel production from vegetable and waste oils," Fuel, Elsevier, vol. 92, pp. 197–203, 2012
[31] F. Tahira, S. T. Hussain, S. D. Ali, Z. Iqbal, and W. Ahmad,"Homogeneous catalysis of high free fatty acid waste cooking oil to fatty acid methyl esters (Biodiesel)," International Journal of Energy and Power, vol. 1,, pp. 31-36, 2012.
[32] Sarwar A, Katas H, Samsudin SN, Zin NM. Regioselective sequential modification of chitosan via azide-alkyne click reaction: synthesis, characterization, and antimicrobial activity of ahitosan derivatives and nanoparticles. PLoS One., Vol. 10, pp. 123084. 2015.
[33] Normani S, Dalla Vedova N, Lanzani G, Scotognella F, Paternò GM. Bringing the interaction of silver nanoparticles with bacteria to light. Biophys Rev. Vol. 2, pp. 021304, 2021.
[34] Ahmed N. Abd, Mohammed F. Al–Marjani, Zahraa A. Kadham "Antibacterial Activity Of Cadmium Oxide Nanoparticles Synthesized By Chemical Method", Journal of Multidisciplinary Engineering Science and Technology (JMEST), Vol. 3 pp. 2458-9403, 2016.
[35] Omar Fadhil Abdullah, Saadoo M. Abulkarem, Wedian K. Abad, "Selenium Dioxide Nanoparticles from Hibiscus Sabdariffa Flower Extract Induce Apoptosis in Bacterium (Gram-negative, Gram-positive) and Fungi", NeuroQuantology, Vol. 20: 198-203, 2022.
[36] Duha M. A. Latif, Hind A. Mahdi, Firas Kadhim Nsaif, Ahmed Naj Abd, "Synthesis and Study NiO Charactrization of Extract from Green Tea Plant Prepared by Chemical Method" NeuroQuantology, Vol. 18, pp. 83-87, 2020.

(UV) Radiation Dosimetry Sensor Based on Modified Optical Fiber

Wasmaa Jabbar, Ismaeel Al-Baidhany, Hayim Ch. Magid
Mustansiriyah University, College of Education, Department of Physics
wasmaajabbar@uomustansiriyah.edu.iq, ismaeel_2000@uomustansiriyah.edu.iq

Abstract
Optical fibers radiation dosimetry system and due to a number of advantages are becoming more important and increasingly widely used industrial and clinical environments, when they possess over conventional sensors. To monitoring in the high-radiation environments. The irradiation effects on various optical fibers were determined under different irradiation conditions. The ratio of the power distribution between the core and clad of fiber selected to be a sensitive function of the index difference, which depends on the effect of temperature changes on the transmission of the fiber when cladding is made lossy.
This study is useful for in designing optical fiber radiation Dosimeters to investigate the influence of doping effect on the fiber sensitivity under radiations source UV- radiation.
Final conclusions Conclusion shows that there is potential for ultrasensitive temperature sensors using optical fiber technology to be applicable to the measurement of absorbed dose. The relative sensitivity according to wavelength transmitted light intensity and (phase\ wavelength) shift for such fiber dosimeter as a function to dose range and temperature variation.

الخلاصة:
أصبح نظام قياس الجرعات الإشعاعية الضوئية وبسبب عدد من المزايا أكثر أهمية وأكثر استخدامًا للبيئات الصناعية والسريرية على نطاق واسع، عندما تمتلك أجهزة استشعار تقليدية. للرصد في البيئات عالية الإشعاع.
تم تحديد تأثيرات التشعيع على الألياف الضوئية المختلفة تحت ظروف إشعاع مختلفة. تم اختيار نسبة توزيع الطاقة بين اللب والألياف المكسوة لتكون دالة حساسة لفرق المؤشر، والتي تعتمد على تأثير التغيرات في درجات الحرارة على انتقال الألياف عند فقدان الكسوة.
هذه الدراسة مفيدة في تصميم مقاييس الجرعات الإشعاعية بالألياف الضوئية للتحقق من تأثير المنشطات على حساسية الألياف تحت مصدر الأشعة فوق البنفسجية والأشعة السينية.
الاستنتاجات النهائية تبين الخاتمة أن هناك احتمالية لأن تكون حساسات درجة الحرارة فائقة الحساسية تستخدم تقنية الألياف الضوئية قابلة للتطبيق على قياس الجرعة الممتصة. الحساسية النسبية وفقًا لطول الموجة المرسل شدة الضوء و(الطور/ الطول الموجي) لمقياس جرعات الألياف كدالة لنطاق الجرعة وتغير درجة الحرارة.

Introduction

Radiation is the emission or transmission of energy in the form of waves or particles through space or through a material medium [1]. In fact, people are much more exposed daily to radiation from many other sources, including the atmosphere and the Earth as well as from applications used in medicine and industry. In 1955, nuclear weapon tests raised public concerns about the effects of atomic radiation on air, water and food. In response, the United Nations General Assembly established the United Nations Scientific Committee on the Effects of Atomic Radiation (UNSCEAR) to collect and evaluate information on the levels and effects of radiation exposure. There are two forms of radiation (ionizing and non-ionizing radiation), non-ionizing radiation, such as radio waves, visible light or ultra-violet radiation (Ultraviolet radiation except for the very shortest wavelengths), infrared, microwaves, and sunlight [2]. Ionizing radiation (Indirectly ionizing such as X-ray, γ- ray), directly ionizing and may be subdivided into two families based on their mass: heavy charged particles such as protons or α particles and light ones such as the β particles, neutrons [2], [3].

(UV) radiation dosimetry Experiment

This experiment represents the second research stage in the field of the use of fiber optic sensors as (UV) radiation dosimetry.

Samples Preparation

For the purpose of preparing samples for optical fiber sensors for use in experimental experiments and practical laboratory measurements, an MMF type optical fiber has been used commercially and with standard dimensions that represent the ratio between the basic diameter/ cladding dimensions being (50/125) microns [4]. The sensitization zone was determined to be within 4 cm in the center of the commercial fibers and after it was stripped from the plastic wrap using the chemical solutions of acetone, the sensitization area was then immersed with a dilute solution of HF acid for different periods of time and after that we wash it several times to ensure the removal of the acid residue as shown in Figure (1).

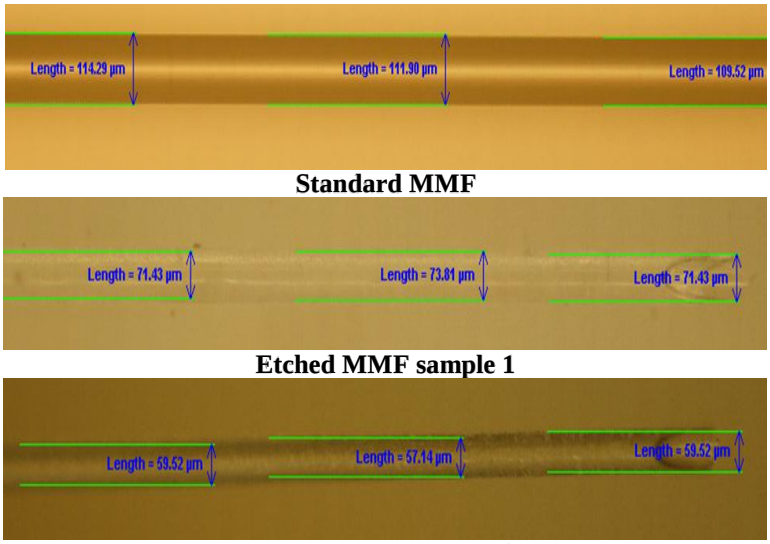

Standard MMF

Etched MMF sample 1

Etched MMF sample 2

Figure (1): MMF Samples preparation by etching

The excavated area was immersed in a solution of Ge nanoparticles at a concentration of 5% wt. which is a very important step to obtain a modified sensor and sensor area which will give it better properties as shown in Figure (2).

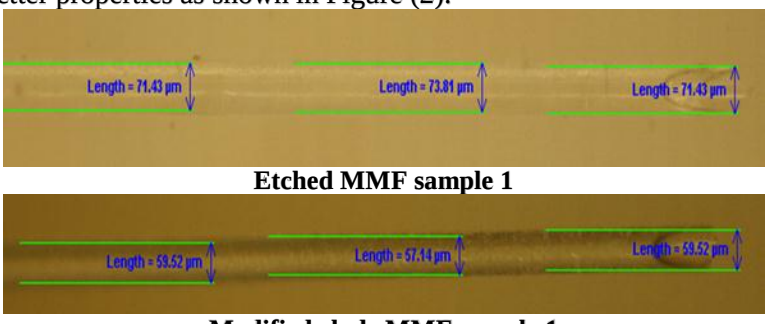

Etched MMF sample 1

Modified clade MMF sample 1

Figure (2): MMF Samples preparation by etching and modified clade sample.

The chemical etching process, which controls the required fiber diameters that are monitored and controlled by connecting the optical fiber input port to the laser source at the wavelength of 1550 nm and controlling the output of the blasting beam and its energy, which depends on the amount of losses caused by removing part of the cladding surrounding the core as shown in Figure (3) for MMF Samples preparation by etching [5].

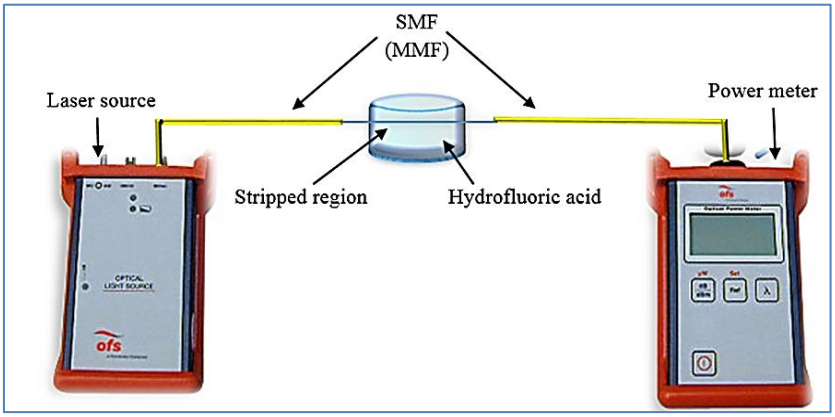

Figure (3): Real time monitoring technique for etching control.

(UV) Radiation Dosimetry Experimental Setup

Figure (4) illustrates the experimental set up (schematic diagram) and the measuring procedures of the radiation responses for the multi-mode optical fibers exposed to pulsed UV- radiation are explained [6].

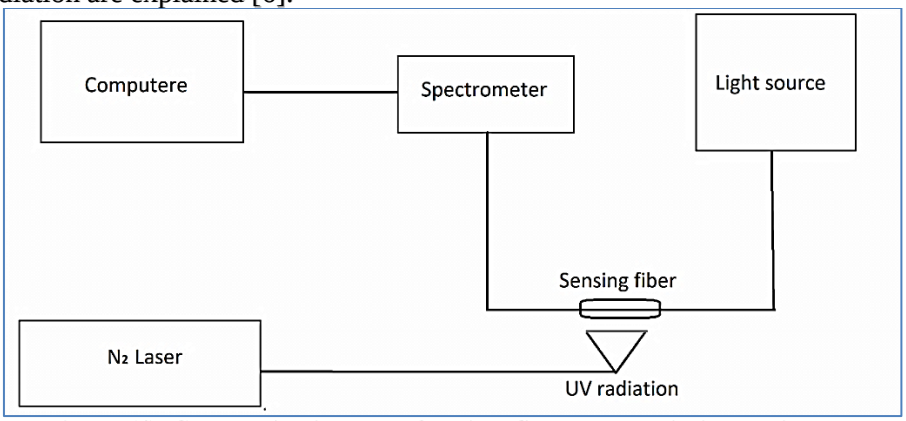

Figure (4): Schematic diagram of optical fiber UV- radiation dosimeter.

Figure 5 illustrates the laboratory practical aspect of testing and studying the properties of the optical fiber ray sensor in ultraviolet ranges, and for you by connecting one end of the fiber sensor to the Ocean Optics DH-2000 light source that emits light in the UV-VIS-NIR ranges Where the light is sent as a transmission signal through optical fibers while the other end of the optical fiber sensor has been interleaved to an Ocean Optics HR2000 optical spectrum analyzer that operates within the UV-VIS-NIR ranges and through which the window signal that reflects the sensor's properties is analyzed. The recorded and achieved spectral measurements of different diameter fibers included two phases [7]. The first is to perform measurements of the resulting optical signal for standard and modified multimeter fibers and the sensors directly without exposing them to any irradiation, while the second stage is to perform measurements of the resulting optical signal for the standard and modified multimode fibers multimode to verify the losses caused by Absorption (RIA) by setting the sensitive portion of the optical fiber (sensor) on a glass slide [8], and then exposing it to a UV radiation source (1) cm between the sensor and the radiation source Ultraviolet radiation emitted from a pulsed nitrogen laser source model N2 (MNL-100) with a wavelength of (337.1) nm, and a factor with a repeat rate of (60) Hz, with a pulse duration of (2.5) ns, and with energy ranges (0 to 40) µj.

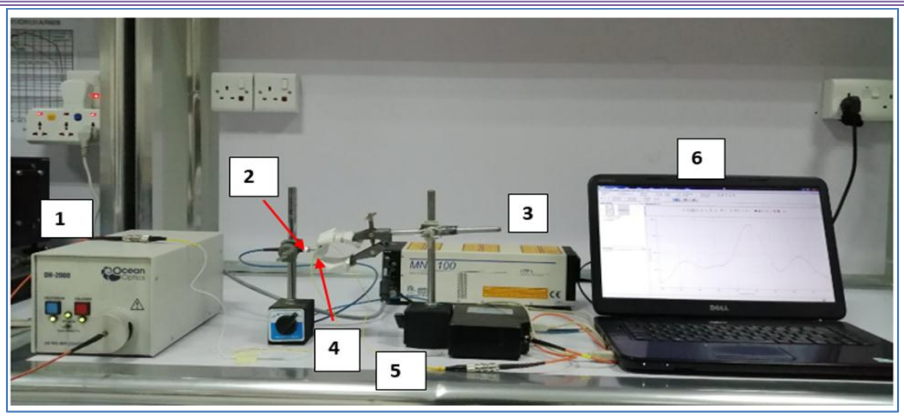

Figure (5): Experimental set up photograph of optical fiber UV- radiation dosimeter. 1-source, 2-UV-Probe, 3-N2 laser, 4-Sensor fiber, 5-OSA, 6- computer.

Radiation Sensor

A new and novel radiation sensors had been submitted in this work as far as authors know. This was achieved through using the commercially available single mode fibers (SMF) core /cladding diameter 8/125 µm and multimode fibers (MMF) core /cladding diameter 62/125 µm were used in this experiment [8]. First, the middle region of fibers were stripped and cleaned very well by immersing them in acetone solution, after that they were etched in HF solution of 40% concentration in different times in order to get different fibers' diameters (35 min of etching resulted in 60 µm diameter and 45 min. of etching resulted in 50 µm diameter).Then the etched fibers were cleaned well by dipping them several times in distilled water to remove all HF residues [9]. The etched region had been dipped in 5% wt. of Germanium solution to obtain germanium coated-cladding optical fiber. The purpose of the dipping process was to get a modified cladding of fiber which represents the sensing element of the submitted sensor. The optical fiber sensor samples are the same samples which prepared for both temperature and UV- radiation dosimeter samples.

Light Measurement Instrument

The Ocean Optics HR2000 spectrometer in the UV-VIS-NIR range used to detect the spectral resolving part of the output optical signal. This spectrometer was used in testing by both facilities. The spectrometer plugs into a laptop which runs the Ocean Optics Spectra Suite spectrometer software. This software enables the user to monitor and record resultant spectra measurements from the tested optical fiber sensors [10].

(UV) Radiation Dosimetry Experiment Results & Discussions

The results of the measurements will be reviewed for laboratory experiments related to testing and evaluating the performance of fiber optic radiation sensors within the UV ranges, which are represented by (337.1 nm) wavelength N_2- pulsed laser model (MNL-100) with (60 Hz) repetition rate, (2.5 ns) pulse duration and from (0 to 40) µj varying pulse energy in order to investigate the RIA spectra resulted from this approach, as shown in Figure (5). The different responses of the both single mode and multimode fibre samples are illustrated in the previous Figures [11]. The absorption spectrum of fibre samples; sleeve bare, clad tapered, and finally Ge –dipped sensor fibres without irradiation exposure shown in Figure (6).

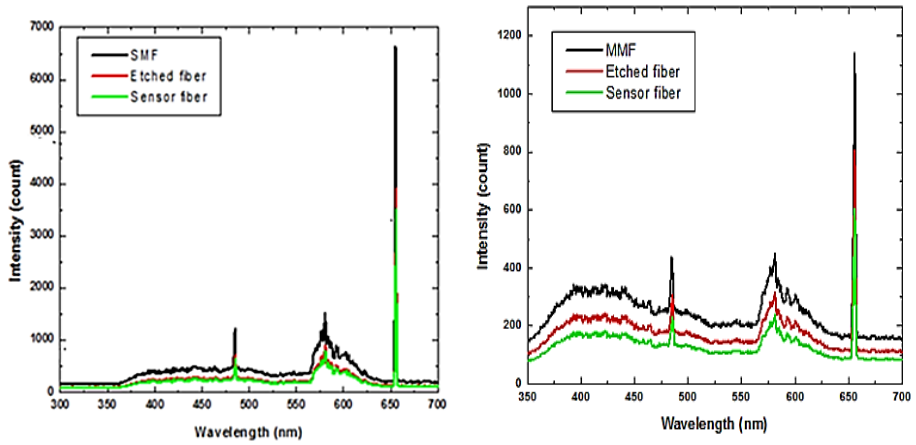

Figure (6): The Absorption spectrum of(left)SMF,(right) MMF fiber samples; sleeve bare, clad tapered, and Ge –dipped sensor fibers without irradiation exposure.

First case: Figure (6) shows the SMF absorption spectra of a (65 µm) diameter of: sleeve bare, clad tapered, and Ge–dipped fiber sensors.
Figure (6): SMF absorption spectra of a (65 µm) sleeve bare, clad tapered, and Ge –dipped fiber sensors.

Table (1) shows a comparison between the SMF absorption spectra with different (65 and 60 µm) diameters of: sleeve bare, clad tapered, and Ge –dipped fiber sensors as a function of UV-irradiation energy.

Table (1): A comparison between the SMF peaks absorption spectra with different (65 and 60 µm) diameters of: sleeve bare, clad tapered, and Ge –dipped fiber sensors

SMF diameter (µm)	65			60		
Fiber type	Sleeve bare	Clad tapered	Ge-dipped sensor	Sleeve bare	Clad tapered	Ge-dipped sensor
Absorption wavelengths (nm)	655.82 581.08 485.52	656.02 581.28 485.72	656.09 581.35 485.83	655.82 581.08 485.52	656.07 581.33 485.77	656.22 581.48 485.92

Figure (7) shows the SMF peaks absorption intensities of (65 µm) diameter of: sleeve bare, clad tapered, and Ge –dipped fiber sensors as a function of UV-irradiation energy.

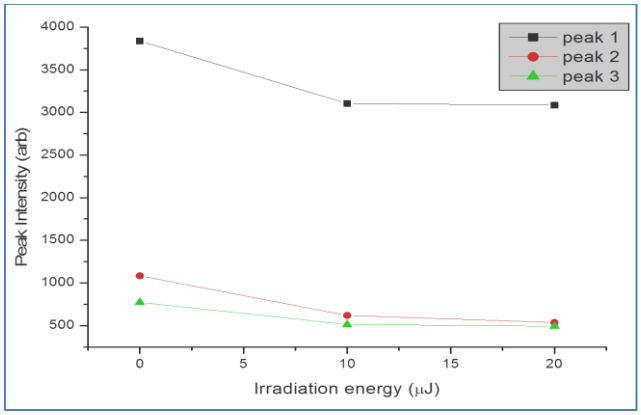

Figure (7): The SMF peaks absorption intensities of (65 µm) diameter of: sleeve bare, clad tapered, and Ge –dipped fiber sensors as a function of UV-irradiation energy.

Figure (8) shows the SMF absorption spectra of a (60 µm) diameter of: sleeve bare, clad tapered, and Ge-dipped fiber sensors.

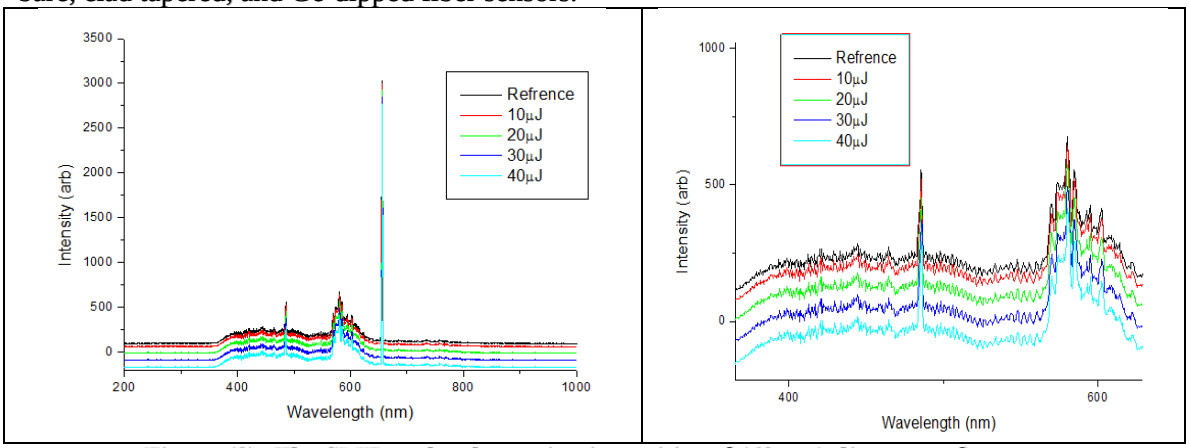

Figure (8): The SMF peaks absorption intensities of (60 µm) diameter of different radiation energy.

While Table (2) shows the SMF peak absorption wavelengths of a (60 µm) diameter of different radiation energy.

Table (2): The SMF peak absorption wavelengths of a (60 µm) diameter of different radiation energy.

Peak (nm)	Reference Intensity (counts)	10(µJ) Intensity (counts)	20(µJ) Intensity (counts)	30(µJ) Intensity (counts)	40(µJ) Intensity (counts)
656.2	3030	2995	2925	2845	2766
580.17	678	643	532	372	292
483.22	536	522	360	280	200

Figure (9) shows the SMF peaks absorption intensities of (60 µm) diameter of of different radiation energy.

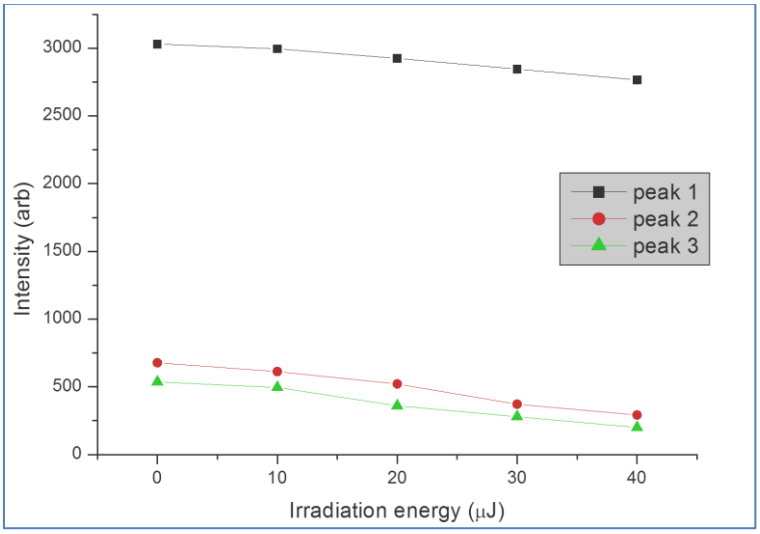

Figure (9): The SMF peaks absorption intensities of (60 µm) diameter of different radiation energy.

Second case: The same above measurements sequence done but for MMF sensor with UV irradiation. Figure (10) shows the MMF absorption spectra of a (65 µm) diameter of: sleeve bare, clad tapered, and Ge –dipped fiber sensors.

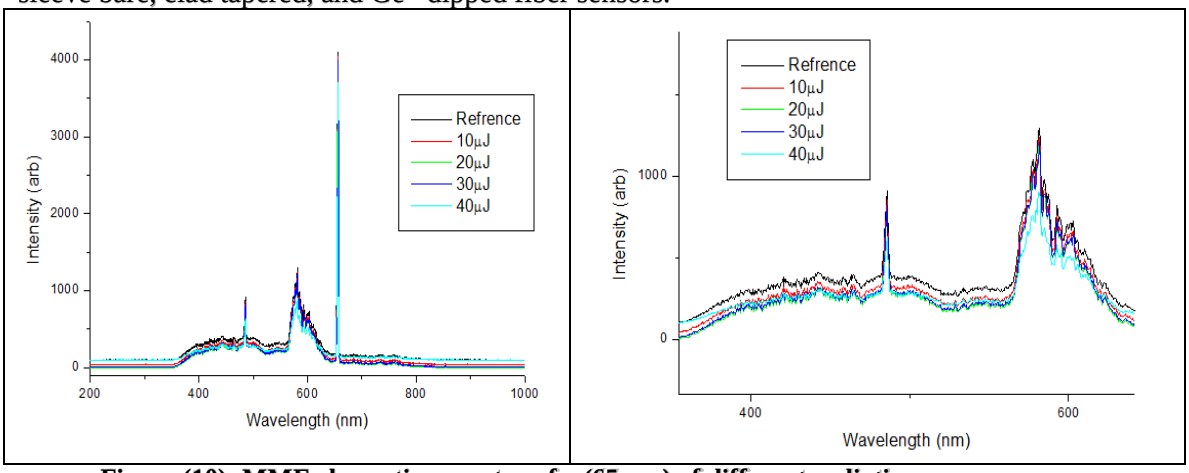

Figure (10): MMF absorption spectra of a (65 µm) of different radiation energy.

While (Table 3) shows the MMF peak absorption wavelengths of a (65 µm) diameter of different radiation energy.

Table (3): The MMF peak absorption wavelengths of a (65 µm) diameter of different radiation energy.

Peak (nm)	Reference Intensity (counts)	10(µJ) Intensity (counts)	20(µJ) Intensity (counts)	30(µJ) Intensity (counts)	40(µJ) Intensity (counts)
655.82	4095	4035	3995	3885	3707
579.73	1124	1064	1024	1014	861
495.06	846	854	814	756	597

Figure (11) shows the MMF peaks absorption intensities of (65 µm) diameter of: sleeve bare, clad tapered, and Ge–dipped fiber sensors as a function of UV-irradiation energy.

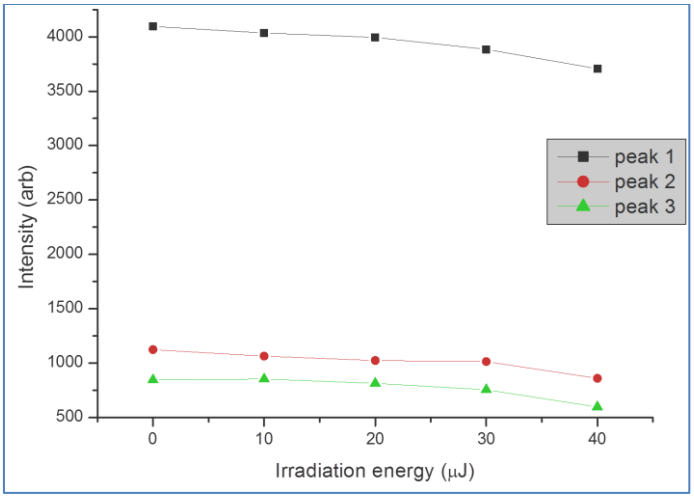

Figure (11): The MMF peaks absorption intensities of (65 µm) diameter of different radiation energy.

Figure (12) shows the MMF absorption spectra of a (60 µm) diameter of: sleeve bare, clad tapered, and Ge –dipped fiber sensors. While (Table 4.4) shows the MMF peak absorption wavelengths of a (60 µm) diameter different radiation energy.

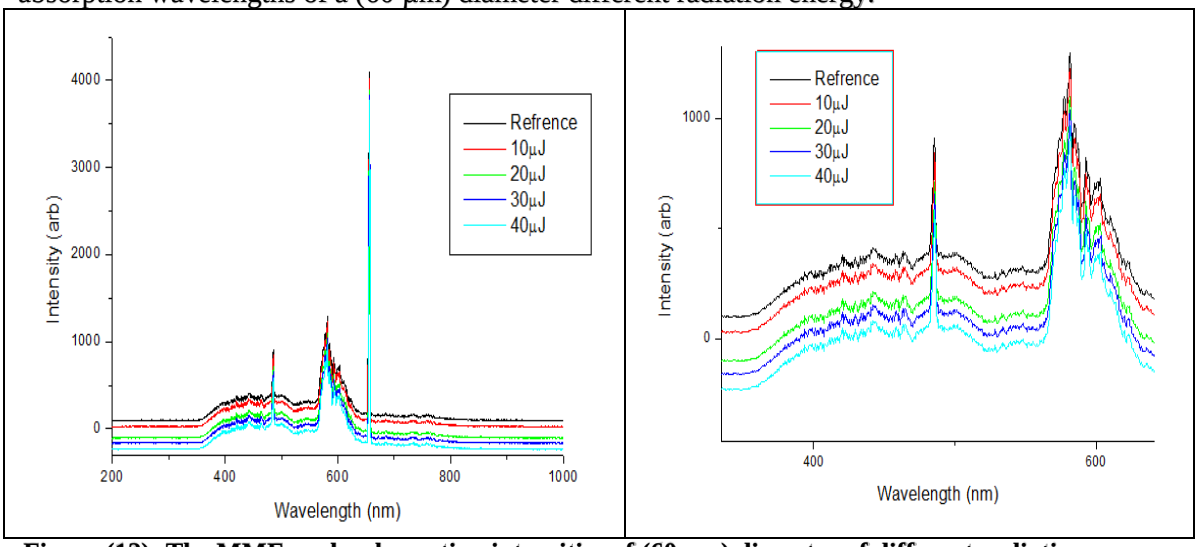

Figure (12): The MMF peaks absorption intensities of (60 µm) diameter of different radiation energy

Table (4): The MMF peak absorption wavelengths of a (60 µm) diameter of different radiation energy.

Peak (nm)	Reference Intensity (counts)	10(µJ) Intensity (counts)	20(µJ) Intensity (counts)	30(µJ) Intensity (counts)	40(µJ) Intensity (counts)
653.22	4115	4025	3895	3835	3665
577.03	1104	1045	1000	943	790
499.36	875	776	714	586	515

Figure (13) shows the MMF peaks absorption intensities of (60 µm) diameter of different radiation energy.

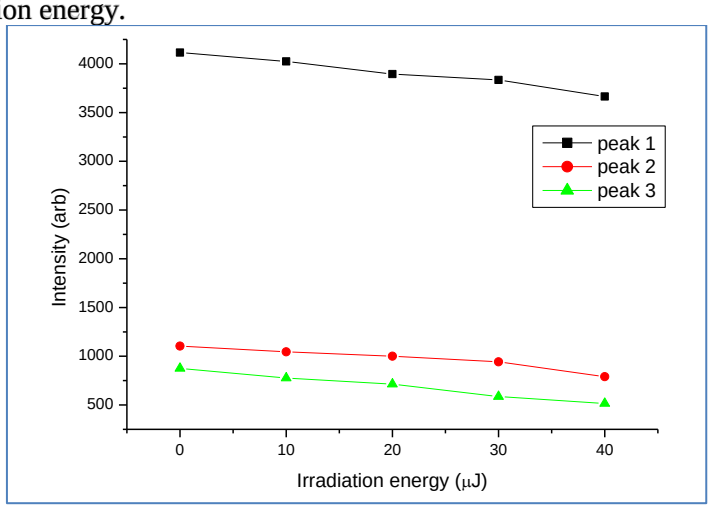

Figure (13): The MMF peaks absorption intensities of (60 µm) diameter of different radiation energy

Table (5) shows a comparison between the MMF absorption spectra with different (65 and 60 µm) diameters of: sleeve bare, clad tapered, and Ge-dipped fiber sensors.

Table (5): A comparison between the MMF peaks absorption spectra with different (65 and 60 µm) diameters of: sleeve bare, clad tapered, and Ge –dipped fiber sensors.

MMF diameter (µm)	65			60		
Fiber type	Sleeve bare	Clad tapered	Ge-dipped sensor	Sleeve bare	Clad tapered	Ge-dipped sensor
Absorption wavelengths (nm)	655.82	579.73	495.06	653.22	577.03	499.36
	577.03	581.28	581.35	577.03	581.33	581.48
	499.36	485.72	485.83	485.52	485.77	485.92

From the above results and as discussions its well noticed that decreasing of intensity values and shifting towards the long wavelengths recorded by the optical spectrum analyzer for tapered and Ge –dip fiber sensor as compared with sleeve bare ones, due to the fact the evanescent signal interaction with surrounding environment, while this evanescent wave is absorbed by the Ge- dipped on its modified cladding and the existed absorption defects. In other side, the decreasing and shifting of the peak intensity is more obvious for the 60 µm fiber than the 65 µm fiber, due to the less the diameter of the fiber cladding the more evanescent field escape outwards and finally the more decreasing of spectrum intensity. As the UV irradiation energy increases, the light intensity decreases due to larger attenuation growth in the irradiated Ge dipped fiber sensor at the highest exposed energy of UV source. The RIA decreases spatially due to the role of Ge dopant in governing the fiber response to radiation and the nature of defects involved in the absorptions process.

Conclusions

According to the results obtained in the previous chapters, specifically with regard to the simulation aspect and laboratory practical results for the evaluation of performance of samples of radiation sensors based on optical fibers, we would like to confirm the following conclusions:

In case of **(UV) radiation dosimetry Laboratory Experiment**, for germanium-coated cladding fiber at low irradiation energies, modified cladding fibers sensitivity to the radiation is strongly wavelength dependent. The dopant material (Ge) creating guiding modes for optical signal passed through the fibre and confining features by controlling refractive-index profile and enhancing sensing characteristics. Also, the glass provides very low attenuation, to reduce the levels of absorption and scattering to be close to their theoretical limits. Such results are very supportive to understand the better performance depending on the fibre structure, dopant material and irradiation properties.

References

[1] Weisstein, Eric W. "Radiation". Eric Weisstein's World of Physics. Wolfram Research. Retrieved 2014-01-11.

[2] Introduction to Radiation, December 2012, Introduction to Radiation Minister of Public Works and Government Services Canada (PWGSC) 2012 PWGSC catalogue number CC172-93/2012E-PDF ISBN 978-1-100-21572-3 Published by the Canadian Nuclear Safety Commission (CNSC).

[3] Iacopo Toccafondo, Fabrizio Di Pasquale, Markus Brugger, "Distributed Optical Fiber Radiation and Temperature Sensing at High Energy Accelerators and Experiments, Thesis, distudi Universitari edi Perfezionamento, Scuola Superiore Sant", Anna, Anno Accademico 2014-2015.

[4] T. Shikama, K. Toh, S. Nagata, and B. Tsuchiya, "Optical dosimetry for ionizing radiation fields by infrared radioluminescence", IOP Publishing Ltd., Measurement Science and Technology, Vol. 17. No. 5, 2006.
[5] Jackson, D. A. (2004), "Novel fibre optic based ionization radiation probe", paper presented at 2nd European Workshop on Optical Fibre Sensors, Proceedings Vol. 55502, Proceedings Vol. 5502, Santander, Spain.
[6] Mignani, A. G., Romano, S., Fusi, F. and Mencaglia, A., "Radiation dosimetry in radiotherapy: a model for an extrinsic optical fiber sensor", in Culshaw, B. and Jones, J. (Eds), paper presented at European Workshop on Optical Fibre Sensors, Proceedings of SPIE, Vol. 3483, 1998, Peebles, Scotland, UK.
[7] Dario Alasia, A. Fernandez Fernandez, B. Brichard, Laura Abrardi, Luc Thévenaz1, "Study of the radiation effects on the properties of Brillioun scattering in standard Ge-doped optical fibres", paper presented at 17th International Conference on Optical Fibre Sensors, SPIE, Bruges, 17th International Conference on Optical Fibre Sensors, Marc Voet, Reinhardt Willsch, Wolfgang Ecke, Julian Jones, Brian Culshaw, eds., Proceedings of SPIE Vol. 5855, 2005, Bruges, Belgium.
[8] Huston, A. L., Justus, B. L., Falkenstein, P. L., Miller, R.W., Ning, H. and Altemus, R. (2001), "Remote optical fibre dosimetry", Nuclear Instruments and Methods in Physics Research Section B: Beam Interactions with Materials and Atoms , vol. 184, Issues 1–2, September 2001, pp. 55-67.
[9] Brichard, B., Borgermans, P., Fernandez, A. F., Lammens, K. and Decreton, M. (2001), "Radiation effect in silica optical fiber exposed to intense mixed neutron-gamma radiation field", IEEE Transactions on Nuclear Science, December 2001, Vol. 48, Issue 6, pp. 2069-2073.
[10] Brichard, B., Fernandez Fernandez, A., Ooms, H., Borgermans, P. and Berghmans, F., "True doserate enhancement effect in phosphorous doped fibre optic radiation sensors", paper presented at Second European Workshop on Optical Fibre Sensors, Proceedings of the SPIE, Vol. 5502, pp. 184-187, 2004, Santander, Santander, Spain.

A Study of the Correlation between the Bulge Dynamical Masses and Spiral arm Pitch Angles in Spiral Galaxies

Ismaeel Al-Baidhany, Wasmaa Jabbar, Hanaa Kadham Essa
Mustansiriyah University, College of Education, Department of Physics
wasmaajabbar@uomustansiriyah.edu.iq, ismaeel_2000@uomustansiriyah.edu.iq

Abstract

In this work, the measurement of the bulge dynamical masses (M_{dyn}) for a sample of 40 galaxies are studied by applying the relationships between (σ_{*}) and (R_e) are the host-galaxy bulge velocity dispersion and the bulge effective radius respectively.

The Mid-Infrared (MIR) views of (M_{dyn}) scaling relations are presented based on a two-dimensional decomposition of Spitzer/IRAC 3.6 micron images. From this, accurate bulge parameters for 40 spiral galaxies have been derived and presented. Spitzer/IRAC provides high-quality imaging data for this sample, and the sensitivity of this instrumentation permits the clear identification of morphological features.

These bulge structural parameters are used to determine several M_{dyn} and galaxy morphological scaling relations. These include the bulge dynamical mass-spiral arm pitch angle (M_{dyn}- P) relationship. In all three cases, strong correlations are found.

Hence, spiral arm pitch angle is a parameter that can be used to determine indirect measurements of the bulge dynamical mass.

المستخلص:

في هذا العمل ، تمت دراسة لقياس الكتل الديناميكية المنتفخة (M_{dyn}) لعينة من 40 مجرة من خلال تطبيق العلاقات بين (σ *) و(R_e) وهي تشتت سرعة انتفاخ المجرة المضيفة ونصف قطر الانتفاخ الفعال على التوالي.

يتم تقديم عروض منتصف الأشعة تحت الحمراء (MIR) لعلاقات الارتباط (M_{dyn}) بناءً على تحليل ثنائي الأبعاد لصور Spitzer/ IRAC 3.6µm. تم اشتقاق وتقديم معلمات انتفاخ دقيقة لـ 40 مجرة حلزونية. يوفر Spitzer IRAC بيانات تصوير عالية الجودة لهذه العينة، وتسمح حساسية هذه الأجهزة بتحديد واضح للسمات المورفولوجية.

تُستخدم هذه المعلمات الهيكلية للانتفاخ لتحديد العديد من علاقات التحجيم المورفولوجية في M_{dyn} وتشمل هذه العلاقة بين الكتلة الديناميكية المنتفخة وزاوية ميل الذراع الحلزونية (M_{dyn}-P) في جميع الحالات الثلاث. ومن ثم فإن زاوية ميل الذراع الحلزونية هي معلمة يمكن استخدامها لتحديد القياسات غير المباشرة للكتلة الديناميكية المنتفخة.

Introduction:

In 1968, the American physicist John Archibald Wheeler used the term “black hole” (Hooft 2009). By the 1960s, the concept of black holes had generated great interest among physicists, astronomers, and the other people as well.

Astronomers observed many types of black holes which can be classified into three groups: stellar mass black holes, intermediate mass black holes (IMBHs) and supermassive black holes (SMBHs) (Gebhardt & Rich 2005). The distinction between normal black holes and SMBHs is that normal black holes are believed to be the end point of stellar evolution for the most massive stars. The possible end products of stellar evolution are white dwarfs, neutron stars (usually observed as pulsars), and black holes. Stars that have masses greater than around 5 times the mass of the Sun may end up as a black hole (Valeri & Igor 1998).

A SMBH is the largest type of black hole. They are typically found in the centers of galaxies, with masses in the range $\approx 10^5$ to $10^9 M_{\odot}$.

Supermassive black holes (SMBHs) are common at the center of all or most of galaxies (Mogorrian et al., 1998; Ferrarese & Merritt, 2000) as observed at high sensitivities and resolution with the Hubble Space Telescope (HST). In addition, their masses are in the range of hundreds of thousands to billions of solar masses (Kormendy & Richstone 1995; Richstone et al. 1998; Kormendy & Gebhardt 2001).

Over the last decade, studies of galaxies have led to the discovery that there are many strong or tight correlations locally between the masses of the SMBHs and the global properties of the spheroid components of their hosts. This suggests an intriguing link between galaxy formation and SMBH growth (Yuexing 2007). As a result, astrophysicists believe that the energy released by growing SMBHs play important role in shaping the properties of the structure of their host galaxies (Benson 2010; Fabian 2012).

Measuring the spiral arm pitch angle

Previous studies described logarithmic spiral in polar coordinates (Lin & Shu 1964; Kennicutt 1981; Elmegreen & Elmegreen 2004; Seigar & James 1998a, b, 2002; Seigar et al. 2006; Vallée 2002). This is a special kind of spiral curve that describes the arm in disk galaxies:

$$r = r_0 e^{\theta \tan(\varphi)} \quad \ldots(1)$$

where r is radius, θ is central angle, r_0 is initial radius when θ = 0, and pitch angle is $-90 \leq \Phi \leq 90$.

Because the spiral arm pitch angle has been shown to be independent of the wavelength at which it is measured, multi-band images were used to determine it for our sample of spiral galaxies (Seigar et al. 2006a).

Spiral arm pitch angles were measured using a two-dimensional fast Fourier transform (2DFFT) decomposition with logarithmic spirals of Spitzer/ IRAC 3.6 μm images of 40 galaxies (Table 2), with inclinations of $30^o \leq i \leq 60^o$. The 2DFFT program analyzes images of spiral galaxies and categorizes their pitch angles and number of arms. The two-dimensional fast Fourier transform decomposition program is fully described by I. Puerari in Schröder et al. (1994). The amplitude of each Fourier component is given by:

$$A(m,p) = \frac{\sum_{i=1}^{I}\sum_{j}^{J} I_{ij}(\ln r,\theta)\exp[-i(m\theta + p * \ln r)]}{\sum_{i=1}^{I}\sum_{j=}^{J} I_{ij}(\ln r,\theta)} \quad \ldots(2)$$

where r and θ are polar coordinates, I(ln r, θ) is the intensity at position (ln r, θ), m represents the number of arms or modes, and p is the variable associated with the pitch angle P defined by $P = -(m/p_{max})$.

IRAF was used to determine the ellipticity values and major-axis position angle in order to deproject the 3.6 μm galaxy images to fully face-on by assuming circular outer isophotes. ELLIPSE in IRAF was used to derive inclination angle (α); (Hubble 1926; Jedrzejewski 1987), which is defined by:

$$\alpha = \cos^{-1}(b/a) \quad \ldots(3)$$

Where (a) is the semi-major axis and (b) is the semi-minor axis, where the value 0^o describes a face-on galaxy and 90^o describes an edge-on galaxy.

Measurement of the dynamical bulge mass

In this part the methods used to derive the dynamical bulge mass are described. The bulge's dynamical mass (M_{dyn}) were estimated by using the virial theorem, i.e. the virial bulge mass given by:

$$M_{dyn} = kR_e\sigma^2/G \quad (4)$$

where k is a model dependent dimensionless constant (Hu 2009) or is in general a function of the Sérsic index n. (Cappellari et al. 2006 & sani et al. 2011). K is a constant throughout the galaxy in the isothermal model, and its value is determined numerically, K=3 (Gebhardt et al. 2003), 8/3 (MH03), 3 (Hu 2009) and 5 (Sani et al 2011), we follow Sani (2011) to use k = 5 instead of 8/3 or 3.

where k is in general a function of the Sérsic index n (as in Hu J. 2009, Marconi et al. 2003, Sani et al. 2011), $\sigma_*$and R_e are the host-galaxy bulge velocity dispersion and the bulge effective radius respectively, and G is the gravitational constant.

Result and Discussion:

M_{dyn} − P Correlation:

The M_{dyn} − P correlations are shown in Figures (1), (2), and (3). In Figure (1), we found that the Pearson's linear correlation coefficient for this correlation was 0.8. This figure shows that 10 out of 25 pseudobulges galaxies (NGC4594, NGC7727, IC2560, NGC4030, NGC4151, NGC5055, NGC6300, NGC1350, NGC1566, NGC3783) are outliers of the fitting line, or not consistent with the correlation for classical bulge galaxies. While the other 15 pseudobulges and 10 classical bulges galaxies are consistent with the correlation for bulges galaxies. From Pearson's linear correlation coefficient which is 0.82, it can be concluded that most spiral galaxies, which have pseudobulges and classical bulges, have a correlation between M_{dyn} and P (Table 1). The linear fit of the relation is:

$$\log_{10}\frac{M_{dyn}}{M_{\odot}} = (11.39 \pm 0.3) - (0.062 \pm 0.007)P$$

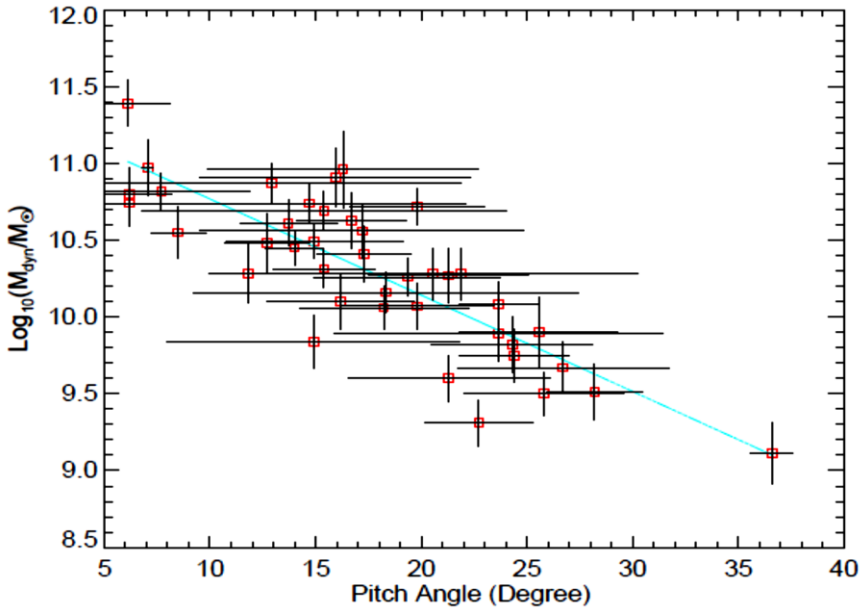

Figure (1): Bulge dynamical mass (Mdyn) as a function of spiral arm pitch angle (P). The solid line is the fit to all spiral galaxies.

Figure (2) shows the relations in M_{dyn}-P plots (we assigned markers to these galaxies according to bulges and pseudobulges). Pearson's linear correlation coefficients are found, which are 0.799 and 0.79 for the pseudobulges and classical bulges respectively. Most spiral galaxies are concluded, including pseudobulges or classical bulges have a good correlation between M_{dyn} and P (Table 1). The best-fitting lines are shown for this diagram:

$$\log_{10}\frac{M_{dyn}}{M_{\odot}} = (11.58 \pm 0.43) - (0.061 \pm 0.016)P \quad \text{(Classical bulges)}$$

$$\log_{10}\frac{M_{dyn}}{M_{\odot}} = (11.106 \pm 0.31) - (0.055 \pm 0.013)P \quad \text{(Pseudobulges)}$$

These results confirmed the observational and theoretical results that pointed out bulges in disc galaxies are divided into two kinds: classical bulges and pseudobulges (Kormendy & Kennicutt 2004, Hu 2008, Hu 2009, and Sani 2011). These results are in agreement with Kauffmann et al. (2003), which pointed out that most of the low-mass AGNs are in spiral galaxies hosts. This implied that most of these low-mass SMBHs may live in the pseudobulges.

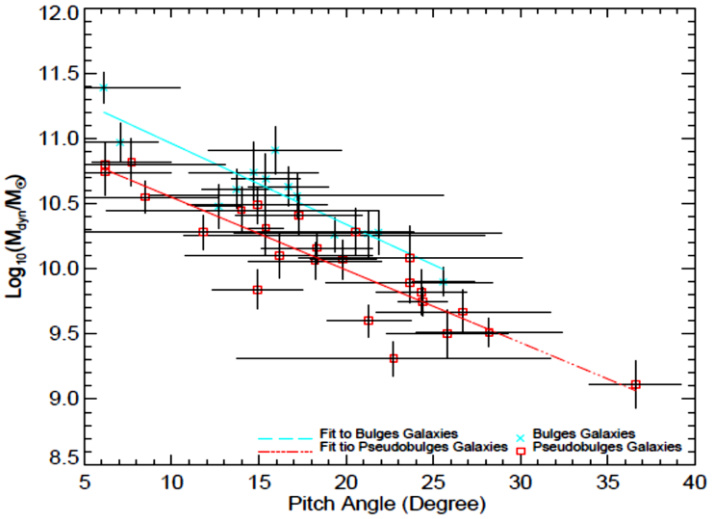

Figure (2): Bulge dynamical mass (M_{dyn}) as a function of spiral arm pitch angle (P). The linear regressions are shown as long dash and dash dot dot, respectively, for pseudobulges, and classical bulges galaxies.

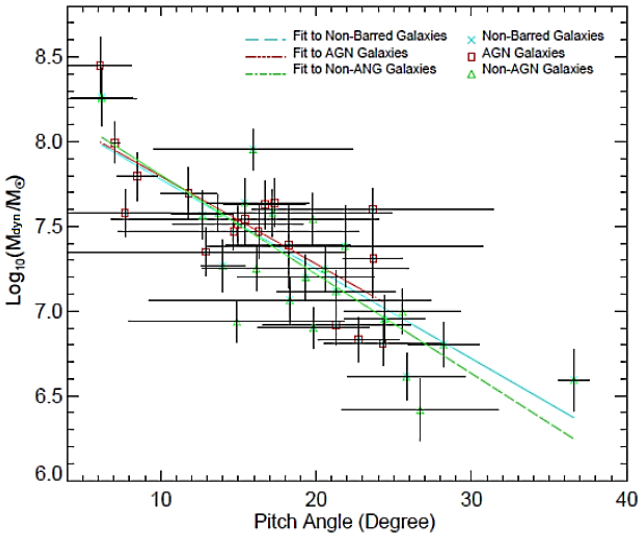

Figure (3): Bulge dynamical mass (M_{dyn}) as a function of spiral arm pitch angle. The linear regression are shown as long dash, dash dot dot dot, dash dot and dashed, respectively, for non-barred, non-AGN, and AGN galaxies.

Figure (3) shows the relations in M_{dyn}-P plots, for non-barred, non-AGN, and AGN galaxies respectively. Pearson's linear correlation coefficients for a correlation between SMBH and M_{dyn} were found to be 0.83, 0.88, and 0.81 respectively. Pearson's linear

correlation coefficient values are noted for all types of galaxies. The significance level at which the null hypothesis of zero correlation is disproved is 3σ (Table 1).
The best-fitting lines are shown for this diagram:

$$\log_{10}\frac{M_{dyn}}{M_{\odot}} = (11.408 \pm 0.4) - (0.049 \pm 0.016)P \quad (Non - Barred)$$

$$\log_{10}\frac{M_{dyn}}{M_{\odot}} = (11.54 \pm 0.35) - (0.063 \pm 0.013)P \quad (Non - AGN)$$

$$\log_{10}\frac{M_{dyn}}{M_{\odot}} = (11.409 \pm 0.5) - (0.063 \pm 0.012)P \quad (AGN)$$

Table (1): Linear correlation coefficient and linear regression coefficients of Bulge dynamical mass (M_{dyn}) as a function of spiral arm pitch angle (P) SMBHs as a function of the bulge luminosity [$\log(M_{dyn})=\alpha + \beta(P)$]:

Types of galaxies	α	β	No. of galaxies	correlation coefficient
All galaxies	11.39 ± 0.3	0.062 ± 0.01	41	0.82
Pseudobulges galaxies	11.1 ± 0.31	0.05 ± 0.01	25	0.79
Bulges galaxies	11.58 ± 0.43	0.06 ± 0.02	16	0.799
Non-Barred galaxies	11.4 ± 0.4	0.06 ± 0.02	14	0.838
AGN galaxies	11.4 ± 0.5	0.06 ± 0.01	18	0.81
Non-AGN galaxies	11.54 ± 0.35	0.06 ± 0.01	23	0.83

Table (2): Estimated Galaxy Parameters. Columns: **(1)** galaxy name. **(2)** Hubble type taken from the Hyper-Leda catalogue. **(3)** Velocity dispersion in km/s, Velocity dispersion references: (1)Hu 2009 (2) Lucey et al. 1997 (3) Beifior 2009 (4) Garcia 2003 (5) Gült 2009 (6) Davies 2009 (7) sani 2011 (8) Ferrarese 2002 (9) Deglus 1995 (10) Lauea 2002 (11) Oliva 1995 (12) Whitmore 1985 (13) Buta 2011(14) Nelson 1995(15) Ho et al. 2009(16) Greene 2006 (17) Idiart 1996 (18) Bower 1993(19) Beifior 2009 (20) Benttoni 1997(21) Plazzlla 2008(22) Laura 2008 (23) Lake 1986. **(4)** Spiral arm pitch angle (P). Most of (P) taken from Berrier et al. (2013), and Davis et al. (2012). The spiral arm pitch angle given for M31, MW, and NGC 4945 are taken from Braun (1991), Levine et al. (2006) and Burg et al. (1986) respectively. **(5)** Effective radius in (kpc). **(6)** Bulge dynamical mass.

Name (1)	Leda Type (2)	σ (km/sec) (3)	P (deg.) (4)	$M_{dyn}(M_{\Theta})$ (6)
Circinus	Sb	75	26.7	9.67±0.19
IC 2560	SBb	137	16.3	11±0.4
NGC 224	Sb	160±8	8.5±1.3	10.6±0.5
NGC 613	Sbc	125.3±18.9	23.68±1.77[(1)]	10.1±0.3
NGC 1022	SBa	99	19.83±3.6[(1)]	10.1±0.17
NGC 1068	Sb	151±7	17.3±2.2[(2)]	10.4±0.11
NGC 1097	SBb	150	16.7±2.62[(3)]	10.6±0.13
NGC 1300	Sbc	145±22	12.7±1.8	10.5±0.08
NGC 1350	Sab	120.91±2.08*	20.57±5.38[(1)]	10.3±0.13
NGC 1353	Sb	83	36.6±5.4[(1)]	9.11±0.73
NGC 1357	Sab	121±14	16.16±3.48[(1)]	10.1±0.02
NGC 1365	Sb	151±20	15.4±2.4[(3)]	10.3±0.25
NGC 1398	SBab	216±20	6.2±2[(3)]	10.8±0.23
NGC 1433	SBab	84±9	25.82±3.79[(1)]	9.5±0.034
NGC 1566	SABb	100±10	21.31±4.78[(3)]	9.6±0.032

NGC 1672	Sb	130.8±2.09*	18.22±14.07[3]	10.1±0.57
NGC 1808	Sa	148	23.65±7.77[1]	9.89±0.3
NGC 2442	Sbc	140.74±2.18*	14.95±4.2[1]	10.5±0. 32
NGC 3031	Sab	143±7	15.4±8.6	10.7±0.14
NGC 3227	SABa	128±13	12.9±9	10.9±0.06
NGC 3368	SABa	122±(28,24)	14±1.4	10.5±0.03
NGC 3511	SABc	93.56±2.04*	28.21±2.27[1]	9.51±0.13
NGC 3521	SABb	130.5±7.1	21.86±6.34[3]	10.3±0.07
NGC 3673	Sb	117.45±2.07*	19.34±4.38[1]	10.3±0.08
NGC 3783	SBab	95±10	22.73±2.58[1]	9.31±0.03
NGC 3887	Sbc	102.01±2.05*	24.4±2.6[2]	9.75±0.08
NGC 4030	Sbc	122.43±2.1*	19.8±3.2[2]	10.7±0.08
NGC 4151	SABa	156±8	11.8±1.8	10.3±0.07
NGC 4258	SABb	146±15	7.7±4.2	10.8±0.18
NGC 4462	SBab	146±8	17.2±5.42[1]	10.6±0.07
NGC 4594	Sa	240±12	6.1	11.4±0.09
NGC 4699	SABb	215±10	6.2±2.2[1]	10.7±0.06
NGC 5054	Sbc	104.48±2.05*	25.57±3.73[1]	9.9±0.13
NGC 5055	Sbc	101±5	14.9±6.9	9.84±0.37
NGC 6300	SBb	94±5	24.3±3.8[1]	9.82±0.04
NGC 6902	SBab	145.86±2.1*	13.71±2.3[3]	10.3±0.19
NGC 7213	Sa	185±20	7.05±0.28[1]	10.6±0.84
NGC 7531	SABb	108.7±5.6	18.31±9.09[1]	11±0.048
NGC 7582	SBab	137±20	14.7±7.44[3]	10.2±0.08
NGC 7727	SABa	181±10	15.94±6.39[1]	10.7±0.08

Conclusion

In this work, the following conclusions are made:

Scaling relations were studied between the bulge dynamical mass (M_{dyn}) in the center of galaxies, and spiral arm pitch angles. The bulge Sérsic index (n) and effective radius (R_e) were determined based on a 2D decomposition of 3.6 μm Spitzer/IRAC images of 41 spiral galaxies. The dispersion velocity was obtained from Hyperleda, which was used to estimate the bulge dynamical mass (M_{dyn}).

The relationships between the bulge dynamical mass (M_{dyn}) and spiral arm pitch angle (P) was found, and the best-fitting lines regressions were:

As well, the relationships between a bulge dynamical mass (M_{dyn}) and spiral arm pitch angle (P) was investigated, and the best-fitting lines regressions were:

$$\log_{10}\frac{M_{dyn}}{M_{\odot}} = (11.39 \pm 0.3) - (0.062 \pm 0.007)P$$

$$\log_{10}\frac{M_{dyn}}{M_{\odot}} = (11.58 \pm 0.43) - (0.061 \pm 0.016)P \quad \text{(Classical bulge)}$$

$$\log_{10}\frac{M_{dyn}}{M_{\odot}} = (11.106 \pm 0.31) - (0.055 \pm 0.013)P \quad \text{(Pseudobulges)}$$

$$\log_{10}\frac{M_{dyn}}{M_{\odot}} = (11.408 \pm 0.4) - (0.063 \pm 0.016)P \quad (\text{Non} - \text{Barred})$$

$$\log_{10}\frac{M_{dyn}}{M_{\odot}} = (11.54 \pm 0.35) - (0.063 \pm 0.013)P \quad (\text{Non} - \text{AGN})$$

$$\log_{10}\frac{M_{dyn}}{M_{\odot}} = (11.409 \pm 0.5) - (0.063 \pm 0.012)P \quad \text{(AGN)}$$

References

Beifiori A., Sarzi M., Corsini E. M., Dalla Bont`a E., Pizzella A., Coccato L., Bertola F., 2009, ApJ, 692, 856 (B09).
Benson, A. J., & Bower, R. 2010, MNRAS, 405, 1573, _; Benson A. J.; Bower R. (2010) MNRAS, 405, 1573-1623.
Berrier JOEL C. et al., 2013, ApJ, 769, 132.
Bettoni D., Galletta G.; 1997. Astron. Astrophys. Suppl. Ser., 124, 61.
Bower G.A., Richstone D.O., Bothun G.D., and Heckman T. M.; 1993, Astrophys. J., 402, 76.
Cappellari M., et al. 2006, MNRAS, 366, 1126.
Davis, B. L., Berrier, J. C., Shields, D. W., Kennefick, J., Kennefick, D., Seigar, M. S., Lacy, C. H. S., & Puerari, I. 2012, ApJS, 199, 33,
Douglas 1995, ApJS, 100, 105, A,.
Elmegreen, B. G., Elmegreen, D. M., and Hirst, A. C.,2004., ApJ, 612, 191.
Ferrarese, L., and Merritt, D., 2000, ApJ 539, L9–L12.
Ferrarese, L., 2002., ApJ 578:90–97.
Gebhardt K. et al. 2000b, ApJ, 539, L13.
Gebhardt, K., Rich R. M. and Ho L. C., 2005, ApJ, 634, 1093.
Granato G. L., De Zotti G., Silva L., Bressan A. and Danese L.,. 2004, ApJ, 600, 580.
Greene J. E., Ho L. C., 2006, ApJ 641, L21.
Gültekin, K., et al. 2009, ApJ, 695, 1577.
Häring, N., and Rix, H.-W. 2004, ApJ, 604, L89.
Hooft, G. (2009). Introduction to the Theory of Black Holes. Institute for Theoretical Physics / Spinoza Institute.
Hu J., 2009, ArXiv:0908.2028;2009.
Hubble, E. P. 1926, ApJ, 64, 321.
Idiart, T. P., de Freitas Pacheco, J. A., Costa, R. D. D. 1996, AJ 112, 2541.
Jedrzejewski, R. I. 1987, MNRAS, 226, 747.
Kennicutt, R. C. 1981, AJ, 86, 1847.
Kormendy, J. and Richstone, D. O., 1995, ARA&A, 33, 581.
Kormendy, J., & Gebhardt, K. 2001, in AIP Conf. Proc. 586, 20th Texas.
Kormendy, J., & Kennicutt, R. C. 2004, ARA&A, 42, 603 (KK04).
Lake G., Dressler A.; 1986, Astrophys. J., 310,605.
Laurikainen, E., Salo, H., & Buta, R. , MNRAS, 362, 1319.
Lin, C. C., and Shu, F. H. .1964, ApJ, 140, 646.
Lucey J. R., Guzman R., Steel J., Carter D.; 1997, MNRAS, 287, 899.
Ma, J. 2001, Chin. J. Astron. Astrophys., 1, 395.
Magorrian J., Tremaine S., Richstone D. et al., 1998, AJ, 115, 2285.
Nelson C. H., Whittle M.; 1995, Astrophys. J., Suppl. Ser. 99, 67.
Oliva, E., Origlia, L., Kotilainen, J. K., Moorwood, A. F. M., 1995, A & A 301, 55.
Richstone, D., et al. 1998, Nature, 395, A14.
Sani E., Marconi A, Hunt L. K., Risaliti G., 2011, MNRAS. 2011;413:1479-94.
Schröder, M. F., Pastoriza, M. G., Kepler, S. O., & Puerari, I. 1994, A&AS, 108, 41.
Seigar, M. S., & James, P. A. 1998a, MNRAS, 299, 672.
Seigar, M. S., & James, P. A. 1998b, MNRAS, 299, 68532, 1391, 04.14.
Seigar, M. S., Bullock, J. S., Barth, A. J., & Ho, L. C. 2006a, ApJ, 645, 1012.
Seigar, M. S., Ho, L. C., & Barth, A. J. 2006b, Bulletin of the AAS, 38, 1190.
Seigar, M. S., Kennefick, D., Kennefick, J., & Lacy, C. H. S. 2008, ApJ, 678, L93.
Valeri. P. Frolov and Igor D. Novikov, 1998, Black Hole Physics: Basic Concepts and New Developments, Kluwer academic publishers.
Vallée, J. P. 2002, ApJ, 566:261-266.
Whitmore, B. C., McElroy, D. B., & Tonry, J. L., 1985, (ISSN 0067-0049), vol. 59, Sept. 1985, 1-21.